



**Politecnico
di Torino**

POLITECNICO DI TORINO

Master of Science in Civil Engineering
Structures specialisation

Master Thesis

**Hydrodynamic cavitation, nano-bubble implosion,
TeraHertz vibration, and correlated energy aspects**

Tutors:

Prof. Alberto Carpinteri

Dr. Francesco Montagnoli

Candidate:

Stefano Roggeri

Academic Year 2021/2022

Contents

Abstract.....	1
----------------------	----------

Chapter 1

Introduction to the physical phenomena.....	3
1.1 Piezonuclear reactions in solid media.....	3
1.2 Piezonuclear reactions in fluid media.....	9
1.3 Cavitation phenomenon and bubble behaviour.....	11

Chapter 2

Neutron emissions and early calorimetric experiments: Extrapolation method for COP assessment	20
2.1 Experimental set-up.....	20
2.2 Energy balance assessment.....	25
2.3 Neutron emissions from the non-insulated plant with plastic cavitators	31
2.4 Calorimetric experiments on the plant with plastic cavitators.....	38
2.5 Calorimetric experiments on the plant with brass cavitators (extrapolation method).....	48
2.6 Calorimetric experiments on the plant with second-generation brass cavitators (extrapolation method).....	69

Chapter 3

Optical experiments to determine the bubble dimension distribution and the energy emitted from the nano-bubble implosion.....	95
3.1 Phase Doppler Anemometry technique.....	95
3.2 Optical experiment for the three best brass cavitators.....	97

3.3	Evaluation of the energy emitted per nano-bubble imploded.....	111
------------	---	------------

Chapter 4

Calorimetric experiments: Direct method for COP evaluation.....	115
--	------------

4.1	Overcoming of the extrapolation method and the direct evaluation of COP for cavitators NB and NM.....	115
------------	--	------------

4.2	Application of the direct method to evaluate COP for cavitators M5, M2 and M4.....	143
------------	---	------------

Conclusions.....	157
-------------------------	------------

Acknowledgements.....	159
------------------------------	------------

References.....	160
------------------------	------------

Abstract

In the last two decades, a large amount of evidence has been collected by the research group at the Politecnico di Torino about compositional changes and neutron emissions in solid bodies subjected to fracture. The reasons of the compositional variations in medium-weight elements of the analysed specimens and of the revealed anomalous neutron radiations, which clearly indicated the nuclear nature of the phenomenon, were found in the effect of nano-scale mechanical instabilities in condensed matter. The development of the nano-scale instabilities produces TeraHertz pressure waves (phonons), that expand throughout the specimen crystal lattice and establish resonance with the lattice, consequently producing Low Energy Nuclear Reactions (LENR). The discovery of the piezonuclear reactions led to a wide field of possible practical applications, including the earthquake precursors, as well as the study of the Earth's crust, atmosphere and ocean compositional evolution in time.

As micro-cracking in rocks, so implosion of micro- and nano-bubbles produced by cavitation in a water solution enriched by iron salts has been supposed to be the cause of the compositional changes and of the anomalous neutron emissions revealed simultaneously to the cavitation tests.

The aim of the present thesis is to deepen the comprehension of the cavitation as regards the effects on a water solution, focusing in particular on the study of the extra-heat generation. In order to obtain a reliable parameter to evaluate the thermal efficiency of the cavitation process, two different assessment methods for the Coefficient Of Performance in the steady-state condition were developed and applied, passing from a first extrapolation procedure to a final direct estimate. The two methods considered three terms of thermal and mechanical output energies produced by the cavitation and one term of input energy (the electrical supplies to the three-phase pump of the cavitation plant) for the evaluation of the ratio between the output and input energy contributions. In particular, the thermal energy stored by the entire mass of water in a full cycle, the thermal dispersions in the environment by conduction, convection, and irradiation, as well as the mechanical energy dissipated by the solution in the passage through the cavitator section were considered as output energy terms. Although some differences between the results of the extrapolation and the direct methods were revealed, both of them allow to quantify a significant excess of the output thermal and mechanical energies with respect to the input electrical supply. The energy excess was ascribed to the effect of LENR in the iron salts dispersed in the water solution (fission reactions).

As a consequence of the considerable number of tests performed, the calorimetric monitoring of different geometries of cavitation nozzles led to the definition of some improvement factors to be

considered as possible future implementations of cavitation reactors for industrial applications, especially in terms of pump turning velocities, working pressures, and internal geometrical profiles of the cavitators.

In addition to the results of the calorimetric tests, a series of optical measurements of the dimensions of the bubbles produced by cavitation confirm the importance of nano-scale instabilities and TeraHertz-frequency phonons for the promotion of LENR, encouraging to further studies on the subject.

Chapter 1

Introduction of the physical phenomena

1.1 Piezonuclear reactions in the condensed matter

Since 2008, a series of experimental studies were conducted by the research group led by Prof. Alberto Carpinteri, at Politecnico di Torino, in order to examine the different forms of energy emissions which occur from solid-state fracture. Starting from tests on specimens made of rock, they found some unexpected neutron emissions and compositional changes in the investigated materials, which are strictly linked to the Low Energy Nuclear Reaction (LENR) research topic [7][20].

In particular, the first experimental evidence were obtained from compression fracture tests under monotonic displacement control on Luserna Green Granite and Carrara Marble specimens, containing respectively percentages of iron oxides equal to the 3% and the 0.07% of the total weight [10] [12]. As regards the Luserna Green Granite specimens, the neutron emission monitoring allowed to register relevant neutron radiation peaks simultaneously to the brittle failure [9][12]. The subsequent chemical analysis of the fracture surfaces by means of the Energy-dispersive X-ray spectroscopy (EDS) revealed significant depletions of the iron contents which were perfectly balanced in mass by aluminium and by magnesium and silicon increases, respectively as a consequence of symmetrical and asymmetrical fission reactions [18] [11]. The Carrara Marble samples, instead, were characterised by the absence of relevant neutron emissions corresponding to the brittle failure, but anomalous alpha particle emissions were noticed, reaching values of also ten times higher than the natural background. Simultaneously, compositional changes on the fracture surfaces were produced, with a decrease of about the 13% in the oxygen, calcium and magnesium content and an almost equal increase in the carbon amount [20][14]. The causes of the different types of LENR observed for the two different materials were identified in the chemical composition of the specimens, especially as regards the starting iron content, and in the brittleness number of the materials themselves, which was greatly major for granite than for marble, reflecting a more catastrophic failure [10]. Neutron emissions, followed by electro-magnetic and acoustic ones, were also revealed during compression tests performed on iron-rich basalt and magnetite specimens [16].

In order to explain the relevance of the results got, it was firstly mandatory to highlight that the mechanical instabilities in the condensed matter, as well as fractures or buckling in solid bodies or turbulence and cavitation in liquid media, produce pressure waves that cause contractions and expansions in the longitudinal direction and shear distortions in the transverse direction. These pressure waves, currently defined as “phonons”, have a wavelength which has been found to be always of the same order of magnitude of the cause of the original mechanical perturbation and, as a consequence, it can not exceed the maximum dimension of the body in which the instability takes place [31].

According to the two empirical scaling criteria previously found and considering that the range of the size of continuous bodies that can be interested by different kinds of mechanical instabilities is extremely wide, it can be immediately understood that also the wavelength of the generated phonons may change in a very significant way, by varying from the kilometre scale, in the case of cracks developed in active faults movements, to the nanometre one, due to the movements of vacancies and defects in crystal lattices or the formation or coalescence of nano-cracks in solid media [31].

Analogously, the frequency of the phonons varies also proportionally to the dimension of the original cause of the perturbation, according to the following elementary relation:

$$f = \frac{v}{\lambda} \quad (1.1)$$

where f is the frequency of the phonon, v is the wave velocity and λ is the wavelength.

Since the value of the wave velocity in both solids and fluids oscillates often around $10^3 \frac{m}{s}$, it is lawful to assume this value as a constant, so that it is possible to relate the frequency of the perturbation wave as a function of the dimension of the wavelength. On the other hand, according to the observation that the wavelength has the same order of magnitude of the source of the original mechanical cause, it follows that the frequency of the perturbation wave can be also related to the dimension of the instability source [31]. In addition, it should be pointed out that the wavelength, λ , can never exceed the size of the body interested. Based on these observations and assumptions, the graph in Fig. 1.1 has been developed [20].

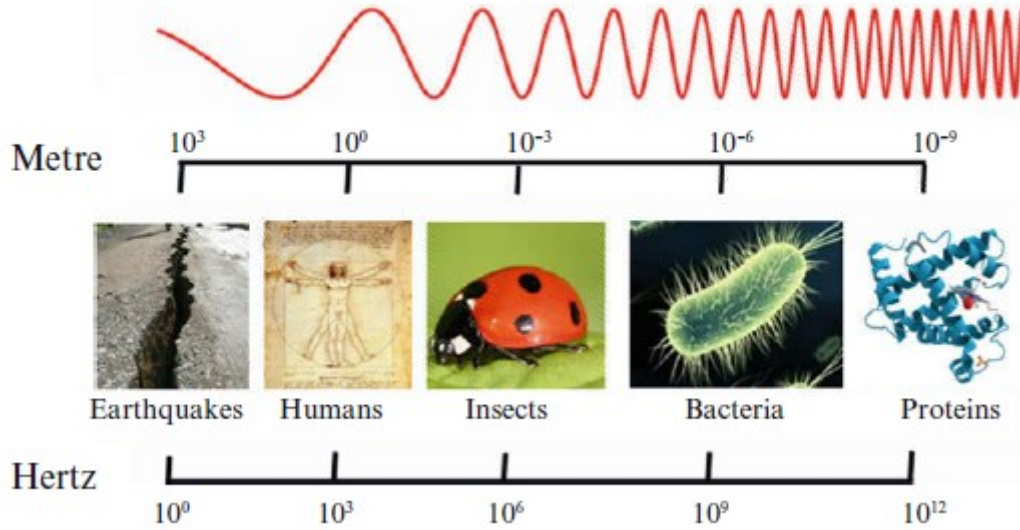


Fig. 1.1 Correlation between wavelength and frequency of phonons for a constant wave velocity in the medium.

Focusing the attention on nanoscale perturbation in solid bodies, according to Eq. (1.1) it is possible to find that the frequency of the related pressure waves falls into the Terahertz field:

$$f = \frac{v}{\lambda} \cong \frac{10^3 \frac{\text{m}}{\text{s}}}{10^{-9} \text{m}} \cong 10^{12} \text{Hz} = 1 \text{ THz} \quad (1.2)$$

Therefore, the previous relationship provides the evidence that these high-frequency phonons can induce mechanical resonance of the crystal lattice of the material crossed, which can lead to fission reactions in the chemical elements involved [20] [31]. These phenomena are commonly called “piezonuclear reactions” or LENR in the literature. The reactions are often accompanied by apparently anomalous neutron emissions that can reach also peaks several times higher than the base neutron radiation and that are clear indicators of the nuclear nature of the phenomenon [3] [5]. Another important evidence of the nuclear nature of the observed reactions was given by the compositional analyses of the fracture surfaces of the broken specimens [11]. In particular, it was found a clear decrement in the chemical concentration of some heavy elements and, conversely, a substantial increase in the chemical concentration of lighter elements, which were found with very low concentrations before to perform the experimental tests [10]. On the other hand, in all of cases a perfect mass balance was found between the uncracked and the cracked specimen concentrations, considering also the contribution of the emitted neutrons [10] [20].

A possible cause of the piezonuclear reactions in solid bodies has been found in the resonance phenomenon in the TeraHertz range that involves the crystal lattice subjected to phonons. In fact,

since the distances between the atoms of the crystal lattice have dimensions of the order of the nanometre, the corresponding Debye frequency of the crystal lattices themselves will fall in the TeraHertz range [31]. Thus, since the fundamental frequency of free vibrations of the crystal lattice is almost close to the phonon frequency, it follows that these high-frequency pressure waves can be at the origin of the resonance phenomenon that involves the solid media [20] [31].

In addition, a further confirm of the capacity of high frequency pressure waves to promote nuclear reactions (in the case of interest low energy ones), can be given by considering the thermal neutrons that cause the fission of uranium atoms [31]: the thermal neutrons, in fact, have an energy range around about 0.025 eV in environmental temperature conditions, which corresponds to almost 4.0×10^{-21} J; considering the Planck Law

$$E = h \times f \quad (1.3)$$

with Planck constant $h = 6.62607015 \times 10^{-34}$ J \times s and the previous energy of the thermal neutron $E = 4.0 \times 10^{-21}$ J, it is possible to evaluate the frequency of the thermal neutron as $f = 6.04 \times 10^{12}$ Hz = 6.04 THz, close to the uranium lattice resonance frequency of 6.24 THz [31]. As well as for thermal neutrons for uranium, the phonons at TeraHertz frequencies produced in the condensed matter by nanoscale mechanical instabilities could be able to activate fission reactions in the crossed materials, the piezonuclear reactions. This could take place because of the frequencies of these phonons are close to the natural resonant frequencies of a lot of medium-weight elements (for iron, for example, $f_{Fe} = 7.77$ THz) [31].

As well as for the phonons, recent studies have also suggested that the plasmons, oscillations of the electronic density in solid lattices, could be a further possible cause of the promotion of piezonuclear reactions in medium-weight elements as iron, by means of the plasmon-lattice interactions caused by nano-scale fractures [35].

After having briefly recalled the main characteristics of the physical phenomenon which is at the base of all the studies reported in the following of the treatise, it is necessary to point out the fact that the study for deep comprehension of the processes leading to the piezonuclear reactions is still in a starting phase. It is also important to underline that, departing from the field of the solid mechanics, a lot of great-potential applications of the detection of LENR could be done in the future, as stated from the studies did at Politecnico di Torino in the last years and now under development [20] [31]: in the seismic field neutronic emissions from nanocracks, as well as electromagnetic and acoustic emissions for cracks of increasing length (altogether called “Fracto-emissions”) could be used for the prevision of earthquakes in specific areas; in the structural engineering field the detection of fracto-emissions could be used for the fatigue and failure

monitoring of steel elements and for fracture precursors in both concrete elements and rock structures or formations; in the biological and chemical field these reactions can be analysed for a better comprehension of mechanical behaviour of complex molecules; in the geologic field the study of piezonuclear reactions can help the understanding of natural formations and evolution mechanisms of the Earth crust; other possible applications may be developed in the future.

As regards the seismic precursors, the first observations of anomalous neutron radiation peaks preceding of about 7-8 days seismic events were collected in July-August 2008 at the “Testa Grigia” laboratory of Plateau Rosa, Cervinia (Italy), for an earthquake of the third degree of the Richter scale, in April 2009 for the earthquake of L’Aquila of the sixth degree of the Richter scale and in January 2013 in the experimental campaign of Bettola, Piacenza (Italy), for an earthquake of magnitude five that was then registered in Garfagnana [2] [25]. In a second phase, a complete survey and analysis of low-magnitude earthquakes between 2013 and 2015, and especially between January 2016 and the end of June 2017, accomplished by means of the monitoring station installed 100 m under the ground level in the San Pietro Prato Nuovo gypsum mine, Piedmont (Italy), allowed to confirm that relevant neutron emissions above the natural background precede seismic events of about 7-8 days, electro-magnetic emissions forerun the events of about 3-4 days and acoustic emissions of about 1-2 days [26] [29]. Referring then to the concept of the “earthquake preparation zone”, whose radius progressively reduces in time around the epicentre [26] [29], in the near future some alerting systems would be developed in order to reduce the casualty rates of high-magnitude earthquakes, based on territorial databases [21]. As a further note, the neutron emissions produced by a high-magnitude seismic event (Old Jerusalem Historical Earthquake) have been also proposed as the cause of the Turin Holy Shroud image formation and of the unreliable results of the radiocarbon analyses [15]. The different kinds of the revealed fracto-emissions are the consequence of the increasing dimensions of the Earth’s crust fractures which precede the final seismic crack and movement, and they constitute a confirm of paramount importance of the scaling law and of the deep correlation between the dimensions of the mechanical instability and the wavelengths of the produced phonons [20] [29].

As regards the failure and fatigue monitoring, the neutron emission survey on medium-dimension prismatic specimens made by mortar enriched by iron salts revealed neutron peaks corresponding to the compressive failure which was about three times the natural background, and also compositional changes on the fracture surfaces were noticed [6] [8]. Tensile and compressive tests in both static and cyclic conditions were carried out on steel samples and they allowed to measure anomalous neutron emissions, despite with lower absolute deviations from the background [4] [20] [33]. The reason of the reduced emissions was identified in the ductility of the collapse

mechanism for the steel rebars [4][33], which prevented the formation of diffused cracks and then the most common mechanical instabilities promoting LENR. Nevertheless, the neutron emission monitoring for steel fatigue monitoring and for concrete damage estimate is still under development [33]. On the other hand, focusing on another kind of fracto-emission, the acoustic monitoring and resonant frequency analysis for concrete members have been proposed as an alternative method for assessment of the present damage, cracking development and remaining lifetimes of concrete structures [8][34].

Moreover, the reference to the piezonuclear reactions was proposed to answer to relevant still unresolved problems about the Earth's crust, ocean and atmospheric evolutions in time [20][28]. In particular, the documented decrease of some heavier elements as iron and nickel, which passed from concentrations respectively of about the 15% and 1% in the original crust to the actual 4% and 0.01%, according to the proposed theory was balanced by the simultaneous relevant increase of lighter elements such as silicon, that passed from the 24% to the actual 28.8%, aluminium, that increased from the original concentration of the 4% to the 8%, and other elements like carbon, nitrogen and oxygen [28] [30]. The LENR promoted by the heavy seismic activity in the geological ages have been proposed as the cause of the previous compositional variations, which were found to coincide with the compositional changes observed in the laboratory fracture tests, and they could be the cause of the so called "Great Iron Depletion" [20] [28]. The predicted nuclear reactions were indicated also as the causes of the compositional changes documented in the Earth's atmosphere by means the analysis of ice carrots: the carbon pollution of the Archean era (3.8-2.5 billions of years ago) is believed to have been caused by the contemporary formation of the tectonic activity and the subsequent seismic period, which altered the composition of the crust causing the decrease of Fe and Ni [26] [28] [30]; the following increase in the nitrogen and oxygen concentrations, defined as "Great Oxidation Event" is supposed to have been produced then by the further fission of a part of the magnesium, silicon and aluminium, which was caused by a new phase of intense seismic activity [13] [20] [30]. Even the actual growth of the CO₂ dispersed in the atmosphere might be partially influenced by natural amounts released from tectonic fractures [13] [28] [30]. Furthermore, the oceanic composition in terms of salt contents seem to be deeply influenced by LENR produced by fractures in the oceanic crust and in the subduction zones [13]: the progressive decrease of iron, nickel, calcium and magnesium contents was found to be contemporary to the progressive increase in sodium, potassium and oxygen (the last one released then in atmosphere) [18] [20]. In particular, the compositional changes due to the effect of piezonuclear reactions promoted by the seismic activity have been proposed as a cause of the high salinity levels of the eastern Mediterranean Sea [13] [24]. The calcium and magnesium depletion has been also proposed as a possible additional

cause to the ocean formation itself, since the fission of these two elements is believed to have been able to produce oxygen and hydrogen, which then could have reacted to form water [20] [24] [28].

A relevant confirmation of the previous LENR was finally obtained by means of the Nuclear Visualization Software (NVS) analyses performed on the lattice model of Cook and Dallacasa, that allowed to reproduce the fission reactions and mass balances which had been previously theoretically proposed [23].

1.2 Piezonuclear reactions in fluid media

The piezonuclear reactions can interest not only the solid matter due to cracks, movements or propagation of defects or local instability in material lattices, but they were detected also in liquid media and solutions. The most relevant evidence of piezonuclear reactions in fluid media were found in the cases of electrolysis and hydrodynamic cavitation, the main subject of the present paper, in both cases with anomalous extra-heat generations and neutron emissions [27] [36].

As regards electrolysis, microcracking of the metal electrodes was observed, as well as anomalous temperature increases, and it was ascribed to the embrittlement caused by the hydrogen atoms produced by electrolysis itself [27]. In particular, the free hydrogen atoms released in the solution enriched by potassium carbonate K_2CO_3 by effect of the electrolysis of water caused the embrittlement of the Ni-Fe and the Co-Cr electrodes, which were subjected to extensive surface microcracks during the electrical activity of the cell [17] [22]. The cracking of the surfaces of the electrodes was recognised to be the cause of piezonuclear reactions that were firstly revealed in terms of significant neutron and alpha particle emissions, several times higher than the respective background levels [22]. Therefore, the analysis of the compositional changes on the fracture surfaces of the first electrode allowed to observe almost perfect balances in mass between the decrease of the nickel and iron contents and the increase of silicon, magnesium and chromium for the Ni-Fe electrode (the fission of iron produced chromium and alpha particles, two different fissions of nickel produced the first silicon and neutrons and the second magnesium and alpha particles); on the Co-Cr electrode, the fission of cobalt produced iron, alpha particles and neutrons while the fission of chromium produced potassium, alpha particles and neutrons, always fulfilling the balance of masses [17] [22]. Similar effects in terms of neutron emissions and compositional changes as a consequence of hydrogen embrittlement were also noticed for electrolysis experimental tests on palladium and iron electrodes [19]. Despite the interesting results obtained as regard the LENR by the hydrolysis tests, also in terms of thermal energy released, it is worth noting

that the piezonuclear reactions took place mainly still as a consequence of fractures in solid media rather than in the aqueous solution, distinguishing for this aspect from the case of hydrodynamic cavitation described in the following.

Hydrodynamic cavitation is a physical phenomenon which can be defined at first as the production of gas or, better, vapour bubbles in a liquid medium as a consequence of large pressure variations induced by dynamic causes [27]. The variations in pressure leading to the development of cavitation can be produced by different working layouts and devices. A first example of these can be found in the propellers of nautical engines, for which cavitation is the source of several degradation and durability problems of metal components, subject matter of research of mechanical engineers. A second example can be given by converging-diverging nozzles of small internal diameters constraining the flux of liquids in pressure.

Deepening the second case, in particular (but it is possible to consider that the induced cavitation phenomenon is almost the same also for the effect of the propeller action) the small diameter nozzle constitutes an obstacle for the flux of liquid in a duct of higher section. This obstacle produces a great increase of pressure before the nozzle and then a noticeable increase of the velocity due to the narrowing of the duct section itself. This increment of velocity causes a drop of the fluid pressure after the nozzle that can decrease below the lower limit of the vapour pressure, causing partial vaporisation of the liquid means and the formation of bubbles. When the fluid distances from the nozzle, the pressure starts to increase again, and in very short time the formed bubbles are subjected to great compression stresses [36]. These stresses are able to promote the condensation of the vapour in the regions of the bubble nearer to the gas-liquid interface. The contraction of the bubbles in this phase could be so fast that the bubble wall velocity can also exceed the velocity of sound in the fluid and then the vapour in the central part of the spherical volume becomes subjected to extreme pressure and temperature conditions. The extreme conditions of this vapour, which is far from the reducing gas-liquid interface and because of this is defined as “trapped vapour”, are able to cause chemical reactions in the vapour molecules, leading to the production of mainly OH radicals but also atomic O and H_2O_2 , oxidants [39]. The violent implosions of the bubbles in the compression phase can be considered as adiabatic collapses [27]. The most relevant aspect to be underlined for the aims of the present treatise is that these collapses produce pressure waves in the liquid medium, so phonons, that have been found to be able to elicit piezonuclear reactions inside the ions of the metallic salts dissolved in the fluid [36].

On the bases of what previously said, it seems to be relevant for promoting these reactions in particular the effect of nano-bubbles collapses, in order to obtain phonons at the Terahertz frequencies (Eq. 1.2). In this case, indeed, the mechanical perturbation cause, which is the collapse

of the nano-bubble itself, has a sufficiently low characteristic dimension to induce resonance between the emitted phonons and the natural frequencies of the metal elements in solution. A noticeable amount of proofs about piezonuclear reactions produced by hydrodynamic cavitation have been detected at Politecnico di Torino by the research group of Prof. Carpinteri in the last ten years. These proofs were given by the significant extra-heat generations between the fluid before and after the nozzles, by the relevant changes in the concentrations of metal ions in the solutions before and after cavitation (with depletions of heavier elements and increases of lighter ones) and finally by remarkable neutron and even alpha particle emissions [20]. Some of the most relevant results are going to be explained in the following chapters.

1.3 Cavitation phenomenon and bubble dynamics

In order to analyse the effect of hydrodynamic cavitation on water solutions, it is mandatory to give more details about the physical phenomenon of cavitation itself and the behaviour of the bubbles produced. In doing that, the concepts reported in the book “Cavitation and bubble dynamics” of C.E. Brennen (Oxford University Press, 1994) [1] are going to be followed.

Cavitation can be defined in more refined way as “the process of nucleation in a liquid when the pressure falls below the vapour pressure” or also as “the process of rupturing of a liquid by decrease in pressure at a roughly constant liquid temperature”. It is worth considering that the constant liquid temperature condition can be considered valid for the case of study since the heat generation from LENR is consequent to cavitation, and do not influence the previous bubble formation. As suggested by the first definition, the production of bubbles during cavitation starts from “nucleation sites”. The nucleation sites can have different nature, as well as temporary small-dimension voids in the fluid (for the “homogeneous nucleation”) or the liquid-solid interfaces with suspended solid particles and container surfaces (for “heterogeneous nucleation”). In the first case the voids can be intended as very small-dimension bubbles in the fluid due to gaseous inclusions.

According to the homogeneous nucleation theory, the growth of the voids, and thus the development of bubbles, will happen at a difference of pressure, Δp_C , between the interior part of the void and the fluid pressure, defined as the tensile strength of the liquid as follows:

$$\Delta p_C = p_B - p = \frac{2 S}{R_C} \quad (1.4)$$

where p_B is the pressure inside the original nucleation bubble, p the pressure of the fluid, S the surface energy (also called “surface tension”) and R_C the critical radius, maximum size of the voids

[1]. It is relevant to note that the reduction of the liquid pressure p produces an increase in the value of Δp_c that moves closer to the cavitation condition, as it happens after a nozzle. The corresponding critical energy [38] for the beginning of cavitation is then:

$$W_{CR} = \frac{16 \pi S^3}{3 \Delta p_c^2} \quad (1.5)$$

Referring to a single-phase, inviscid and frictionless Newtonian fluid with pressure $p(x_i)$ in the generic position x_i , reference pressure of the uniform upstream flow p_∞ , density ρ and velocity U_∞ , the following pressure coefficient can be defined:

$$C_p(x_i) = \frac{p(x_i) - p_\infty}{\frac{1}{2} \rho U_\infty^2} \quad (1.6)$$

Considering the previous hypothesis, the minimum value of the pressure coefficient, C_{pmin} , depends only on the geometrical boundary conditions of the flow and then it can be considered as known (for a viscous fluid a dependence of the Reynolds number has also to be taken into account).

In order to define the conditions of starting cavitation, another important coefficient is then introduced, the “cavitation number”, σ , being $p_v(T_\infty)$ the vapour pressure of the fluid at the temperature of the fluid itself, T_∞ :

$$\sigma = \frac{p_\infty - p_v(T_\infty)}{\frac{1}{2} \rho U_\infty^2} \quad (1.7)$$

In the theoretical case of a liquid without any tensile strength, if the value of the cavitation number decreases below the limit value of the incipient cavitation number, σ_i , vapour bubbles will start immediately to increase their amount and dimensions, having in this way cavitation. In this condition σ_i assumes the following value:

$$\sigma_i = -C_{pmin} \quad (1.8)$$

Despite under the simplified and theoretical hypotheses previously established the condition of beginning of the cavitation process can be considered $\sigma \leq \sigma_i = -C_{pmin}$, in real cases the true values of the incipient cavitation coefficient are significantly different from the minimum pressure coefficient. These differences are due to many possible causes influencing the behaviour of the liquid flow, such as the tensile strength of the fluid (which reduces σ_i), the residence time effect (reducing σ_i), the presence of contaminant gas in solution (increasing σ_i), turbulence in the fluid

(increasing σ_i) and the viscosity effects. The effect of turbulence causes an increase of the incipient cavitation number because in the central part of the vortex a lower pressure than the average one in the fluid can be produced, with possible local cavitation before the expected limit. The viscosity of the fluid is considered, as said, by the Reynolds number (where μ is the dynamic viscosity and l is the characterized length scale):

$$R_e = \frac{\rho U_\infty l}{\mu} \quad (1.9)$$

Viscosity has a complex effect on cavitation index since it influences both directly σ_i and indirectly C_{pmin} , with two different dependencies on the Reynolds number to be combined. Apart from the previous ones, also other effects may influence the cavitation inception, such as the quality of the fluid and of the dispersed particles and the roughness of the surfaces in contact. Because of all these effects, the evaluation the cavitation inception coefficient is a very complex task, and it shows a great variability from different conditions and sites. The effects of just the Reynolds number and inclusions in water solutions are reported in Fig. 1.2.

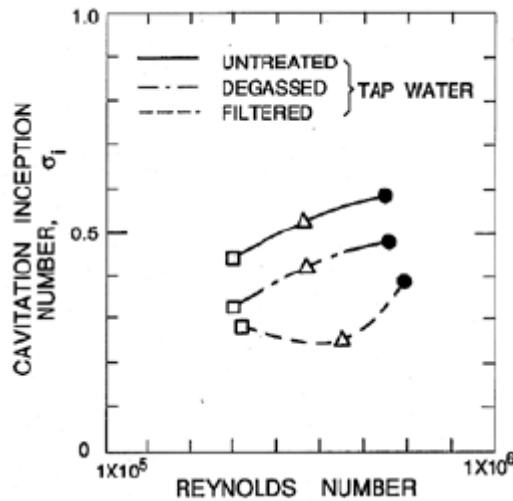


Fig.1.2 Cavitation inception number as a function of Reynolds number and water solution condition (Keller 1974), taken from “Cavitation and bubble dynamics” of C.E. Brennen (Oxford University Press, 1994).

Once cavitation has started and bubbles have formed, it is necessary to discern between the cases of stability or instability, and thus fragmentation and collapse, of the bubbles produced. Although some critics have been moved in the last years to the real representativeness of the method, especially for small diameter bubbles, the traditional Blake approach (1949) is going to be rapidly treated about this problem [37]. According to this approach, a bubble in a fluid is unstable if its radius exceeds the Blake critical radius, R_C , function of the mass of the gas included, m_G , and its

temperature, T_B , of the gas constant, K_G , and the surface energy, S ($k=1$ for constant temperature conditions):

$$R_c = \left[\frac{9km_g T_B K_G}{8\pi S} \right]^{1/2} \quad (1.10)$$

The same critical condition can be seen in terms of pressures by the following lower limit pressure value:

$$p_{\infty c} = p_v - \frac{4S}{3} \left[\frac{8\pi S}{9km_g T_B K_G} \right]^{1/2} \quad (1.11)$$

If the pressure in the liquid is lower than the critical pressure above, bubbles will form in the fluid having radii greater than the critical one. Therefore, they will violently collapse in the successive compression phase, being then in a condition of unstable equilibrium.

Just to give an order of magnitude of theoretical values obtained in case of incompressible fluids, if a common maximum radius at the verge of collapse almost 10^2 times the size of nucleation sites is considered, in the compression phase immediately before the bubble implosion pressures of also 10^{10} bar and temperatures reaching $4 \cdot 10^4$ times the environmental one are obtained in the core of the bubbles, even if just for fractions of microsecond and in an extremely reduced space. In real cases some mitigating effects as gas diffusion and liquid compressibility can reduce these values up to estimated lower bounds of about 6700 K and 848 bar respectively for temperatures and pressures [1].

The pressures of the waves produced by the bubble collapse and their propagation in the fluid medium were firstly numerically studied by Hickling and Plesset in 1964, considering the so called “rebound” of the bubble [32]: after having reached the maximum acceptable diameter of the bubble, called R_o by Hickling and Plesset or R_M by Brennen, the bubble starts to be subjected to compressive stresses; these stresses reduce its diameter and cause thus a contraction of the bubble itself; the contraction progressively leads to extreme temperature and pressure conditions in the bubble core; once the collapse condition is reached, the bubble implodes causing a new expanding pressure wave that propagates [1] [32]. This last expanding pressure wave is the phonon, the possible cause of piezonuclear reactions.

In the contraction phase preceding the collapse, the pressure profiles depicted in Fig 1.3 were obtained [32], plotted as a function of the distance from the centre of collapse, r , both in non-dimensional form, and of the time indices $[-16; -0.1]$. The time indices are negative since time zero was established at the instant of collapse.

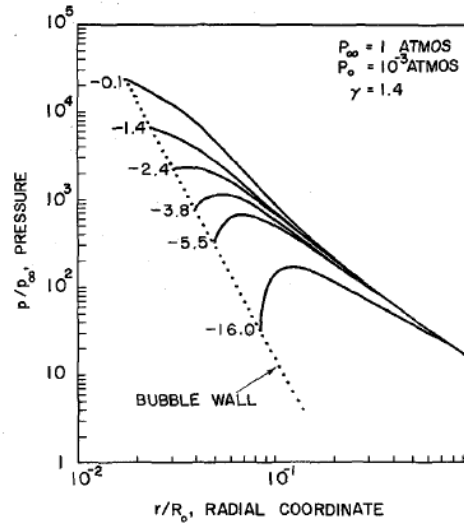


Fig. 1.3 Pressure profiles at different times around the bubble surface before collapse (Hickling & Plesset, 1964).

After the bubble collapse, the pressure profiles numerically evaluated have been reported with the shapes shown in Fig.1.4, that highlights a damping by increasing the distance between the origin of the implosion site proportional to r^{-1} (as before [0.1;16] are time indices, now positive) [32].

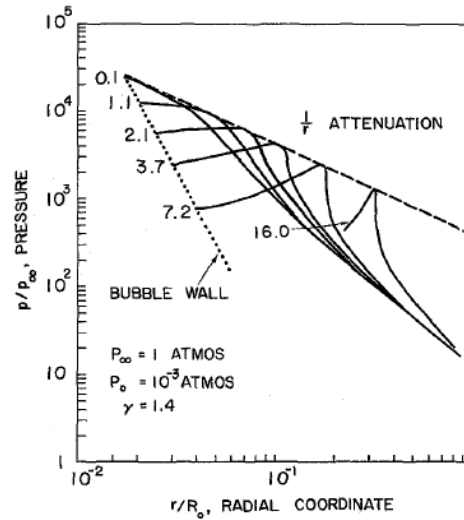


Fig. 1.4 Pressure profiles at different times around the bubble surface after collapse (Hickling & Plesset, 1964)

An approximated expression for the peak pressure of the generated wave can be obtained as follows:

$$p_p \approx \frac{100R_M p_\infty}{r} \quad (1.12)$$

By simply evaluating the peak pressure of the phonon at distance $r = R_M$ and for the reference pressure of the liquid in rest $p_\infty = 1$ bar, a value of $p_p = 100$ bar can be obtained, result confirmed by empirical tests.

All the concepts about bubble dynamics introduced until now have been referred to the starting simplifying hypothesis of a single-phase fluid. In real cases, for the orders of magnitude of the bubble concentrations of cavitation tests, the validity of this hypothesis is jeopardised and it is needed to refer to multiphase fluids (two-phase ones, actually). In the following, a brief explanation of some of the main characteristics of the multiphase flow are going to be analysed, in order to better describe the effect of the nozzles on the flow itself.

The multiphase behaviour of a mixture can be classified as “separated”, for phases with different velocities and then relative motions between them, or as “homogeneous”, in case of negligible differences in the velocities and relative movements. The last one is the most common case for bubbly flows.

Multiphase flows are defined (as the single-phase ones) by a continuity, a momentum and a barotropic equation. The barotropic equation, linking pressure and density of the fluid, can be written by isolating the term c , the sonic speed in the medium, according to the general expression of Eq. (1.13). The density of a multiphase flow, ρ , can be evaluated as the sum of the products of the volume fractions of each of the N phases, α_N , by the density of the phase itself, ρ_N .

$$c = \left(\frac{dp}{d\rho} \right)^{1/2} \quad (1.13)$$

In the case of polytropic gas behaviour and under the assumption of null surface tension of the fluid (then equality of the gaseous and liquid phases pressures), the equation of the sonic speed in a two-component flow can be written in a simplified form as follows:

$$\frac{1}{c^2} = [\rho_L(1 - \alpha) + \rho_G\alpha] \left[\frac{\alpha}{kp} + \frac{(1 - \alpha)}{\rho_L c_L^2} \right] \cong \frac{\alpha}{kp} [\rho_L(1 - \alpha) + \rho_G\alpha] \quad (1.14)$$

In the previous equation α is the volume fraction of the gaseous phase, c_L is the sonic speed in the liquid phase alone and k is the polytropic index, which is equal to 1 for isothermal and 1.4 for adiabatic bubble behaviour. The second equivalence in Eq. (1.14) is valid only for quite relevant concentrations of gas in the mixture, since for very low ones the liquid compressibility term $\frac{(1-\alpha)}{\rho_L c_L^2}$ is not negligible (it is negligible just for $\alpha_o \gg \frac{p_o}{\rho_L c_L^2}$, with the subscript “o” indicating the fluid in reservoir condition). As established by the studies of Karplus (1958) and Gouse and Brown (1964),

the sonic speed can decrease very significantly for high gas concentrations in the two-phase solution, reaching also values of about $20 \frac{\text{m}}{\text{s}}$ for α between 0.4 and 0.6 [1].

By considering the compressibility effect of the multiphase fluid (more general case), the sonic speed can be also rewritten as a function of the pressure in the fluid itself, as reported:

$$c^2 = \frac{p}{\rho_L} \frac{\left[1 + \frac{\alpha}{1-\alpha}\right]^2}{\left[\frac{1}{k} \frac{\alpha}{1-\alpha} + \frac{p}{\rho_L c_L^2}\right]} \quad (1.15)$$

As a function, instead, of the original reservoir pressure conditions, it can be expressed as follows:

$$c^2 = \frac{kp_o}{\rho_o} \frac{(1-\alpha)^{k-1}}{\alpha^{k+1}} \frac{\alpha_o^k}{(1-\alpha_o)^{k-1}} \quad (1.16)$$

Through the application of the continuity and momentum equations for the flux, assumed as unidirectional and frictionless, a similar equation for the two-phase fluid velocity at every different point of the duct has been obtained. The spatial variability is implicitly considered within the gas volume fraction α :

$$u^2 = \frac{2kp_o}{\rho_o} \frac{\alpha_o^k}{(1-\alpha_o)^{k-1}} \left[\frac{1}{k} \left\{ \left(\frac{1-\alpha_o}{\alpha_o} \right)^k - \left(\frac{1-\alpha}{\alpha} \right)^k \right\} + \{ \text{either } f_{k=1}(\alpha) \text{ or } f_{k \neq 1}(\alpha) \} \right] \quad (1.17)$$

Knowing then the continuity equation:

$$\frac{d}{ds}(\rho u A) = 0 \Rightarrow A = \frac{\text{constant}}{\rho u} = \frac{\text{constant}}{\rho(1-\alpha)} \quad (1.18)$$

and the variation of the gas volume fraction as a function of the pressure, the following relevant relation was found:

$$\frac{1}{A} \frac{dA}{ds} = \frac{1}{\rho} \frac{dp}{ds} \left(\frac{1}{u^2} - \frac{1}{c^2} \right) \quad (1.19)$$

From the equation (1.19) it can be noticed that at the throat of the duct (but actually also in the other portions with constant section on the infinitesimal length ds) $\frac{dA}{ds} = 0$. To fulfil the equation, it is needed, thus, that one of the following two conditions is verified, $\frac{dp}{ds} = 0$, which is true in

unchoked conditions that are also subsonic ones, since in this case u is generally lower than c , or $\frac{1}{u^2} - \frac{1}{c^2} = 0$ and then $u = c$, for choked and supersonic conditions [1].

The relations between the physical quantities previously defined (pressure, fluid velocity and void or gaseous phase ratio) were expressed by Brennen as a function of the area, A , of the duct equipped by the nozzle and of the corresponding properties of the throat section (being the nozzle itself) identified by $*$ [1]. They were used to obtain the graphs in Fig. 1.5, which represent the effect of the reduction of section for a choked flow:

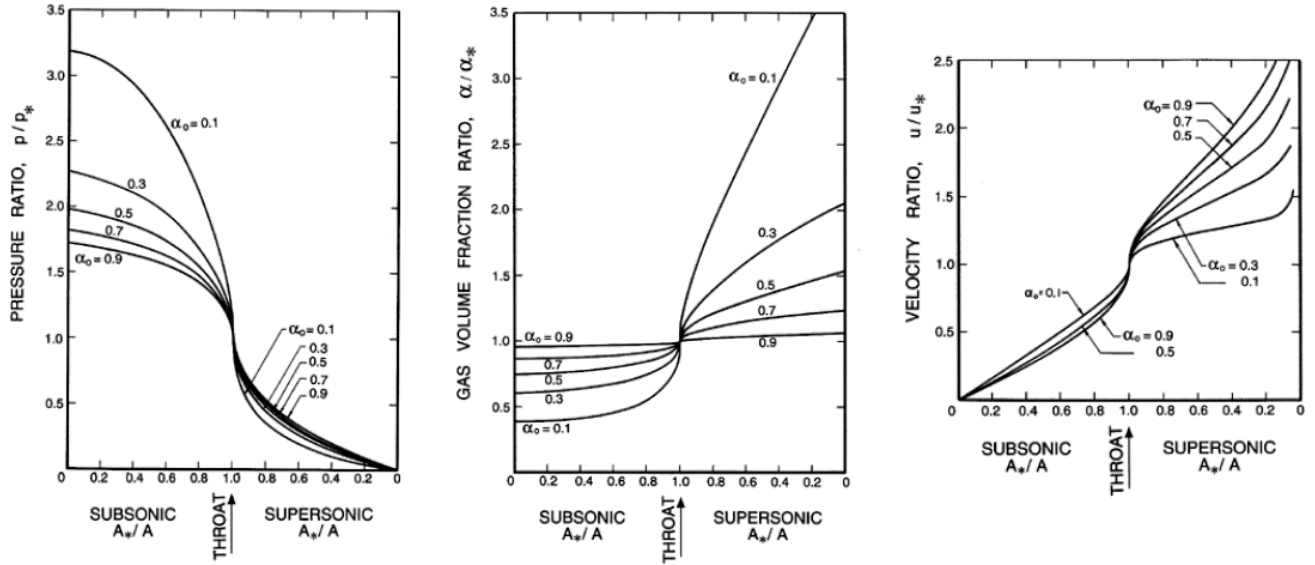


Fig. 1.5 Pressure, gas volume fraction and velocity ratios for a two-component flow with a nozzle with $k=1$ (Brennen, 1994)

As it is possible to notice from the graphs, the effect of the throat on the flux causes a great decrement of pressure nearby the nozzle and a corresponding and almost symmetrical increment in velocity. The increment is in both cases higher for lower reservoir void fractions, whose variability has more considerable effects for pressures before and for velocities after the throat section. A quite different tendency is shown by the gas volume ratios at the nozzle, that have in general an increase which is very relevant for small initial void percentages, as in many of the cases of interest for cavitation, and almost unperceivable for very high α_0 . The increase of the gas volume fraction can be intended as the vaporisation of also relevant portions of the fluid which produces the bubbles in the cavitation phase. The cavitation phase follows the passage of the fluid trough the nozzle as it is the effect of the pressure decrease. It is significant to notice that the possible very sudden change in the duct section can allow to produce these wide variations of the mechanical parameters in very short lengths and reduced times, as in the test setup of the experimental campaign carried out.

As a further note it is said that, as the pressure in the throat section p^* is evaluated by equating the expressions of u and c as functions of p (and not only of p_o) by imposing $p = p^*$, in the same condition, the critical one, also the choked mass flow rate \dot{m}_c can be evaluated:

$$\frac{\dot{m}_c}{A_*(p_o\rho_o)^{1/2}} = k^{1/2} \frac{\alpha_o^{k/2}}{(1 - \alpha_o)^{\frac{k+1}{2}}} \left(\frac{1 - \alpha_*}{\alpha_*} \right)^{\frac{k+1}{2}} \quad (1.20)$$

Having treated firstly the piezonuclear reactions in the condensed matter and then the cavitation phenomenon and the dynamic of bubbles, by exploiting in particular the potentialities of the nano-bubbles, it is possible to pass to the experimental part of the dissertation, starting from the results obtained in the previous years.

Chapter 2

Neutron emission and first calorimetric experimental results

2.1 Experimental setup

The first experimental tests about the effect of hydrodynamic cavitation on the production of low energy nuclear reactions in water solutions with metal salts was carried out at Politecnico di Torino until September 2014 on a cavitation reactor constituted by a plastic tank, a volumetric pump and high-density polyethylene ducts. From these first attempts, it was found the important evidence of neutron emissions, changes in concentrations of the metal ions in solution and extra-heat generations during the experimental tests.

In 2016 the design phase of a new cavitation plant started, aimed to investigate the heat generation that derives from the piezonuclear reactions of the metal ions dispersed in the ultra-pure water. This cavitation reactor was composed by a main duct made of a series of segmental plexiglass elements connected with each other by means of PTFE thread seal tape and four continuous screws fixed just at the two ends. The four passing screws were introduced to ensure a constant total length of the main duct and an adequate contrast to the high testing pressures. A bottom steel plate allowed to fix each plexiglass segment with the lower steel guide. The segmental configuration of the main duct, including the cavitation room containing the brass nozzle called “cavitator”, permitted to change its total length, as well as to insert additional measuring devices, depending on the needs required during the tests. During the prelaminar design of the cavitation reactor, it was chosen that the main duct needed to be made of plexiglass in order to guarantee a higher transparency for the successive optic tests and to avoid the water contamination caused by metal ions released by the presence of metallic parts. Together to the main duct, the plant was also composed of the water tank, made of the same material of the ducts (i.e. plexiglass), which receives the water coming from the main duct after the cavitation process. The water tank was also connected to the other main components of the system, such as a three-phase electric volumetric pump and a PVC tube, which connects the pump to the cavitation duct. The pump, which pulls the water out of the tank and sends it again to the main duct in a closed cycle, was chosen to reach

absolute pressures up to 20 bar (model AR 45 bp EM, CC31222 three-phase) and to have all the components in contact with water made of polymeric material. The pump is equipped by a security by-pass aimed to avoid potentially dangerous excessive pressures within the cavitation reactor. The security bypass activates at a pressure of about 15 bar. Figs. 2.1-2.4 show the cavitation plant and its main components.

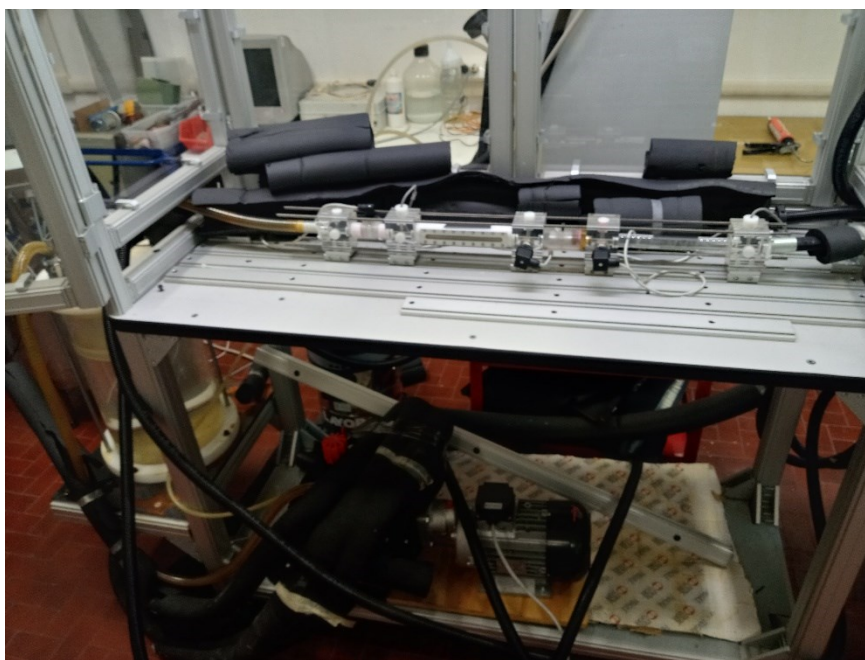


Fig. 2.1 Overall image of the plant (open).

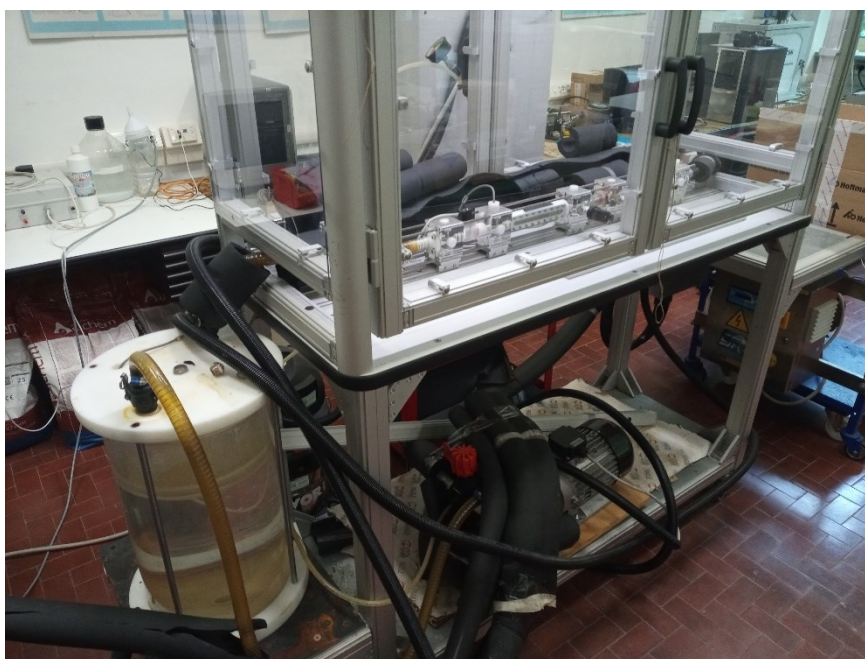


Fig. 2.2 Overall image of the plant (closed).

Just to give the order of magnitude of the dimensions of the parts of the main duct, the cavitation segment is 8 cm long and 4 cm wide, while the plexiglass cubes hosting thermometers and measurement devices have 6 cm long sides (see Fig. 2.3).

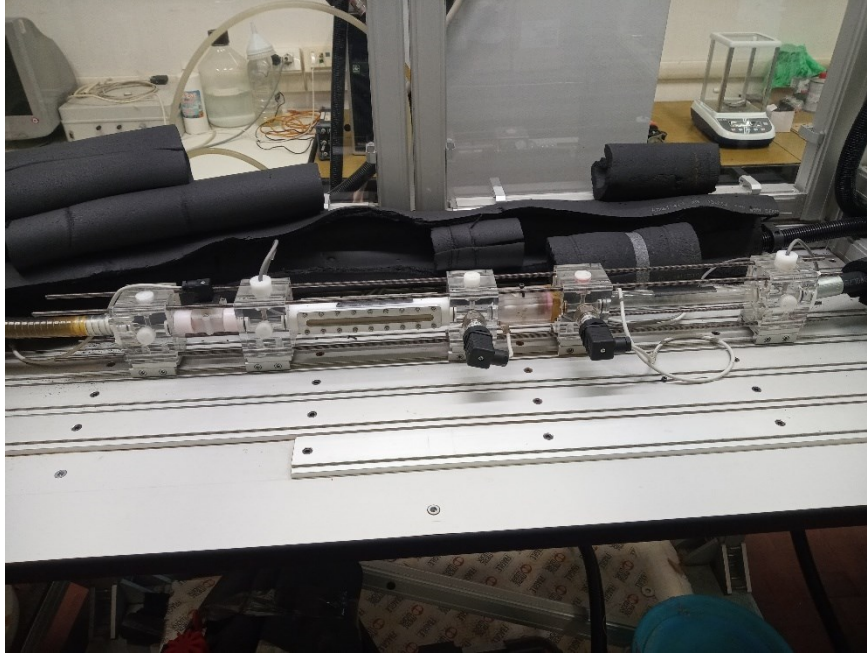


Fig. 2.3 Main duct of the plant.

Regarding the monitoring system, the plant was equipped with several different sensor typologies. More in detail, four temperature sensors were installed in different position along the cavitation reactor. Two thermocouples are placed 30 cm before and after the cavitator with the aim to measure the temperature increment in the fluid due to the effect of both piezonuclear reactions that develop as a consequence of the cavitation process and the mechanical action of the pump. The third thermocouple is then located within the tank. The difference in temperature measured between the thermometer before the cavitator and the thermocouple in the tank is the fundamental parameter to be evaluated for describing the energy produced by the cavitation reactor and its efficiency. During the design of the cavitation reactor, it was chosen to adopt a sampling frequency for the temperature measurements equal to six acquired data per each minute.

The pressure of the fluid is measured by two pressure gauges that are placed just before and after the cavitator in order to evaluate the pressure drop caused by the nozzle (Fig. 2.4). Furthermore, the cavitation plant is equipped by a flow measurement device, that measures the fluid velocity in a cross-section of the main duct located after the cavitator. The flux is then automatically evaluated by the product between the measured speed and the known area of the monitoring section.

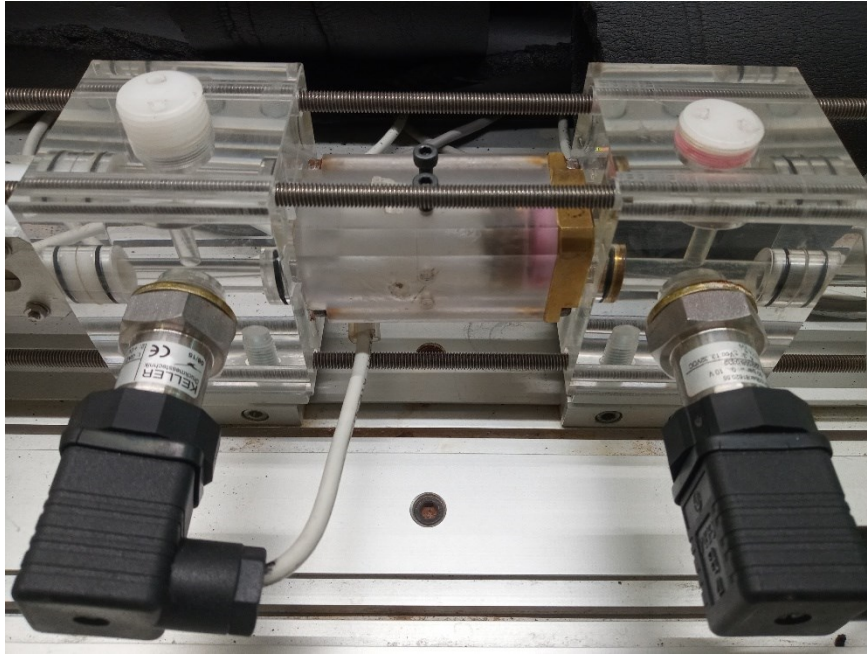


Fig. 2.4 Detail of the cavitation segment with the plexiglass cubes, the pressure gauges, and brass cavitator.

These measurement devices were connected to a control unit, which allows to save the acquired experimental data with a predetermined time interval (Fig. 2.5). It is worth to highlight that the same control unit is able to acquire the electric power given by each phase of the pump also (by means of a SIEMENS PAC3200 device), so that the total absorbed electric energy by the cavitation plant can be recorded with a sampling frequency of one value per each minute. Eventually, the cavitation plant can be equipped with a neutron emission detector. The detection of neutron emissions was accomplished by using a He^3 neutron proportional counter produced by the industrial company Xeram (France). The neutron emission detector was composed of a He^3 detector tube and an electronic system of preamplification, amplification and discrimination of the acquired signal [20]. It was powered with an electrical tension of 1.3 kV by means of a high voltage Nuclear Instrumentation Module (NIM) [14] [20]. The logic output which produces the Transistor-Transistor Logic (TTL) pulses was connected to a NIM counter. Since the He^3 counter is also sensitive to gamma rays, X rays and electrons, a threshold value was set for the received signals [14] [20]. The device was directly calibrated by the company for the detection of thermal neutrons; its sensitivity was $65 \frac{\text{cps}}{n_{\text{thermal}}} = 65 \frac{\text{s}^{-1}}{n_{\text{thermal}}}$ with a declared variability of $\pm 10\%$, which corresponds to a flux of one thermal neutron per second and square centimetre ($1 \frac{n_{\text{thermal}}}{\text{s cm}^2}$) [12] [20] [21].



Fig. 2.5 Monitoring computer and pump electric power control unit.

In Fig. 2.6a the hydraulic scheme of the cavitation reactor is portrayed, and in Fig. 2.6b the respective legend according to the actual Italian regulation.

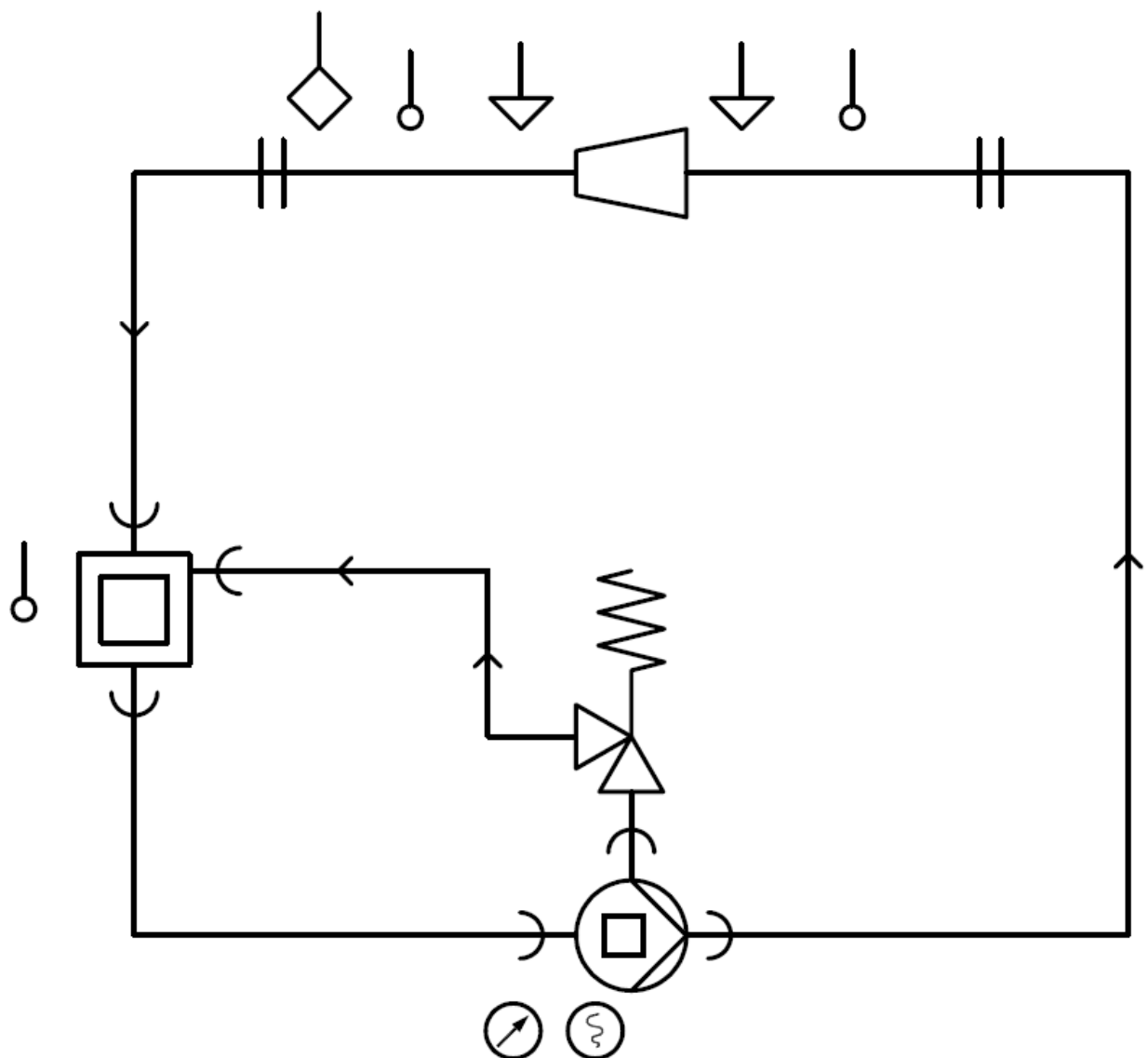


Fig. 2.6a Hydraulic scheme of the cavitation reactor.

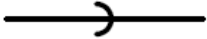











Nomenclature according to UNI 9511 regulation (effectively adopted nomenclature)	Simbolo
Spigot joint	
Flange joint	
Flux way	
Concentric reduction (Cavitator)	
Storage tank (Tank)	
Safety valve (Bypass)	
Volumetric pump	
Temperature probe (Thermocouple)	
Pressure detector	
Flow rate detector	
Direct-lecture indicator device	
Recording device	

Fig. 2.6b Legend of the symbolism adopted for the hydraulic scheme.

2.2 Energy balance assessment

Let us analyse the possibility of exploitation of the piezonuclear reactions for the heat production. To this aim, the assessment of all the energy input and output contributions with a good accuracy was strictly mandatory in order to assess the energy balance of the cavitation reactor over a preassigned time interval after that the steady state condition is reached. In our analysis, the reference time interval was set equal to one hour, i.e. $\Delta t = t_e - t_i = 3600$ s.

The input energy contribution coincided with the total electric energy supplied to the pump by the grid and it was evaluated by means of the product between the average electric power provided for the three-phase pump, \bar{W}_{el} , and the reference period:

$$E_{in} = \bar{W}_{el} \times 3600 \text{ s} \quad (2.1)$$

The average electric power \bar{W}_{el} was calculated as the mean value on the reference time in steady-state condition of the total electric power absorption, which was equal to the sum of the powers provided to each one of the three phases of the pump engine for every acquisition interval (one minute).

The output energy was evaluated by the sum of three terms, that are the thermal energy stored by the water solution, E_w , the thermal energy dispersed in the environment, E_{disp} , and the mechanical energy dissipated by the cavitator, E_{mec} :

$$E_{out} = E_w + E_{disp} + E_{mec} \quad (2.2)$$

These three quantities were assessed once the steady state condition is reached.

In particular, the thermal energy stored by the water in a full cycle was evaluated by applying the heat transfer formula:

$$E_w = m_w c_w \Delta T_1 \quad (2.3)$$

where m_w is the total mass of the water solution, c_w is the specific heat capacity of the water, which is equal to $4186 \frac{\text{J}}{\text{kg K}}$, and the term ΔT_1 represents the temperature difference measured between the tank and the section of the main duct 30cm before the cavitator. The temperature difference was considered after the reaching of the steady-state condition.

The thermal energy dispersed in the environment by the cavitation plant was evaluated by referring to the conduction, convection and irradiation phenomena:

- Conduction (Fourier's Law)

$$\dot{E}_{cond} = 2\pi L \lambda \frac{\Delta T_c}{\ln(r_e/r_i)} \quad (2.4)$$

where \dot{E}_{cond} is the thermal flux dispersed by effect of the conduction mechanism, L is the length of the cylindrical layer of the duct, λ is the thermal conductivity of the material, r_e is the external radius of the layer, r_i is the internal radius of the layer and ΔT_c is the temperature difference between the internal and the external surfaces of the layer itself.

Starting from Eq. 2.4, it was possible to determine the thermal conduction resistance of the cylindrical layer, R_{cond} , as follows:

$$R_{cond} = \frac{\ln(r_e/r_i)}{2\pi L \lambda} \quad (2.5)$$

- Convection (Newton's Law)

$$\dot{E}_{conv} = h A (T_f - T_{si}) \quad (2.6)$$

where \dot{E}_{conv} is the thermal flux dispersed by effect of the convection mechanism, h is the convective heat transfer coefficient, A is the area of the cylindrical surface in contact with the fluid, T_f is the temperature of the fluid and T_{si} is the temperature of the internal solid surface. The internal convective heat transfer coefficient was assessed as a function of the velocity of the water solution and of several other parameters by means of the dimensionless numbers of Rayleigh, Prandtl and Nusselt on the internal side of the duct, subjected to forced convection. The Rayleigh number was evaluated according to the following expression:

$$Ra = \frac{V D}{\nu_w} \quad (2.7)$$

where V is the fluid velocity, D is the internal diameter of the duct and $\nu_w = 1 \times 10^{-6} \frac{m^2}{s}$ is the cinematic viscosity of water. For the sake of simplicity, the lowest of the internal diameters of the ducts constituting the plant was considered as D , and this constituted a conservative choice for the evaluation of the final convective coefficient.

The Prandtl number was then calculated according to the next equation:

$$Pr = \frac{\nu_w \rho_w c_w}{\lambda_w} \quad (2.8)$$

where $\rho_w = 1000 \frac{kg}{m^3}$ is the density and $\lambda_w = 0.60 \frac{W}{m K}$ is the thermal conductivity of water.

In the calculations accomplished for the following evaluations of the internal convective coefficient, the Prandtl number was always considered to assume the value of 6.98.

The Nusselt number was estimated with reference to the Böhm empirical expression related to the forced convection case, depending on the Rayleigh number:

$$Nu = 0.0033 \times Ra \times Pr^{0.33} \quad (2.9)$$

The formulation was proposed to be applied for $3000 \leq Ra \leq 30000$.

Therefore, the convective heat transfer coefficient for the internal water flux, h_i , was evaluated as follows, as a function of the thermal conductivity of water, of the internal diameter of the duct and of the Nusselt number:

$$h_i = \frac{\lambda_w}{D} Nu \quad (2.10)$$

On the external side of the duct, the widely proposed value of $5 \frac{W}{m^2K}$ for air in natural convection condition was adopted as the external convective heat transfer coefficient, h_e .

The thermal convection resistance, R_{conv} , was then obtained from the Newton's Law:

$$R_{conv} = \frac{1}{h A} \quad (2.11)$$

- Irradiation (Stefan-Boltzmann's Law)

$$\dot{E}_{irr} = \varepsilon \sigma A (T_{se}^4 - T_a^4) \quad (2.12)$$

where \dot{E}_{irr} is the thermal flux dispersed by effect of irradiation, ε is the surface emissivity, $\sigma = 5.67 \times 10^{-8} \frac{W}{m^2K^4}$ is the Stefan-Boltzmann's constant, T_{se} is the temperature of the external solid surface and T_a is the environmental temperature.

The sum of the conduction and convection thermal resistances allowed to evaluate the equivalent thermal resistance of the whole duct, R_{eq} , as follows:

$$R_{eq} = R_{conv,i} + \sum_{j=1}^n R_{cond,j} + R_{conv,e} \quad (2.13)$$

where $R_{conv,i}$ is the internal convection resistance of the duct, $R_{conv,e}$ is the external convection resistance of the duct, $R_{cond,j}$ is the conduction resistance of the j -th layer and n is the number of the layers constituting the duct. The thermal flux dispersed by effect of conduction and convection, \dot{E}_{cc} , could then be obtained in the following way:

$$\dot{E}_{cc} = \frac{\Delta T_2}{R_{eq}} \quad (2.14)$$

where ΔT_2 is the difference between the temperature of the internal fluid and the external environmental one.

Once the thermal flux \dot{E}_{cc} had been known, it became possible to apply the inverse expression of the equivalent formulation of Eq. 2.14 to determine the temperature profile from the inner water solution to the external surface of the duct. The external temperature of the duct evaluated in this way was then substituted in Eq. 2.12 to assess the irradiation contribution to the thermal dispersion. Therefore, the total thermal flux dispersed by the cavitation reactor was estimated as follows:

$$\dot{E}_{disp} = \dot{E}_{cc} + \dot{E}_{irr} \quad (2.15)$$

where \dot{E}_{disp} is the total thermal flux dispersed by effect of conduction, convection and irradiation and \dot{E}_{irr} is the thermal flux dispersed by irradiation only.

The thermal energy dispersed by the plant in the reference period of one hour, E_{disp} , could be finally evaluated:

$$E_{disp} = \dot{E}_{disp} \times 3600 \text{ sec} \quad (2.16)$$

In order to perform the assessment of the thermal dispersions related to the cavitation reactor activity, the plant was discretised a series of three ducts characterised by different lengths, internal and external diameters and also materials. The three ducts were intended as analytical representations of the hydraulic system, which is constituted by the main duct (made of plexiglass), the PVC tubes including also the internal parts of the pump, that are made by the same material and are characterised by the same diameters, and the cylindrical plexiglass tank. All the ducts of the plant are constituted by a single layer of polymeric material; two layers were adopted just for the tank in insulated conditions, when it had been externally enveloped by the Polyflex-Molubrik insulating material. In Tab. 2.1 the geometrical parameters which were adopted for the three ducts considered in the analytical representation of the cavitation reactor for the evaluation of the thermal dispersions are given, where L is the length of the pipe, \varnothing_{int} is the internal diameter of the layer in contact with the fluid, \varnothing_{est} is the external diameter and t is the thickness of the layer.

Main duct	
L (m)	1.10
\varnothing_{int} (m)	0.0116
\varnothing_{est} (m)	0.0209
t (m)	0.00465
PVC tubes and pump	
L (m)	9.70
\varnothing_{int} (m)	0.0116
\varnothing_{est} (m)	0.0265
t (m)	0.00745

Tank	
L (m)	0.40
\varnothing_{int} (m)	0.290
\varnothing_{est} (m)	0.300
t (m)	0.005
Insulating material (Polyflex)	
t (m)	0.019

Tab. 2.1 Geometrical parameters of the analytical representation of the plant for thermal dispersions

For the three materials considered, the thermal conductivities of Tab. 2.2 were adopted.

$\lambda_{PLEXIGLASS} \left(\frac{W}{m \cdot K} \right)$	0.190
$\lambda_{PVC} \left(\frac{W}{m \cdot K} \right)$	0.159
$\lambda_{POLYFLEX} \left(\frac{W}{m \cdot K} \right)$	0.038

Tab. 2.2 Thermal conductivities of the materials constituting the cavitation reactor

The third output energy contribution was the mechanical dissipation of the cavitator, E_{mec} . This term was given by the product between the reference period and the dissipated hydraulic power, W_{hyd} , which was assessed as the product of the pressure drop in correspondence of the cavitator, ΔP , and the volumetric flow rate of the main duct, Q :

$$W_{hyd} = \Delta P Q \quad (2.17)$$

$$E_{mec} = W_{hyd} \times 3600 \text{ sec} = \Delta P Q \times 3600 \text{ sec} \quad (2.18)$$

From a simple comparison between the input energy, E_{in} , and the output one, E_{out} , it would be found that a difference between these two terms exist. In fact, in the previous thermal balance it was not explicitly considered the most interesting energetic contribution for the aim of this thesis, the heat generation produced by the piezonuclear reactions in the metal ions in solution induced by the cavitation phenomenon. As a consequence, the energy balance would have been completely satisfied when an addition term, called in the following E_X , would have been explicitly considered [3]. Therefore, the following correct energy balance expression could be written:

$$E_{in} + E_X = E_{out} \quad (2.19)$$

The heat generation by Low Energy Nuclear Reactions (LENR) in the liquid medium E_X was evaluated in an implicit way by introducing the Coefficient Of Performance (COP), the parameter

which expresses the efficiency of a thermodynamic system as the ratio between the measured output energies and the supplied input in steady-state conditions:

$$COP = \frac{E_{out}}{E_{in}} \quad (2.20)$$

Values of the COP greater than one imply that the total amount of output energy exceeds those provided to the cavitation reactor as electric energy. In other words, values of the COP greater than one in the cavitation plant can be considered as the effect of another form of energy contribution, that in the case of interest were identified in the piezonuclear reactions. Thus, the COP was a parameter of paramount importance for the present studies, since it measured the energetic efficiency of the cavitation reactor and on the other hand it made an indirect estimate about the role of LENR on heat generation due to the cavitation phenomenon.

2.3 Experimental results of the neutron emission on the non-insulated plant equipped by plastic cavitators

The first calorimetric tests, carried out between June 2016 and May 2017, were performed by employing a plastic trial cavitator, which is portrayed in Fig. 2.7.

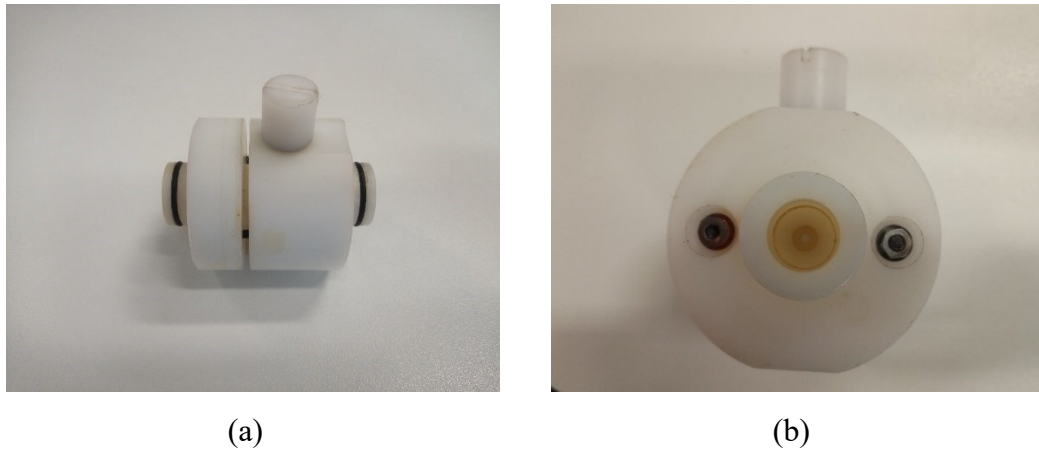


Fig. 2.7 Plastic cavitator for the first calorimetric tests: (a) lateral view; (b) front view.

The experimental tests were firstly accomplished on the plant in non-insulated conditions, as shown in the previous images. More in detail, the first attempts were performed with the aim to understand if the LENR induced by the cavitation phenomenon could be at the origin of observed extra heat generation. To this aim, it was used a mass 22 kg of ultra-pure water enriched by 0.11 mg

of iron(III) chloride (FeCl_3) in order to obtain a solution concentration equal to 5 ppm. Tests with higher concentrations of iron salts, carried out in the preliminary experimental phases to verify the possibility of higher heat productions, as theoretically suggested, were then abandoned due to the observed precipitation and deposition of the salts on the surfaces of the plant. Therefore, the concentration adopted was chosen as the optimum for the necessities of the calorimetric tests and for avoiding possible damages. Eventually, it is worth to emphasise that the choice of iron salts rather than other metal ones was accomplished because of the considerable number of research performed about piezonuclear reactions at Politecnico di Torino on solid and liquid (electrolysis) media in the previous years.

During the experimental tests, measurements of the thermal neutron flux and the compositional changes in the water solution were accomplished. Fig. 2.8 shows the neutron count rate evolution during the first experimental test, which is compared with the average measured background level. From this figure, it is evident that the cavitation phenomenon has been able to generate some anomalous neutron emissions with several important deviations from the average background level. This experimental evidence can be more appreciated in Fig. 2.9, where the cumulative curves for the neutron emission counts are reported. It was observed that the total counts value, monitored while the cavitation reactor was operating, was approximately 34.4% higher than the value measured for the neutron background level.

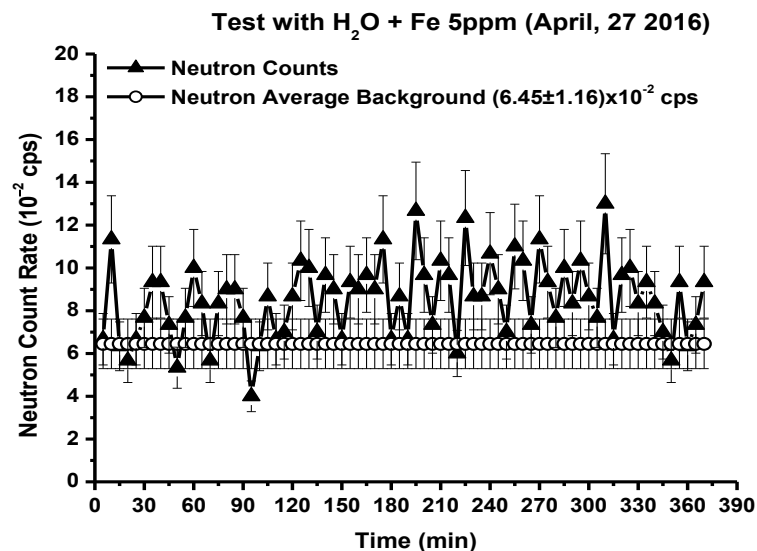


Fig. 2.8 Thermal neutron flux from test of April 27, 2016.

The release of thermal neutrons during cavitation is a strong evidence of the occurrence of piezonuclear reactions in the water solution, caused by the violent implosion of the bubbles, and especially of the nano-bubbles, triggered by the cavitation.

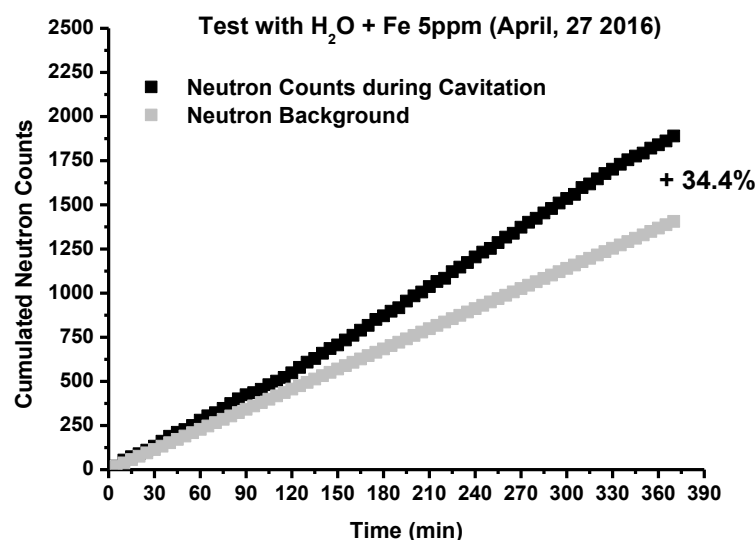


Fig. 2.9 Cumulative curve for the neutron emissions from test of April 27, 2016.

As a further confirm of the nuclear nature of the recorded neutron emissions, chemical composition analyses of the water solution were carried out on six samples (one each 60 minutes) in terms of iron and aluminium concentrations (see Fig. 2.10). The chemical compositional analyses showed a significant decrease in iron concentration of about the 20% at the end of the test and a simultaneous relevant growth in the aluminium concentration, which increased from a value slightly higher than 5 ppb up to 10 ppb at the end of the test.

Therefore, by considering the observed neutron emissions and compositional changes in the water solution enriched by iron salts, the capability of the hydrodynamic cavitation in producing piezonuclear reactions was confirmed, allowing thus to plan more deepened tests to evaluate the potentialities of the consequent heat generations.

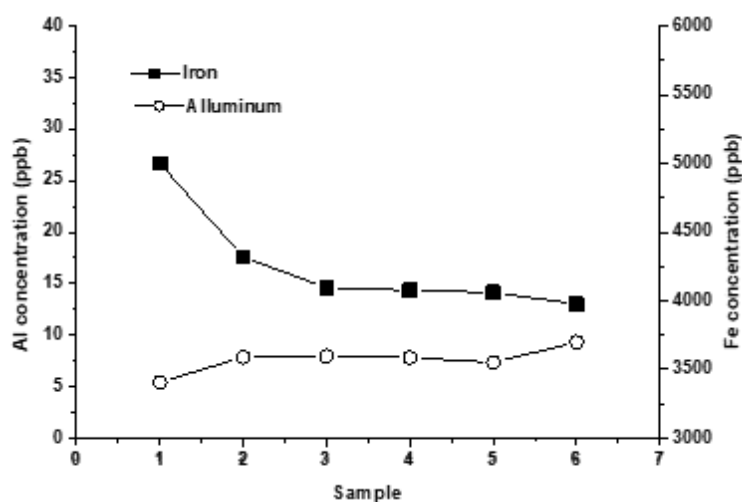


Fig. 2.10 Chemical compositional changes of elements in solution from test of April 27, 2016.

After these preliminary attempts, further experimental tests were accomplished between October and November 2016 with the same cavitator of Fig. 2.7 to perform calorimetric and neutron emission measurements. In Fig. 2.11 the measurements of the thermal neutron flux detected in the experimental test in October 2016 are depicted, which show important punctual increments with respect to the average background level. On the other hand, it has been observed an increase in the cumulative curves for the neutron emission counts of about 35.3 % with respect to the environmental background (Fig. 2.12).

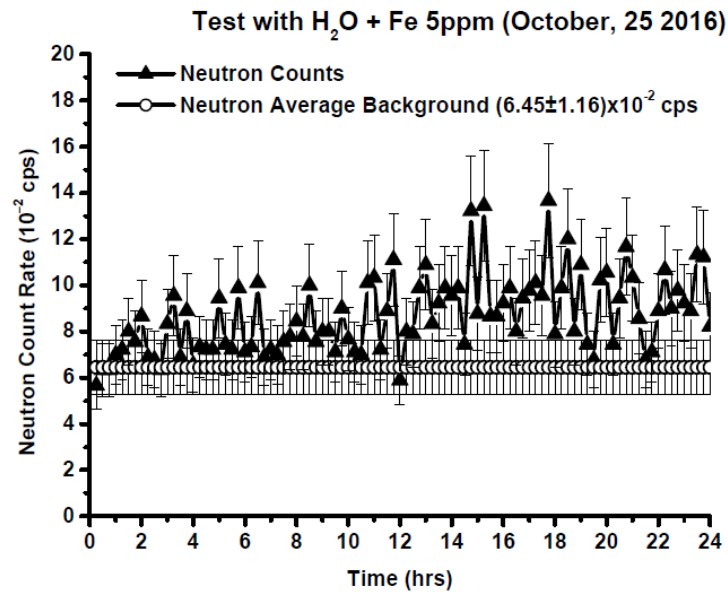


Fig. 2.11 Thermal neutron flux from test of October 25, 2016.

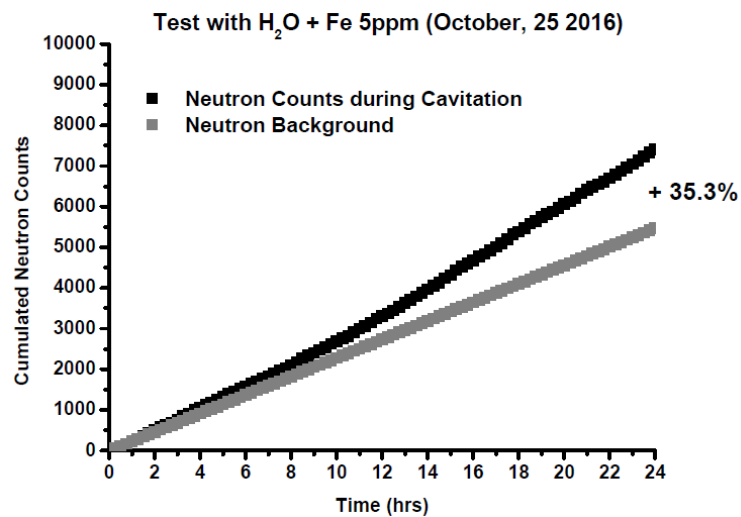


Fig. 2.12 Cumulative curve of neutron emissions from test of October 25, 2016.

Simultaneously, the temperatures of the water solution were measured and acquired every 10 seconds in the plastic tank and the section of the main duct before the cavitator for about 51 hours. More in detail, 25 hours was the duration of the experimental test, while 26 hours was the time required by the water solution to reach the environmental temperature after the turning off of the cavitation reactor (see Fig. 2.13).

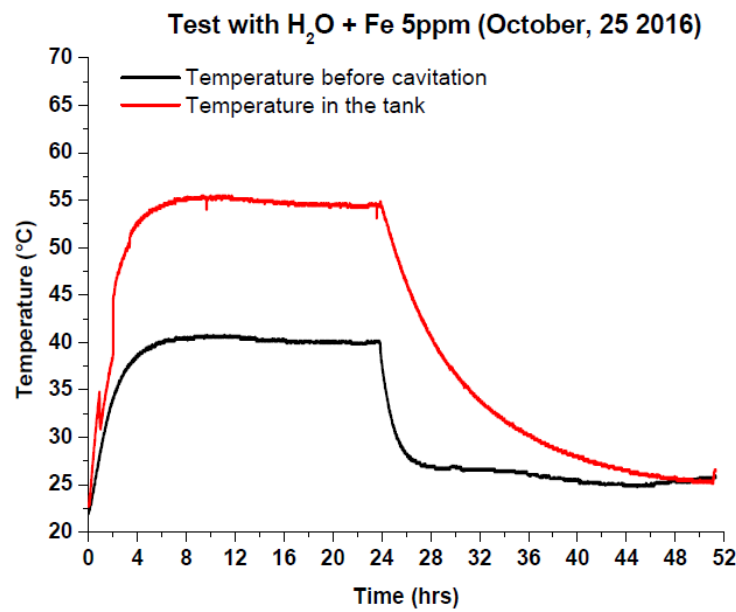


Fig. 2.13 Temperature profiles from test of October 25, 2016.

From this figure, it is possible to notice that the steady-state condition temperature in the tank was reached after about 8 hours, with a final value of 55°C (red curve of Fig. 2.13); an analogous trend was obtained for the measured temperature before the nozzle (black curve of Fig. 2.13). The temperature increase, produced both by the mechanical action of the pump and by the piezonuclear reactions in the solution during the cavitation, is evident by a comparison between the red and black curves of Fig. 2.13, in which it is possible to observe a difference in the steady-state condition temperatures of about 15°C.

During the test, the power absorbed by each phase of the volumetric pump was acquired by the control unit, and it is shown in Fig. 2.14. Firstly, the obtained curves were analysed in order to evaluate possible instabilities of the electrical supply of the pump on the calorimetric results. From Fig. 2.14, it is evident that negligible differences were found in terms of the average value of the total absorbed electric power during the test, except for the starting transient phase. As a matter of fact, no significant differences were found in terms of the water solution temperature once the steady-state condition was reached.

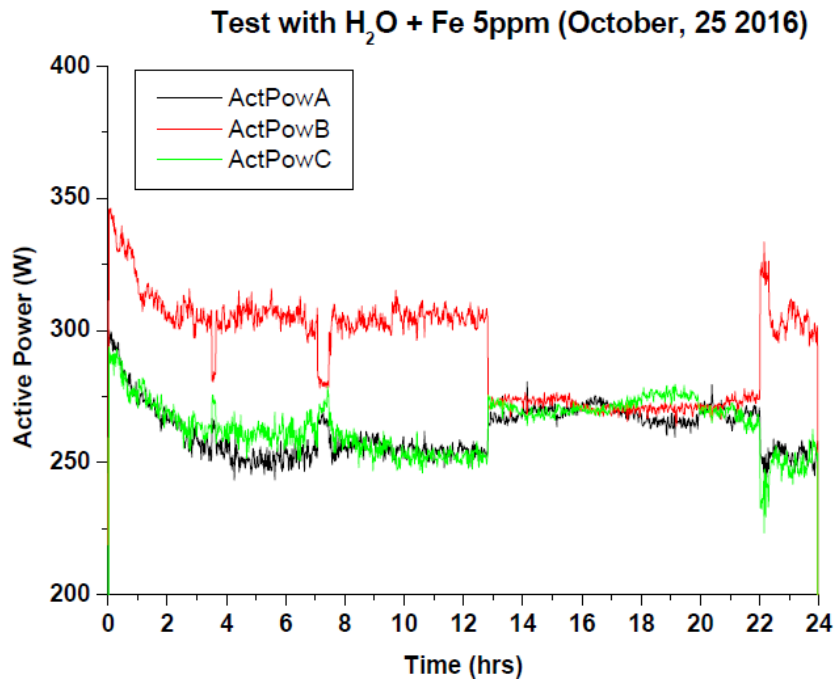


Fig. 2.14 Electric power provided by the three-phase pump from test of October 25, 2016.

A successive test performed for a shorter duration of 10 hours on the 28th of October 2016 allowed to observe the neutron emissions portrayed in Fig. 2.15, which revealed peaks greater than the background level of about 2.5 times. By considering the cumulative curve of Fig. 2.16, it was possible to measure a positive deviation from the cumulate of the neutron environmental radiation level of about 23.3%.

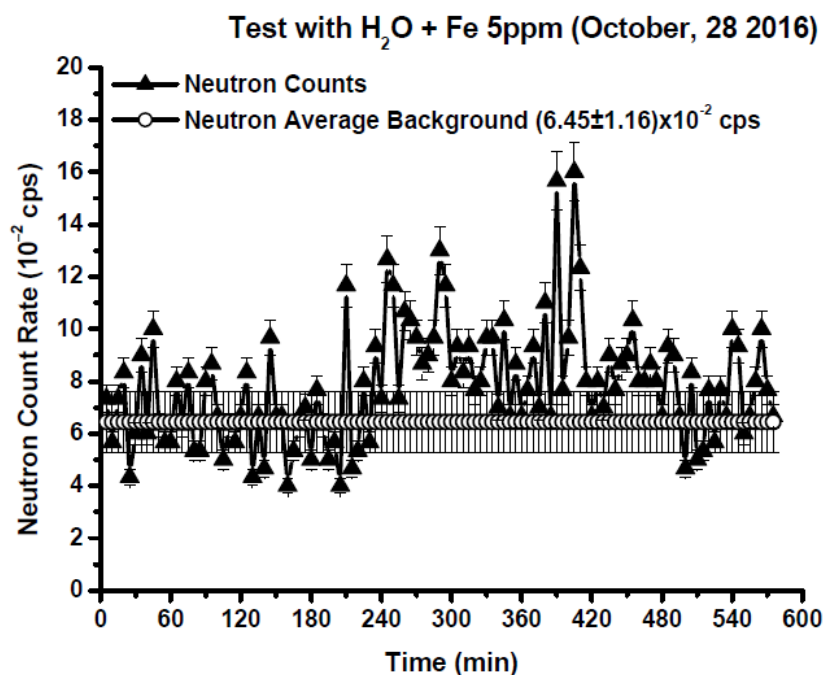


Fig. 2.15 Thermal neutron flux from test of October 28, 2016.

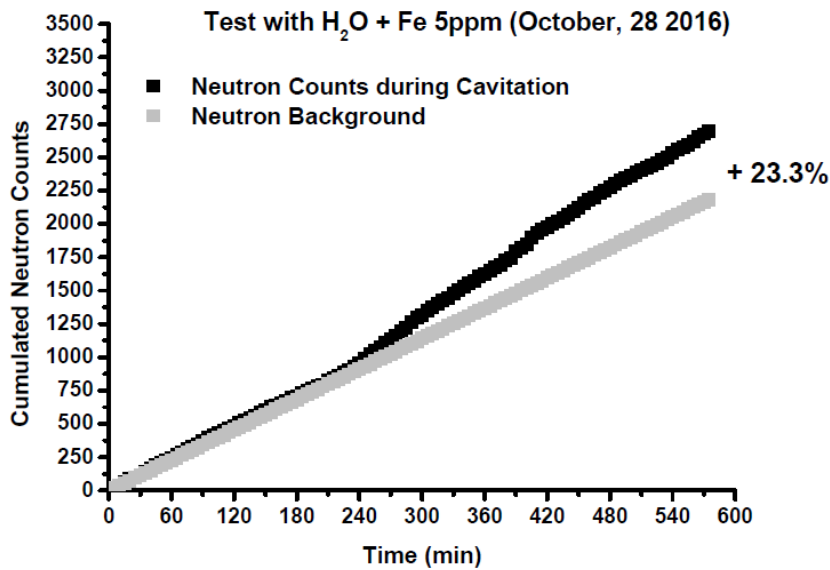


Fig. 2.16 Cumulative curve of neutron emissions from test of October 28, 2016.

At the same time, the temperature trends shown in Fig. 2.17 were registered, which in this case interrupted after having reached the steady-state conditions.

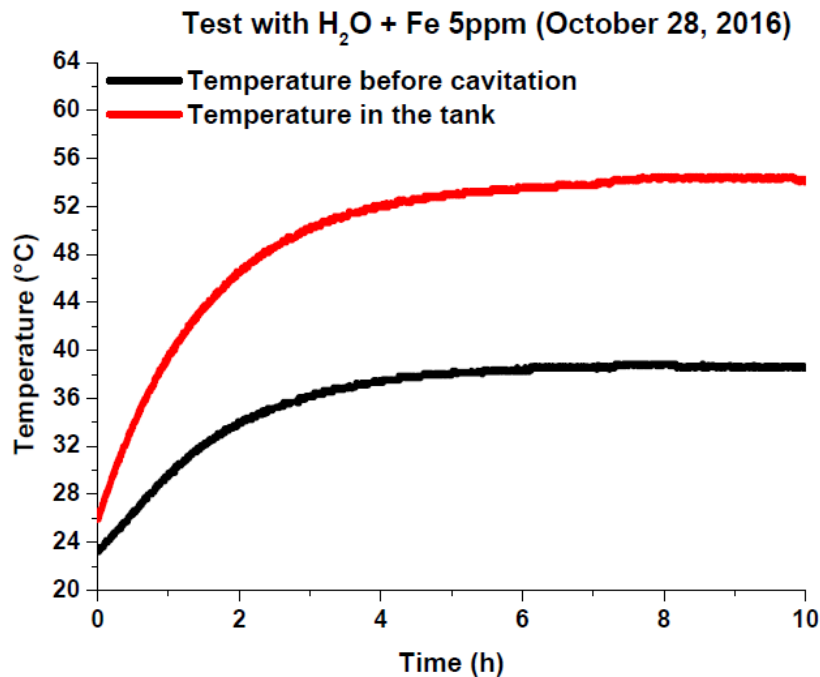


Fig. 2.17 Temperature profiles from test of October 28, 2016.

From the previous graph it is possible to notice that, similarly to the previous test, the steady-state condition was reached at about 55°C after 8 hours of test, with difference in temperatures of about 15°C (a little bit higher in this case).

The curves of the powers absorbed as electric supply of the three phases of the pump are then reported in Fig. 2.18. The observations previously done about the constancy of the average value after the transient phase were recognised to be still valid.

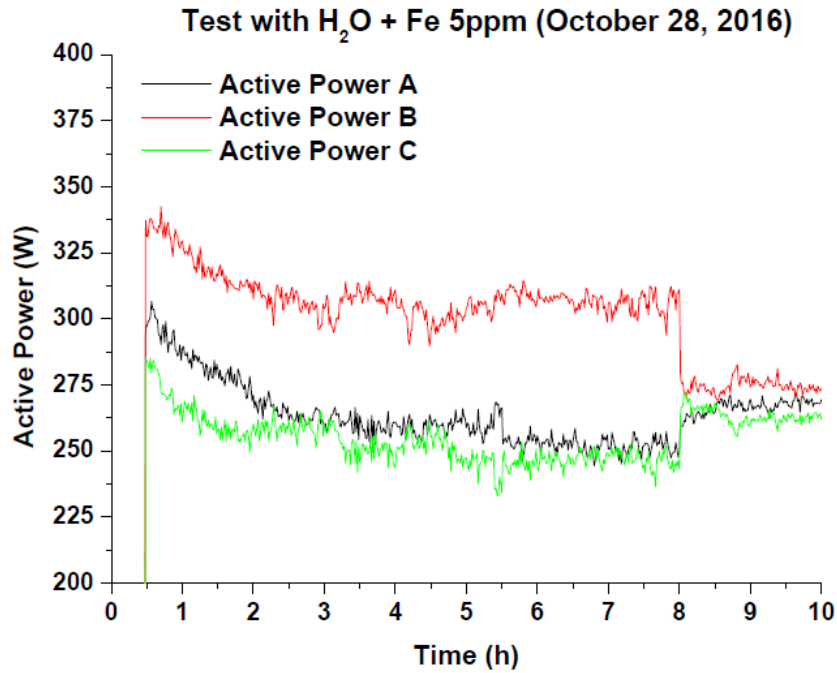


Fig. 2.18 Electric powers provided to the three-phase pump from test of October 28, 2016.

2.4 Calorimetric results on the plant equipped by plastic cavitators according to the indirect method

Once the initial neutron emission monitoring phase had ended, it was decided to improve the performances of the system by reducing the high heat losses from the plant to the environment by means of a convenient thermal insulation system.

It is worth noting that the insulation of the cavitation reactor was intended to allow the reaching of higher steady-state temperatures of the plant to be after exploited in the industrial field, and it was not conceived as a way to obtain an increase the COP of the system. Indeed, by considering for the evaluation of the COP all the energy contributions introduced in Paragraph 2.2, from the theoretical perspective the COP for the insulated and the non-insulated plant for the same pump turning velocity would be exactly the same, since the increase of the energy stored by the water (E_w) would be balanced by the decrease of the thermal dispersion in the environment (E_{disp}).

The Poliflex-Molubrik was chosen as an insulating material, since it is widely used in the industrial field. More in detail, all the components of the plant were covered with this insulating material, including the main plexiglass duct, the other PVC ducts, the plastic tank and the pump.

The only exception was constituted by the pump cooler. Some photos of the insulated system are shown in Fig. 2.19-2.20.



Fig. 2.19 Insulated plant: Thermal insulation of the main duct.



Fig. 2.20 Insulated plant: (a) Thermal insulation of the tank (b) Thermal insulation of the pump..

Subsequently to the insulation of the cavitation plant, a new series of experimental tests was planned by adopting the plastic cavitator of Fig. 2.7. In order to determine the optimal pump turning velocity in terms of evaluated COP, a series of attempts was accomplished by starting from a reduced velocity of the pump (and so reduced electric power supplies and input energies E_{in}) and then gradually increasing it in different tests until the achievement of the optimum value, the one producing the highest COP. In Tab. 2.3 the Rayleigh and Nusselt numbers and the internal convection heat transfer coefficients for the tests on the plastic cavitator are reported.

Plastic cavitator	
October 2017 (350 rpm)	
Ra (-)	7317.47
Nu (-)	495.48
h_i ($\frac{W}{m^2K}$)	25628.20
October 2017 (400 rpm)	
Ra (-)	8232.15
Nu (-)	557.41
h_i ($\frac{W}{m^2K}$)	28831.71
October 2017 (500 rpm)	
Ra (-)	10061.52
Nu (-)	681.28
h_i ($\frac{W}{m^2K}$)	35238.75
November 2016 (700 rpm)	
Ra (-)	12805.57
Nu (-)	867.09
h_i ($\frac{W}{m^2K}$)	44849.33

Tab. 2.3 Rayleigh and Nusselt numbers, internal convection heat transfer coefficient, plastic cavitator.

The first attempt at reduced velocity on the insulated plant was done by imposing to the pump engine a value of 350 rpm (round per minute), and the temperature trends of Fig. 2.21 were obtained.

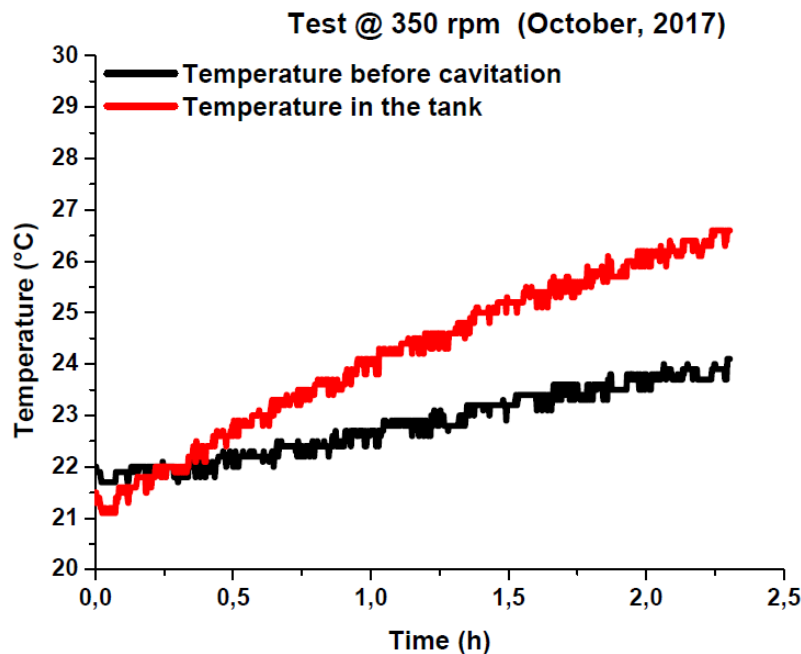


Fig. 2.21 Temperature trends for the first reduced-velocity test (350 rpm).

At about two hours and a half from the beginning of the test a difference in temperature of just 2.5°C was observed. The diagram of the input electric powers of the three phases of the pump is shown in Fig. 2.22.

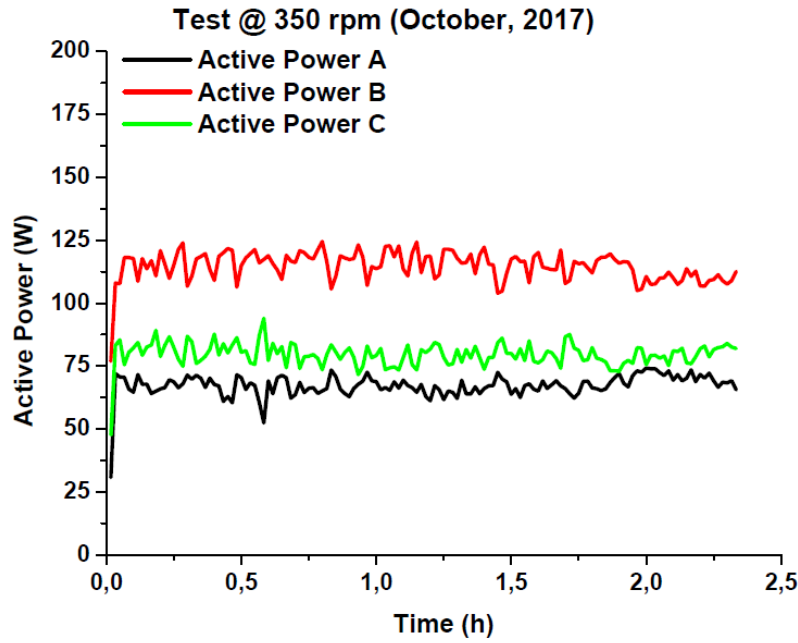


Fig. 2.22 Electric powers provided to the three-phase pump for the first reduced-velocity test (350 rpm).

The following physical quantities were adopted in the calculation of the energy contributions, having considered in the energy evaluations the average values on the last hour of the test (which was really still in transient phase) as the steady-state ones:

- mass of the water solution 22 kg;
- initial (environmental) temperature 21.0°C;
- last hour temperature before the cavitator 23.7°C
- last hour temperature after the cavitator 24.2°C
- last hour temperature in the tank 26.2°C;
- pressure drop in the cavitator 3.60 bar;
- electric power provided to the pump 260 W;
- pump rotation velocity 350 rpm;
- last hour flow rate of the plant 0.004 m³/minute;

On the bases of these data, the energy contributions were calculated as reported:

- | | |
|---|------------------------------|
| - Input electric energy absorbed by the pump | $E_{in} = 936.0 \text{ kJ}$ |
| - Thermal energy stored by water | $E_w = 230.2 \text{ kJ}$ |
| - Thermal energy dispersed in the environment | $E_{disp} = 37.7 \text{ kJ}$ |
| - Mechanical energy dissipated by the cavitator | $E_{mec} = 86.4 \text{ kJ}$ |

Consequently, the COP was evaluated, and it was found to assume in this case a value greatly lower than one, which indicated the absorption of a quantity of energy significantly higher than the released one:

$$COP = \frac{E_{out}}{E_{in}} = \frac{354.3 \text{ kJ}}{936.0 \text{ kJ}} = 0.38 \quad (2.21)$$

In the second reduced-velocity attempt, the three-phase pump turning velocity was set up at 400 rpm and the temperature curves portrayed in Fig. 2.23 were obtained.

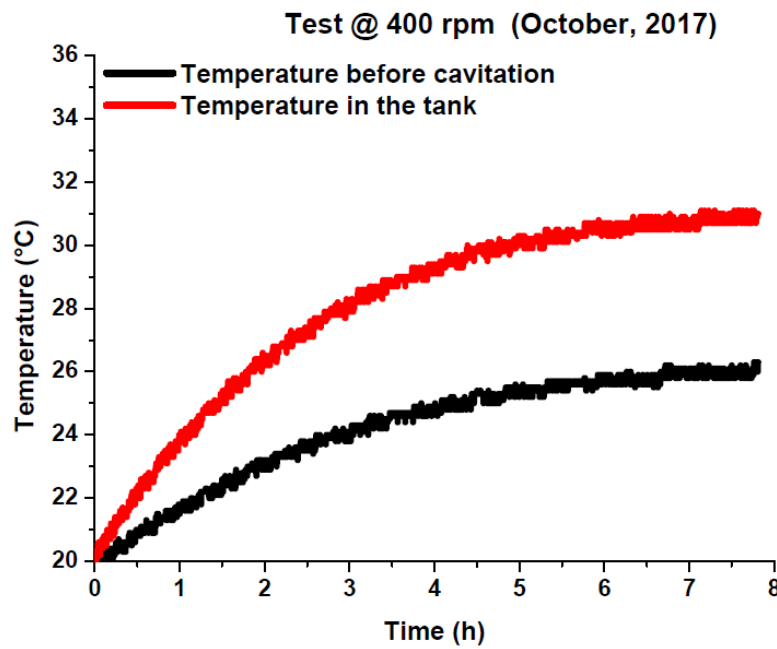


Fig. 2.23 Temperature trends for the second reduced-velocity test (400 rpm).

In this case the steady-state condition was reached. The history of the input electric powers is given in Fig. 2.24, as always with self-balanced anomalies between the powers of the different phases.

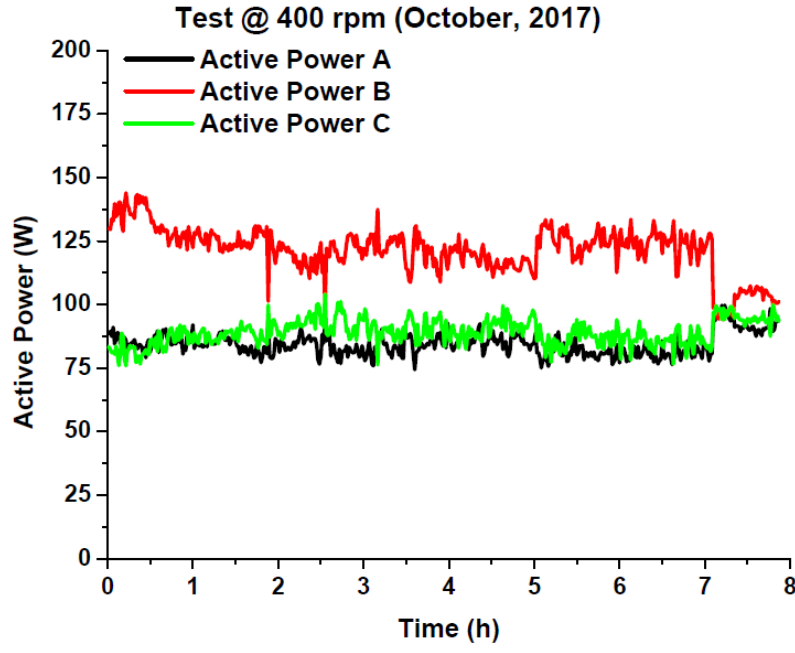


Fig. 2.24 Electric powers provided to the three-phase pump for the second reduced-velocity test (400 rpm).

The measured parameters of the cavitation reactor were the next ones:

- mass of the water solution 22 kg;
- steady-state temperature before the cavitator 26.0°C
- steady-state temperature after the cavitator 26.6°C
- steady-state temperature in the tank 31.0°C;
- pressure drop in the cavitator 4.40 bar;
- electric power provided to the pump 295 W;
- pump rotation velocity 400 rpm;
- steady-state flow rate of the plant 0.0045 m³/minute;

The corresponding energy contributions were evaluated as:

- | | |
|---|------------------------------|
| - Input electric energy absorbed by the pump | $E_{in} = 1062.0 \text{ kJ}$ |
| - Thermal energy stored by water | $E_w = 460.5 \text{ kJ}$ |
| - Thermal energy dispersed in the environment | $E_{disp} = 80.0 \text{ kJ}$ |
| - Mechanical energy dissipated by the cavitator | $E_{mec} = 118.8 \text{ kJ}$ |

Despite the low increase in the velocity of the pump, the efficiency of the system increased in a significant way from the previous case, although reaching still a value significantly lower than one:

$$COP = \frac{E_{out}}{E_{in}} = \frac{659.3 \text{ kJ}}{1062.0 \text{ kJ}} = 0.62 \quad (2.22)$$

The third attempt at reduced velocity was accomplished by driving the pump to 500 rpm, and the thermal outputs of Fig. 2.25 were measured.

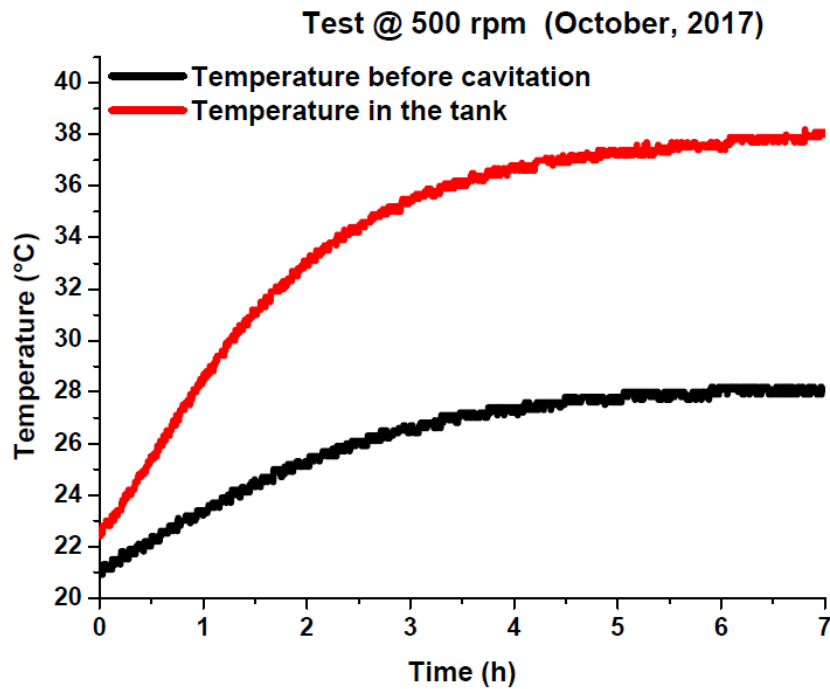


Fig. 2.25 Temperature trends for the third reduced-velocity test (500 rpm).

The steady-state condition was almost reached at the end of the test, for a difference of temperature between the tank and the section before the nozzle of about 10°C. As it is possible to see by comparing the temperatures given by Fig. 2.21, Fig. 2.23 and Fig. 2.25, the increase of the velocity of the pump was found to produce a general increase of the temperature of the fluid, as obvious, but it generated also a progressive increment of the ΔT between the section before the cavitator and the tank. This may suggest that higher velocities will be able to produce cavitation phenomena in a more effective way, and they seem to have an impact on the promotion of piezonuclear reactions in solution.

In Fig. 2.26 the electric powers supplied to the pump are reported.

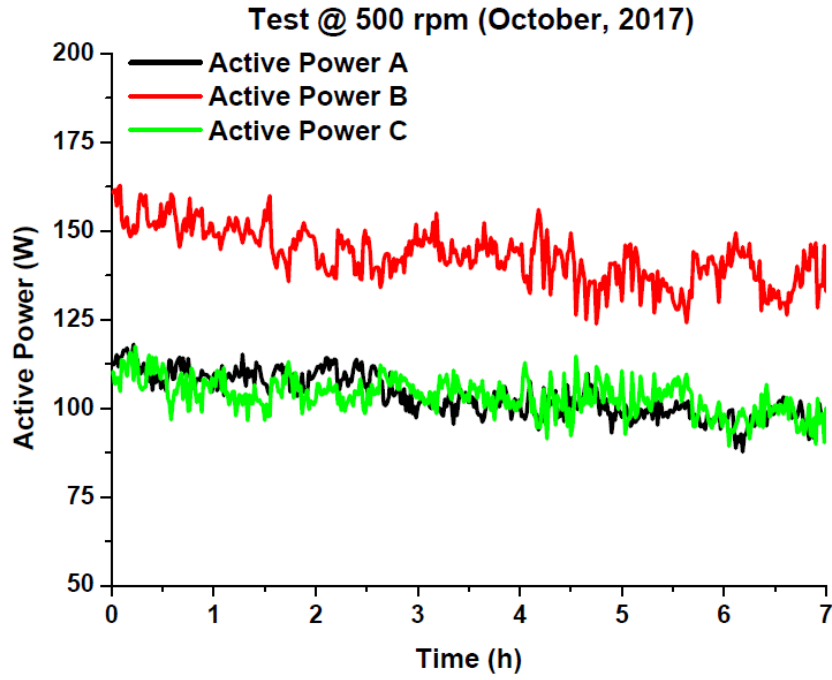


Fig. 2.26 Electric powers provided to the three-phase pump for the third reduced-velocity test (500 rpm).

In order to evaluate the thermal efficiency of the plant, the next physical quantities have been measured:

- mass of the water solution 22 kg;
- steady-state temperature before the cavitator 28.0°C
- steady-state temperature after the cavitator 29.5°C
- steady-state temperature in the tank 38.0°C;
- pressure drop in the cavitator 7.70 bar;
- electric power provided to the pump 350 W;
- pump rotation velocity 500 rpm;
- steady-state flow rate of the plant 0.0055 m³/minute;

Based on these data, the energy contributions have been calculated as follows:

- | | |
|---|-------------------------------|
| - Input electric energy absorbed by the pump | $E_{in} = 1206.0 \text{ kJ}$ |
| - Thermal energy stored by water | $E_w = 920.9 \text{ kJ}$ |
| - Thermal energy dispersed in the environment | $E_{disp} = 105.2 \text{ kJ}$ |
| - Mechanical energy dissipated by the cavitator | $E_{mec} = 254.1 \text{ kJ}$ |

Having evaluated input and output energies, the coefficient of performance was obtained:

$$COP = \frac{E_{out}}{E_{in}} = \frac{1280.2 \text{ kJ}}{1206.0 \text{ kJ}} = 1.06 \quad (2.23)$$

The test at the velocity of 500 rpm allowed for the first time to obtain a COP higher than one, meaning that the sum of output energy contributions due to cavitation was the 6% higher than the input one.

Since the reaching of temperatures of about 60°C - 65°C was considered to be the possible cause of problems of watertightness of the plant, of seal failures and of possible disruptions of the flow-rate sensor, it was decided to avoid the direct testing of pump turning velocities higher than 500 rpm on the insulated plant. Nevertheless, in order to complete the detection of the optimal working velocity of the pump, a preliminary attempt on the non-insulated plant at 700 rpm was considered, whose results are shown in Figs. 2.27-2.28. The direct comparison between the COP evaluated for the reactor in non-insulated and in insulated conditions has been possible because of the theoretical equality of the COP evaluated for the same cavitator and velocity in the two different setups.

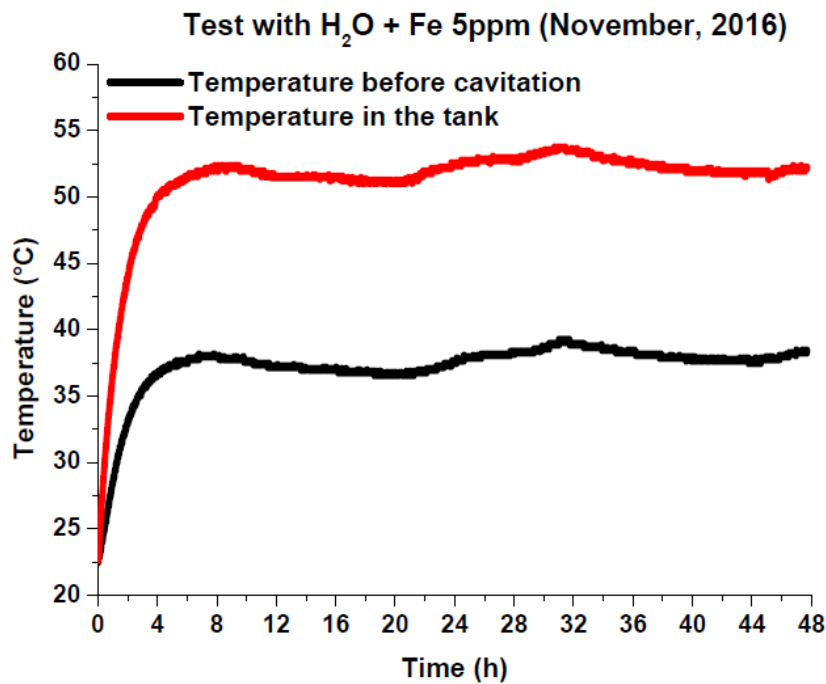


Fig. 2.27 Temperature profiles from test of November 2016.

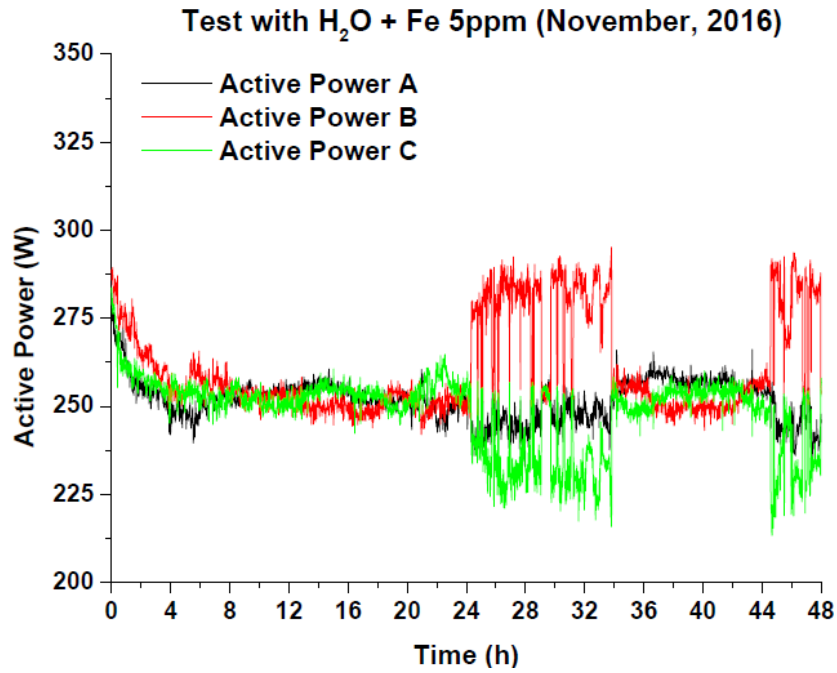


Fig. 2.28 Electric powers provided to the three-phase pump from test of November 2016.

In the analysis, the following physical quantities were considered:

- mass of the water solution 22 kg;
- initial (environmental) temperature 22.4°C;
- steady-state temperature before the cavitator 37.0°C
- steady-state temperature after the cavitator 38.1°C
- steady-state temperature in the tank 52.0°C;
- pressure drop in the cavitator 15.0 bar;
- electric power provided to the pump 750 W;
- pump rotation velocity 700 rpm;
- steady-state flow rate of the plant 0.007 m³/minute;

Starting from the previous data, it was possible to assess the following energy contributions:

- Input electric energy absorbed by the pump $E_{in} = 2713.0$ kJ
- Thermal energy stored by the water $E_w = 1381.4$ kJ
- Thermal energy dispersed in the environment $E_{disp} = 433.6$ kJ
- Mechanical energy dissipated by the cavitator $E_{mec} = 630.0$ kJ

The following Coefficient of Performance was thus evaluated:

$$\text{COP} = \frac{E_{out}}{E_{in}} = \frac{2445.0 \text{ kJ}}{2713.0 \text{ kJ}} = 0.90 \quad (2.24)$$

As it is possible to notice, the COP corresponding to the pump turning velocity of 700 rpm was found to be lower than the value obtained at 500 rpm. On this basis, for the test setting adopted, the velocity of the pump equal to 500 rpm was detected as the optimum one in terms of thermal efficiency. As a consequence of that, although from the theoretical point of view it should be better to drive the cavitation reactor to the highest possible pump velocities and pressures of the fluid, from the practical point of view it is preferable in general adopting reduced pressures and pump velocities, aimed to obtain higher values of efficiency.

Therefore, a series of acoustic measurements were performed on the system by employing piezoelectric transducers PZT at different fluid pressures in order to obtain information about the starting pressures of the cavitation phenomenon in the plant. The starting pressures were detected as the ones which corresponded to some anomalous peak frequencies with respect to the background noise. The acoustic characterisation of the plant revealed as the lower bound for the cavitation inception a pressure of about 4 bar. Despite their practical usefulness for studies of optimisation of the efficiency of the plant for future industrial applications, since they allowed to define a range of pressures to test the system to, the theoretical meaning of these acoustic surveys seems to be not so relevant, and this is the main reason because in the present thesis these tests are just outlined. The maximum perceivable frequencies for the PZT transducers belong in fact to the order of the hundred of kiloHertz, while for the detection of the phonons caused by the implosion of nano-bubbles it would be necessary the achievement of the TeraHertz ones.

2.5 Calorimetric results on the plant equipped by the first generation of brass cavitators according to the indirect method

After a first phase of experimentation that had been carried out by employing a plastic cavitator for the calorimetric tests on the plant, it was decided to produce a set of new brass nozzles with different internal geometries, to test their ability to induce cavitation in the fluid and in particular the production of nanometric bubbles. The geometry of the new cavitators was chosen to have always a final smaller diameter of 2.7 mm. Each cavitator distinguished itself from the others for the different changes of internal diameter and lengths before the reaching of this fixed end value. The changes of diameter were produced by leaving in the internal duct sharp edges, which are the

causes of further turbulence in the flux and then they have a relevant positive effect on the promotion of the cavitation phenomenon, as it was defined in the first theoretical chapter.

Consequently, a set of six new brass cavitators, named M1-M6, was received by the research group of Professor Carpinteri at Politecnico di Torino. In Fig. 2.29 an overall view of the first three cavitators is reported.

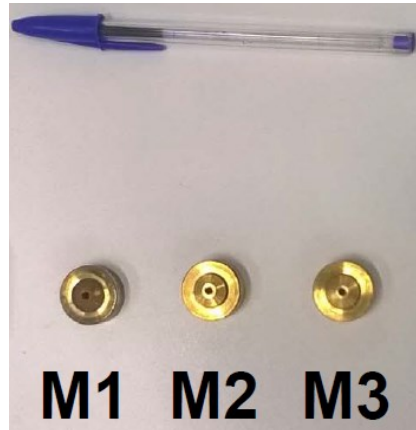


Fig. 2.29 Global front view of the first three brass cavitators.

At the beginning of September 2021, a new phase of the experimental campaign on the study of the energy aspects of the hydrodynamic cavitation started, with the aim to exploit the potentialities of new geometries of cavitators. It was decided in particular to focus on the thermal effects of piezonuclear reactions in the water solution and on the effects of several different shapes of the nozzles on the extra-heat generations. Therefore, it was needed at first to accomplish a new and more complete series of calorimetric tests on the three brass cavitators that had been found to be the best of the first generation during some preliminary attempts. These cavitators were the ones defined as M2, M4 and M5, which were all characterised by a final diameter of 2.7 mm. They were tested at a pump velocity equal to 500 rounds per minute, that had been found as the optimum one during the tests at reduced velocity.

In order to evaluate the thermal balances in the steady-state condition, a new estimation method was developed, defined as “indirect method”. The development of a new assessment method became necessary because of the steady-state condition was considered to be impossible to be reached for the insulated plant (due to the technological limitations of the plastic cavitation reactor, as outlined in Paragraph 2.4). According to the indirect method, the estimation of the energy contributions was done by adopting exactly the same formulations explained for the steady-state condition (Eqs. 2.1-2.20), but in this case interrupting the test in a still transient phase. The main difference from the direct and the indirect evaluation of the COP lies in the fact that in the indirect method the steady-state condition temperatures are extrapolated from the measured interrupted

branches by means of a proper polynomial expression. A polynomial of degree three was chosen for temperature ($T(t)$) as a function of time (t), whose general expression is reported:

$$T(t) = at^3 + bt^2 + ct + d \quad (2.25)$$

Three of the polynomial coefficients were defined by imposing as boundary conditions the passage of the curve for point $(0; T_a)$, the passage for the point $(t_{eq}; T_f)$ and the null value of the tangent in $(t_{eq}; T_f)$, leaving a , T_a , t_{eq} and T_f as free parameters to be assessed by the least squares method (respectively coefficient “ a ”, environmental temperature, time needed for reaching the thermal equilibrium and final, steady-state temperature). By imposing the previous conditions, the following extrapolating equation was obtained:

$$T(t) = at^3 + \left(-2at_{eq} - \frac{T_f - T_a}{t_{eq}^2}\right)t^2 + \left(2\frac{T_f - T_a}{t_{eq}} + at_{eq}^2\right)t + T_a \quad (2.26)$$

The extrapolation procedure allowed to determine the steady-state temperature from the respective interrupted temperature branch (before the cavitator, after the cavitator and in the tank) and to have a comparison between the measured and the analytically extrapolated environmental temperatures. Despite some instability problems of the extrapolation procedure, the indirect method was able to provide a first relevant assessment of the COP without needing to reach directly the steady-state condition, and reducing then the test durations to about 8-10 hours.

The cavitator M5 was the first of the best three brass nozzles of the first generation to be thermally tested. As previously outlined, all the first attempts on the insulated reactor were interrupted at temperatures in the tank always about 50°C, because it was believed that temperatures in the field 60°C-65°C would have been able to cause possible disruptions of parts of the plant. Therefore, the following evaluations of COP were carried out by means of the extrapolation of the indirect method. The Rayleigh and Nusselt numbers and the convective heat transfer coefficient adopted for the thermal dispersion evaluation for cavitator M5 are summarised in Tab. 2.4.

Cavitator M5	
Tests at the velocity of 500 rpm	
Ra (-)	22129.12
Nu (-)	1498.40
h_i $\left(\frac{W}{m^2K}\right)$	77503.47

Tab. 2.4 Rayleigh and Nusselt numbers, internal convection heat transfer coefficient, cavitator M5.

The thermal and electric power monitoring results for the test of the 21st of October 2021 are shown in Figs. 2.30-2.31 respectively.

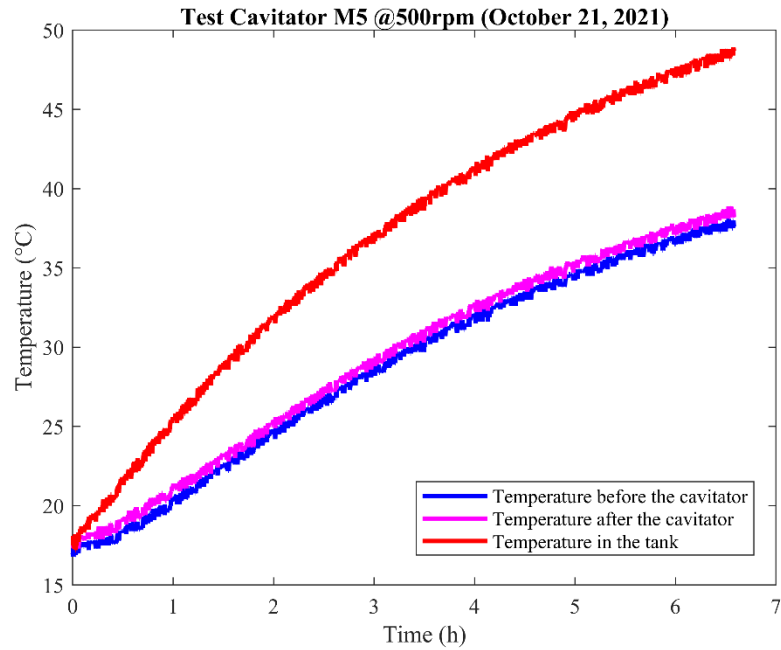


Fig. 2.30 Temperature trends from the test of the 21st of October 2021, cavitator M5, 500rpm.

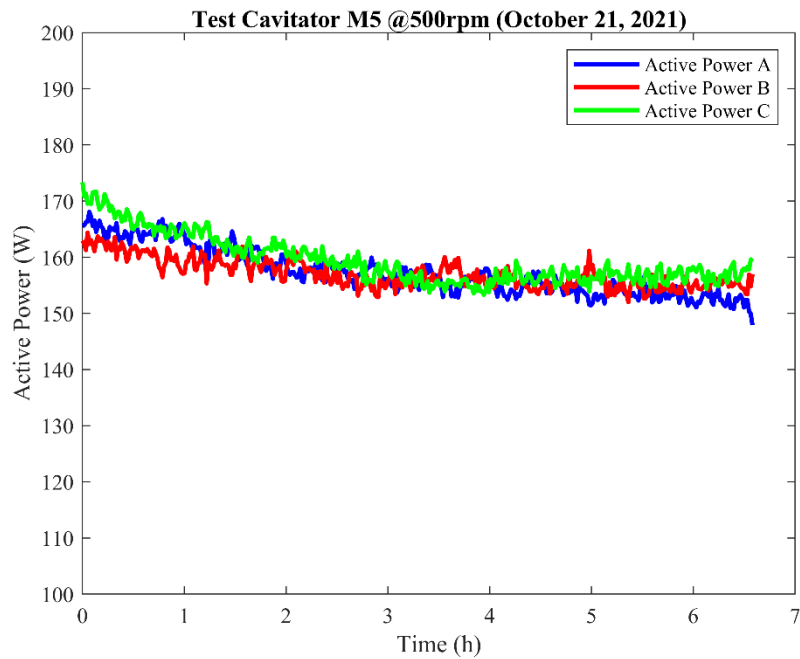


Fig. 2.31 Electric powers provided to the three-phase pump from the test of the 21st of October 2021, cavitator M5, 500rpm.

The energy balance evaluation was accomplished by considering the following data:

- mass of the water solution 25 kg;
- initial (environmental) temperature 17.6°C;
- extrapolated steady-state temperature before the cavitator 38.8°C;

- extrapolated steady-state temperature after the cavitator 38.9°C;
- extrapolated steady-state temperature in the tank 52.1°C;
- pressure drop in the cavitator 10.74 bar;
- electric power provided to the pump 473.69 W;
- pump rotation velocity 500 rpm;
- steady-state flow rate of the plant 0.0121 m³/minute;

Therefore, the next energy terms were calculated by means of the indirect method:

- Input electric energy absorbed by the pump $E_{in} = 1705.3 \text{ kJ}$
- Thermal energy stored by the water $E_w = 1391.8 \text{ kJ}$
- Thermal energy dispersed in the environment $E_{disp} = 259.8 \text{ kJ}$
- Mechanical energy dissipated by the cavitator $E_{mec} = 779.6 \text{ kJ}$

Consequently, the following Coefficient of Performance was evaluated:

$$\text{COP} = \frac{E_{out}}{E_{in}} = \frac{2431.2 \text{ kJ}}{1705.3 \text{ kJ}} = 1.43 \quad (2.27)$$

In Figs. 2.32-2.33 the temperature and the electric power curves of the second insulated test on cavitator M5 are given.

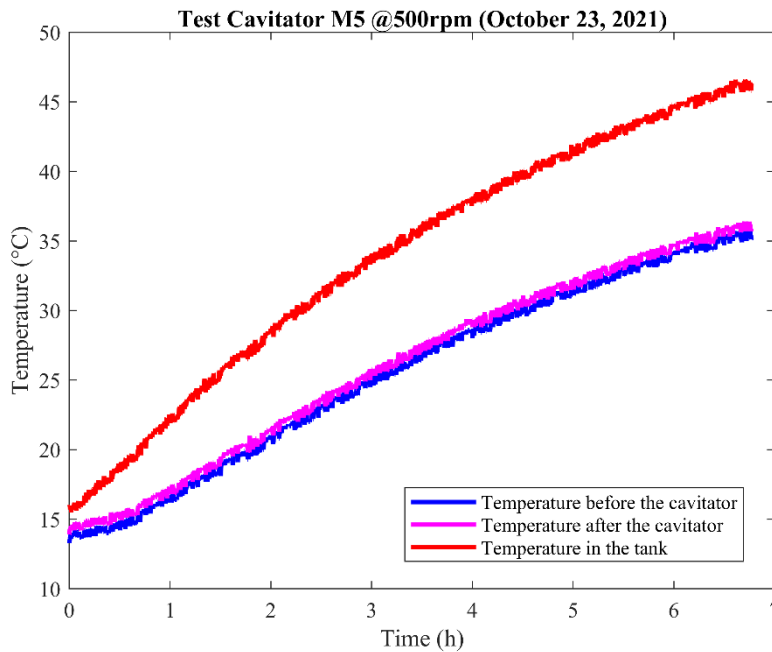


Fig. 2.32 Temperature trends from the test of the 23rd of October 2021, cavitator M5, 500rpm.

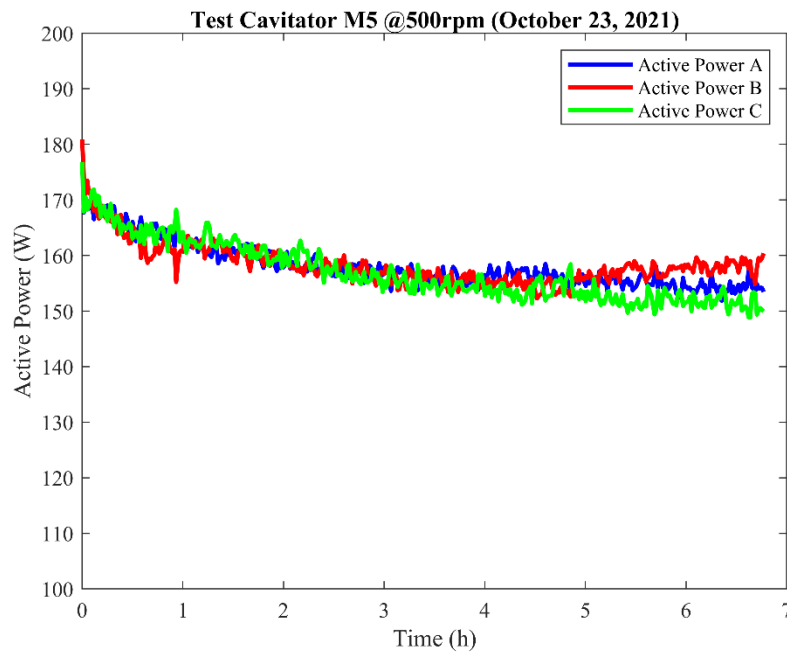


Fig. 2.33 Electric powers provided to the three-phase pump from the test of the 23rd of October 2021, cavitator M5, 500rpm.

The following physical parameters were measured:

- mass of the water solution 25 kg;
- initial (environmental) temperature 15.9°C;
- extrapolated steady-state temperature before the cavitator 36.4°C;
- extrapolated steady-state temperature after the cavitator 37.0°C;
- extrapolated steady-state temperature in the tank 51.5°C;
- pressure drop in the cavitator 10.68 bar;
- electric power provided to the pump 473.44 W;
- pump rotation velocity 500 rpm;
- steady-state flow rate of the plant 0.0121 m³/minute;

The energy contributions to the balance were evaluated as follows:

- Input electric energy absorbed by the pump $E_{in} = 1704.4$ kJ
- Thermal energy stored by the water $E_w = 1580.2$ kJ
- Thermal energy dispersed in the environment $E_{disp} = 262.9$ kJ
- Mechanical energy dissipated by the cavitator $E_{mec} = 775.4$ kJ

The Coefficient of Performance assumed thus the value:

$$\text{COP} = \frac{E_{out}}{E_{in}} = \frac{2618.5 \text{ kJ}}{1704.4 \text{ kJ}} = 1.54 \quad (2.28)$$

The resultant trends of the third calorimetric test on the insulated reactor equipped with cavitator M5 are then portrayed in Figs. 2.34-2.35.

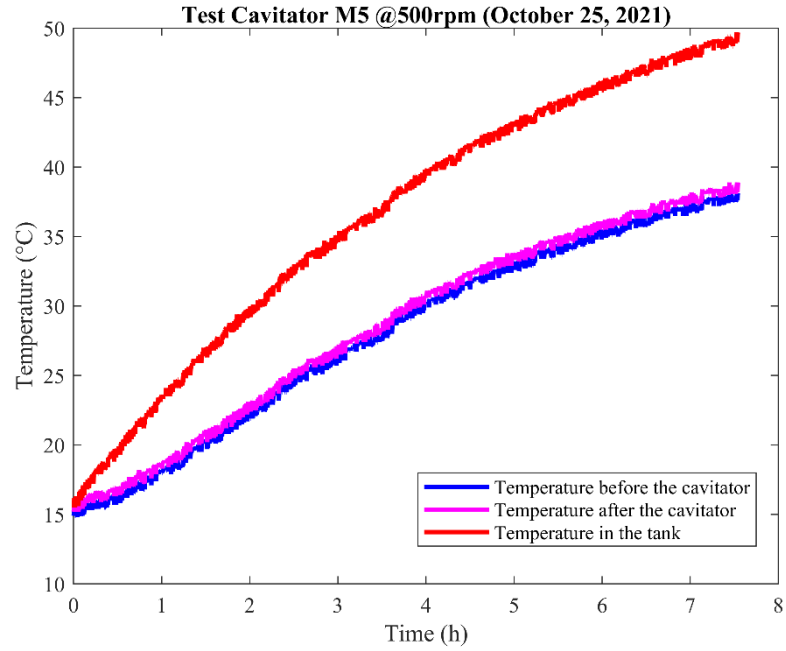


Fig. 2.34 Temperature trends from the test of the 25th of October 2021, cavitator M5, 500rpm.

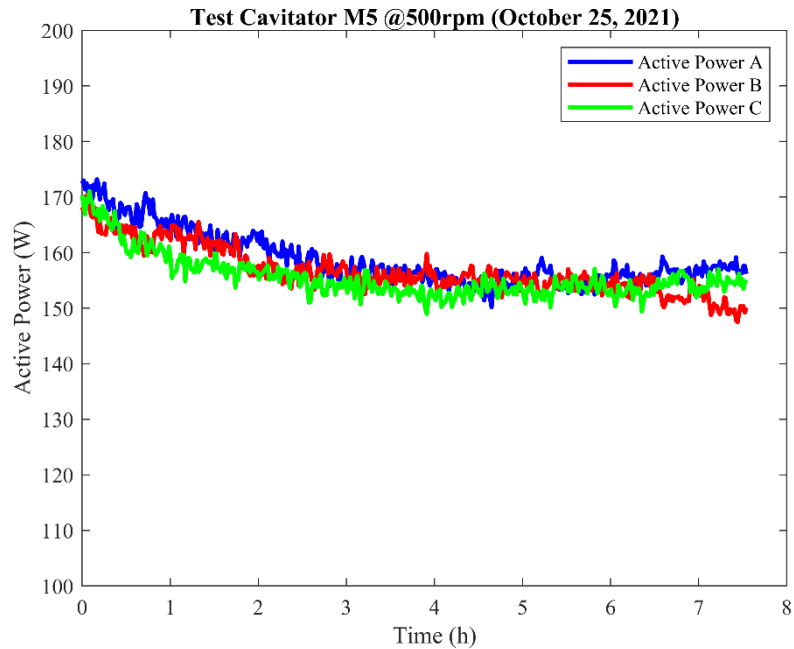


Fig. 2.35 Electric powers provided to the three-phase pump from the test of the 25th of October 2021, cavitator M5, 500rpm.

The next physical quantities were taken into account:

- mass of the water solution 25 kg;
- initial (environmental) temperature 15.7°C;
- extrapolated steady-state temperature before the cavitator 37.8°C;
- extrapolated steady-state temperature after the cavitator 38.3°C;
- extrapolated steady-state temperature in the tank 52.6°C;
- pressure drop in the cavitator 10.48 bar;
- electric power provided to the pump 470.96 W;
- pump rotation velocity 500 rpm;
- steady-state flow rate of the plant 0.0121 m³/minute;

Then, the given terms of the ratio were assessed:

- Input electric energy absorbed by the pump $E_{in} = 1695.5 \text{ kJ}$
- Thermal energy stored by the water $E_w = 1548.8 \text{ kJ}$
- Thermal energy dispersed in the environment $E_{disp} = 275.4 \text{ kJ}$
- Mechanical energy dissipated by the cavitator $E_{mec} = 760.8 \text{ kJ}$

In this last case the Coefficient of Performance was calculated as follows:

$$\text{COP} = \frac{E_{out}}{E_{in}} = \frac{2585.0 \text{ kJ}}{1695.5 \text{ kJ}} = 1.52 \quad (2.29)$$

The repeatability of the insulated tests in terms of measured temperatures can be observed from the superimposition of the three curves of Fig. 2.36, that shows only slight deviations between the trends.

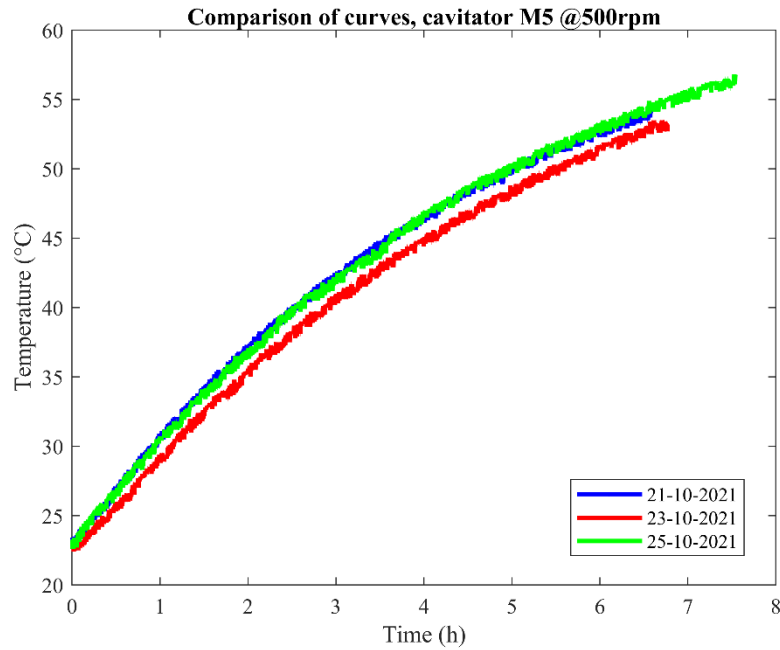


Fig. 2.36 Superimposition of the temperature trends from the insulated tests of cavitator M5 at 500rpm.

Tab. 2.5 reports a summary of the COP which were evaluated according to the extrapolated method for the three tests on cavitator M5, together with the average value and the standard deviation. The relative standard deviation assumes in this case a low value, of only the 4.0%.

Cavitator M5	
Insulated test (indirect method)	COP
21/10/21	1.43
23/10/21	1.54
25/10/21	1.52
Average COP	1.50
St. Dev.	0.06
Rel. St. Dev.	4.0%

Tab. 2.5 Summary of the COP obtained for the cavitator M5, indirect method.

Cavitator M2 has been the second of the three brass nozzles of the first generation to be thermally tested. The internal convection heat transfer coefficient is portrayed in Tab. 2.6.

Cavitator M2	
Tests at the velocity of 500 rpm	
<i>Ra</i> (-)	22631.39

Nu (-)	1532.41
h_i ($\frac{W}{m^2K}$)	79262.59

Tab. 2.6 Rayleigh and Nusselt numbers, internal convection heat transfer coefficient, cavitator M2.

The results in terms of calorimetric performances and electric power absorptions of the first insulated test on the pant equipped by cavitator M2 are shown in Figs. 2.37-2.38.

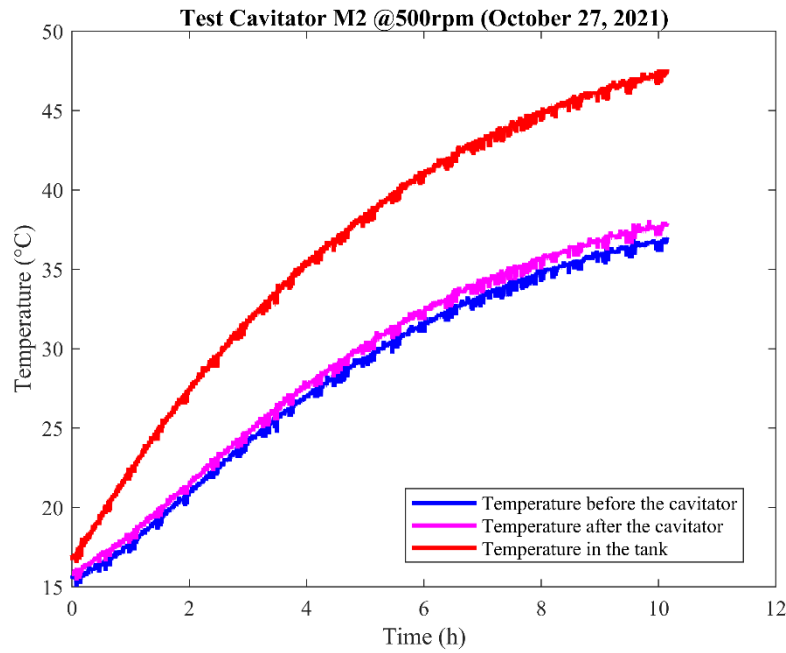


Fig. 2.37 Temperature trends from the test of the 27th of October 2021, cavitator M2, 500rpm.

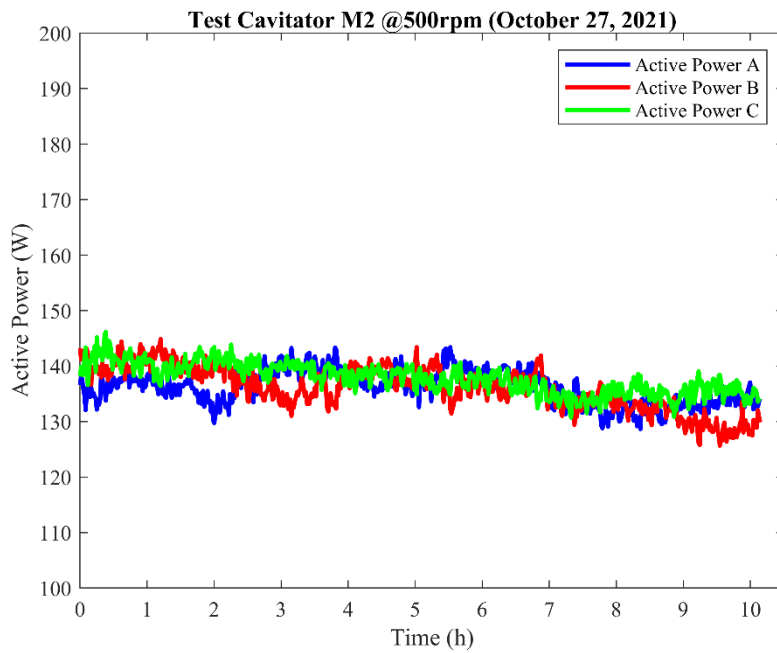


Fig. 2.38 Electric powers provided to the three-phase pump from the test of the 27th of October 2021, cavitator M2, 500rpm.

The ensuing data were collected after the test:

- mass of the water solution 25 kg;
- initial (environmental) temperature 17.0°C;
- extrapolated steady-state temperature before the cavitator 37.1°C;
- extrapolated steady-state temperature after the cavitator 37.9°C;
- extrapolated steady-state temperature in the tank 48.8°C;
- pressure drop in the cavitator 8.04 bar;
- electric power provided to the pump 409.93 W;
- pump rotation velocity 500 rpm;
- steady-state flow rate of the plant 0.01237 m³/minute;

According to the indirect method, the energetic terms were then assessed:

- Input electric energy absorbed by the pump $E_{in} = 1475.8 \text{ kJ}$
- Thermal energy stored by the water $E_w = 1224.4 \text{ kJ}$
- Thermal energy dispersed in the environment $E_{disp} = 241.8 \text{ kJ}$
- Mechanical energy dissipated by the cavitator $E_{mec} = 596.5 \text{ kJ}$

The previous contributions provided the following Coefficient of Performance:

$$\text{COP} = \frac{E_{out}}{E_{in}} = \frac{2062.7 \text{ kJ}}{1475.8 \text{ kJ}} = 1.40 \quad (2.30)$$

The second test on the insulated plant for cavitator M2 allowed to measure the temperature and input electric power curves portrayed in Figs. 2.39-2.40.

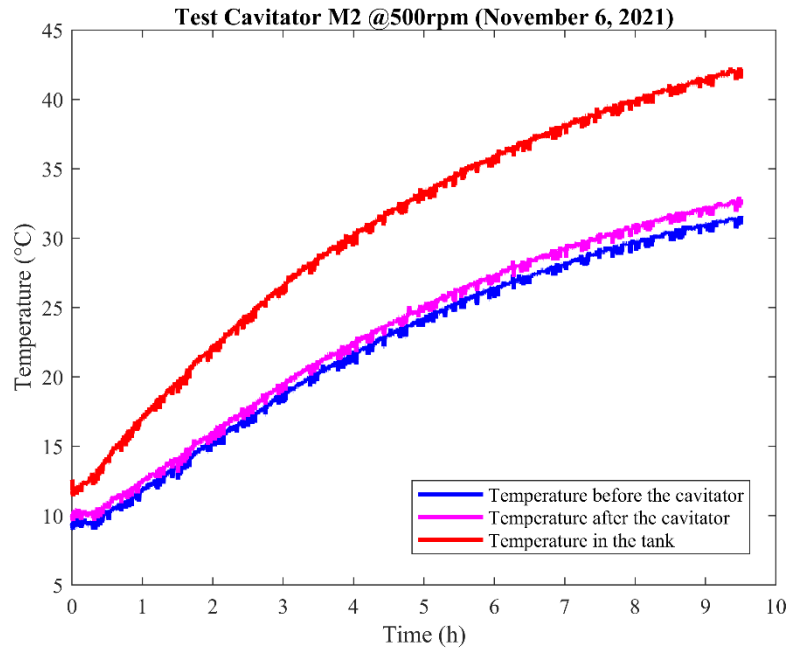


Fig. 2.39 Temperature trends from the test of the 6th of November 2021, cavitator M2, 500rpm.

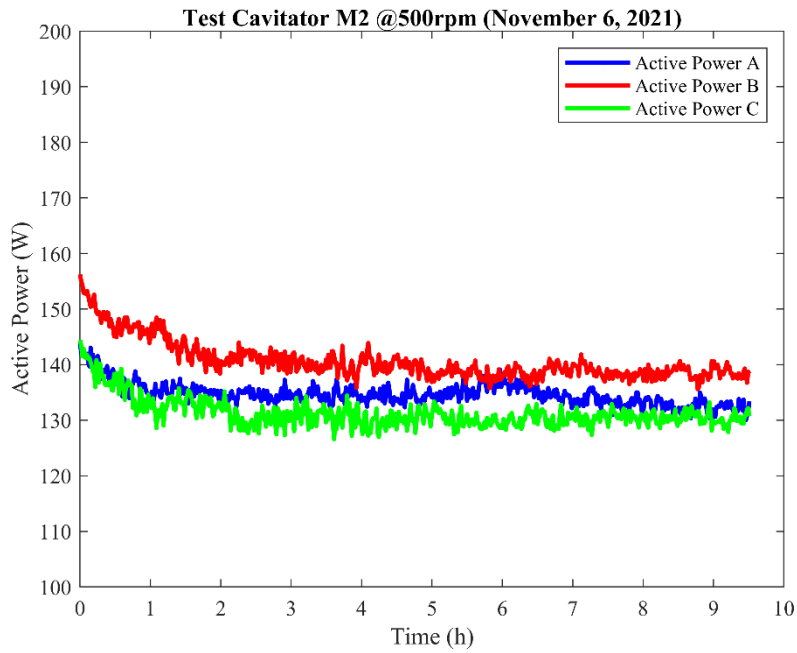


Fig. 2.40 Electric powers provided to the three-phase pump from the test of the 6th of November 2021, cavitator M2, 500rpm.

The next physical parameters were considered in this case:

- mass of the water solution 25 kg;
- initial (environmental) temperature 12.6°C;
- extrapolated steady-state temperature before the cavitator 32.3°C;
- extrapolated steady-state temperature after the cavitator 33.5°C;

- extrapolated steady-state temperature in the tank 44.3°C;
- pressure drop in the cavitator 7.94 bar;
- electric power provided to the pump 406.51 W;
- pump rotation velocity 500 rpm;
- steady-state flow rate of the plant 0.01237 m³/minute;

Therefore, the following energy terms were evaluated:

- Input electric energy absorbed by the pump $E_{in} = 1463.4 \text{ kJ}$
- Thermal energy stored by the water $E_w = 1255.8 \text{ kJ}$
- Thermal energy dispersed in the environment $E_{disp} = 239.5 \text{ kJ}$
- Mechanical energy dissipated by the cavitator $E_{mec} = 589.2 \text{ kJ}$

The Coefficient of Performance was thus estimated:

$$\text{COP} = \frac{E_{out}}{E_{in}} = \frac{2084.5 \text{ kJ}}{1463.4 \text{ kJ}} = 1.42 \quad (2.31)$$

The third and last insulated calorimetric attempt on cavitator M2 produced the thermal and electric power trends of Figs. 2.41-2.42.

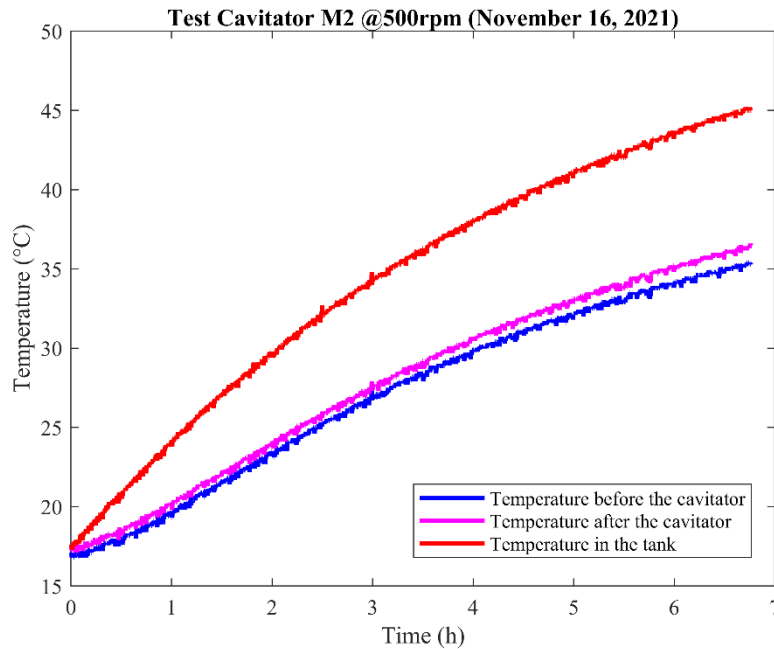


Fig. 2.41 Temperature trends from the test of the 16th of November 2021, cavitator M2, 500rpm.

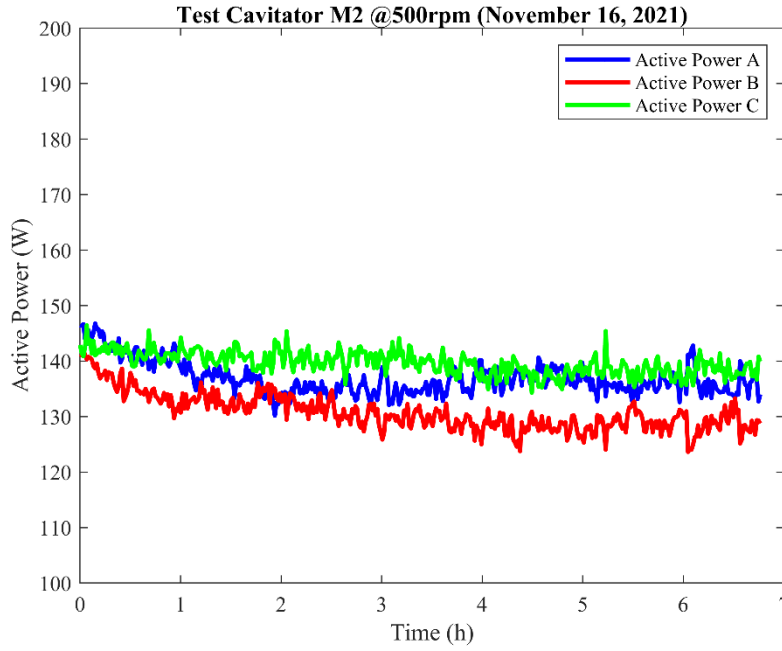


Fig. 2.42 Electric powers provided to the three-phase pump from the test of the 16th of November 2021, cavitor M2, 500rpm.

The physical parameters measured after the test are shown:

- mass of the water solution 25 kg;
- initial (environmental) temperature 17.6°C;
- extrapolated steady-state temperature before the cavitor 36.3°C;
- extrapolated steady-state temperature after the cavitor 37.3°C;
- extrapolated steady-state temperature in the tank 48.0°C;
- pressure drop in the cavitor 8.33 bar;
- electric power provided to the pump 407.26 W;
- pump rotation velocity 500 rpm;
- steady-state flow rate of the plant 0.01237 m³/minute;

The next energy contributions were evaluated from the previous data:

- Input electric energy absorbed by the pump $E_{in} = 1466.2$ kJ
- Thermal energy stored by the water $E_w = 1224.4$ kJ
- Thermal energy dispersed in the environment $E_{disp} = 229.3$ kJ
- Mechanical energy dissipated by the cavitor $E_{mec} = 618.7$ kJ

Consequently, the following Coefficient of Performance was calculated:

$$\text{COP} = \frac{E_{out}}{E_{in}} = \frac{2072.4 \text{ kJ}}{1466.2 \text{ kJ}} = 1.41 \quad (2.32)$$

With the aim to compare the calorimetric results obtained during the three tests on the insulated reactor for cavitator M2, the superimposition of the curves shown in Fig. 2.43 was produced. The graph portrays quite low deviations between curves, with a major variance just for the test of the 16th of November 2021.

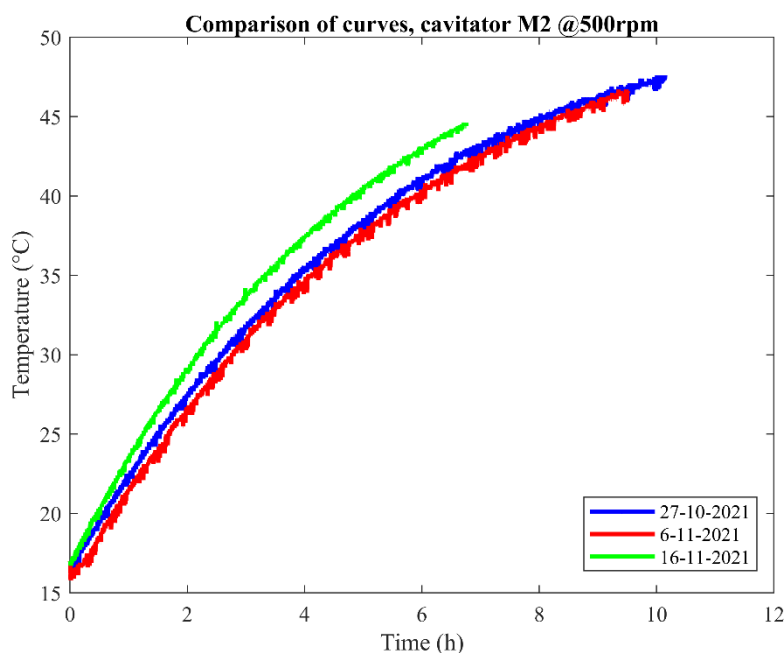


Fig. 2.43 Superimposition of the temperature trends from the insulated tests of cavitator M2 at 500rpm.

By means of the global analysis of the results obtained from cavitator M2 according to the indirect method (Tab. 2.7), it is worth noting that the mean value of the COP evaluated through this cavitator is about the 6% lower than the average one of cavitator M5.

Cavitator M2	
Insulated test (indirect method)	COP
27/10/21	1.40
06/11/21	1.42
16/11/21	1.41
Average COP	1.41
St. Dev.	0.01
Rel. St. Dev.	0.7%

Tab. 2.7 Summary of the COP obtained with the cavitator M2, indirect method

Cavitator M4 was tested from the calorimetric perspective as the last of the best brass cavitators of the first generation. In Tab. 2.8 the Rayleigh and Nusselt numbers and the internal convection heat transfer coefficient are reported.

Cavitator M4	
Tests at the velocity of 500 rpm	
Ra (-)	21812.79
Nu (-)	1476.98
h_i ($\frac{W}{m^2K}$)	76395.56

Tab. 2.8 Rayleigh and Nusselt numbers, internal convection heat transfer coefficient, cavitator M4.

The temperature trends and electrical power absorptions of the first insulated test are shown in Figs. 2.44-2.45, as in the previous cases for a velocity of the pump of 500 rpm.

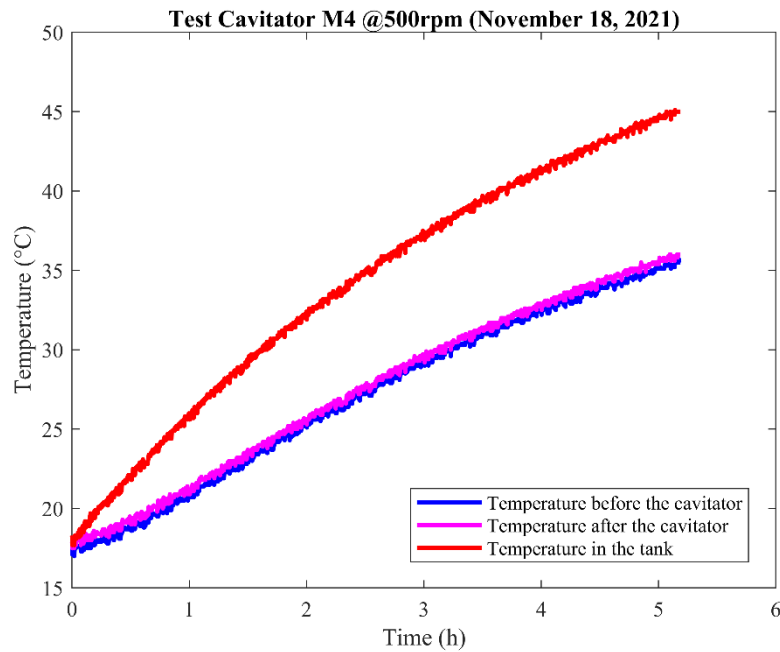


Fig. 2.44 Temperature trends from the test of the 18th of November 2021, cavitator M4, 500rpm.

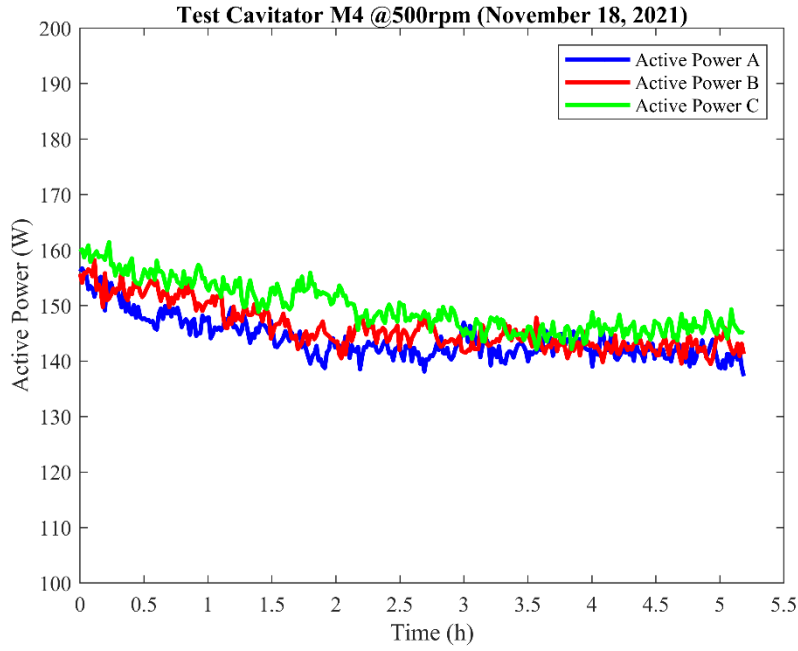


Fig. 2.45 Electric powers provided to the three-phase pump from the test of the 18th of November 2021, cavitor M4, 500rpm.

In order to perform the energetic balance, the ensuing data were considered:

- mass of the water solution 25 kg;
- initial (environmental) temperature 18.3°C;
- extrapolated steady-state temperature before the cavitor 36.7°C;
- extrapolated steady-state temperature after the cavitor 36.9°C;
- extrapolated steady-state temperature in the tank 50.0°C;
- pressure drop in the cavitor 9.77 bar;
- electric power provided to the pump 439.48 W;
- pump rotation velocity 500 rpm;
- steady-state flow rate of the plant 0.01192 m³/minute;

The next energetic contributions were evaluated:

- Input electric energy absorbed by the pump $E_{in} = 1582.1$ kJ
- Thermal energy stored by the water $E_w = 1391.8$ kJ
- Thermal energy dispersed in the environment $E_{disp} = 234.6$ kJ
- Mechanical energy dissipated by the cavitor $E_{mec} = 698.6$ kJ

The following Coefficient of Performance was thus estimated:

$$\text{COP} = \frac{E_{out}}{E_{in}} = \frac{2325.0 \text{ kJ}}{1582.1 \text{ kJ}} = 1.47 \quad (2.33)$$

The temperature curves and electric power supply trends for the three-phase pump collected during the second test on the insulated plant are shown in Figs. 2.46-2.47.

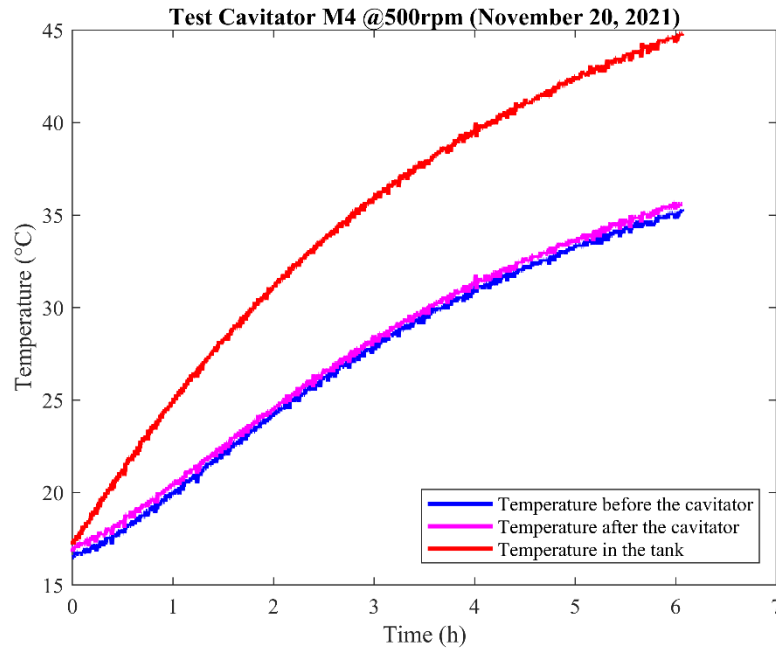


Fig. 2.46 Temperature trends from the test of the 20th of November 2021, cavitator M4, 500rpm.

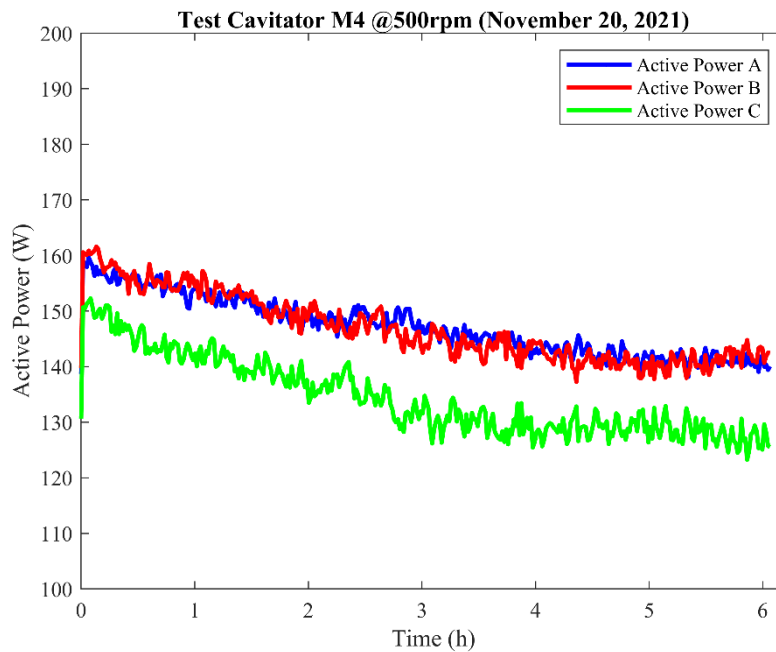


Fig. 2.47 Electric powers provided to the three-phase pump from the test of the 20th of November 2021, cavitator M4, 500rpm.

The following physical parameters were measured:

- mass of the water solution 25 kg;

- initial (environmental) temperature 17.4°C;
- extrapolated steady-state temperature before the cavitator 35.8°C;
- extrapolated steady-state temperature after the cavitator 36.2°C;
- extrapolated steady-state temperature in the tank 46.8°C;
- pressure drop in the cavitator 9.40 bar;
- electric power provided to the pump 428.47 W;
- pump rotation velocity 500 rpm;
- steady-state flow rate of the plant 0.01192 m³/minute;

The energy input and output terms were calculated as in the next list:

- Input electric energy absorbed by the pump $E_{in} = 1542.5 \text{ kJ}$
- Thermal energy stored by the water $E_w = 1151.2 \text{ kJ}$
- Thermal energy dispersed in the environment $E_{disp} = 222.5 \text{ kJ}$
- Mechanical energy dissipated by the cavitator $E_{mec} = 672.5 \text{ kJ}$

Therefore, the Coefficient of Performance was assessed as follows:

$$\text{COP} = \frac{E_{out}}{E_{in}} = \frac{2046.2 \text{ kJ}}{1542.5 \text{ kJ}} = 1.33 \quad (2.34)$$

Passing then to the last test on the insulated plant performed for cavitator M4, the calorimetric and input electric power diagrams are given in Figs. 2.48-2.49.

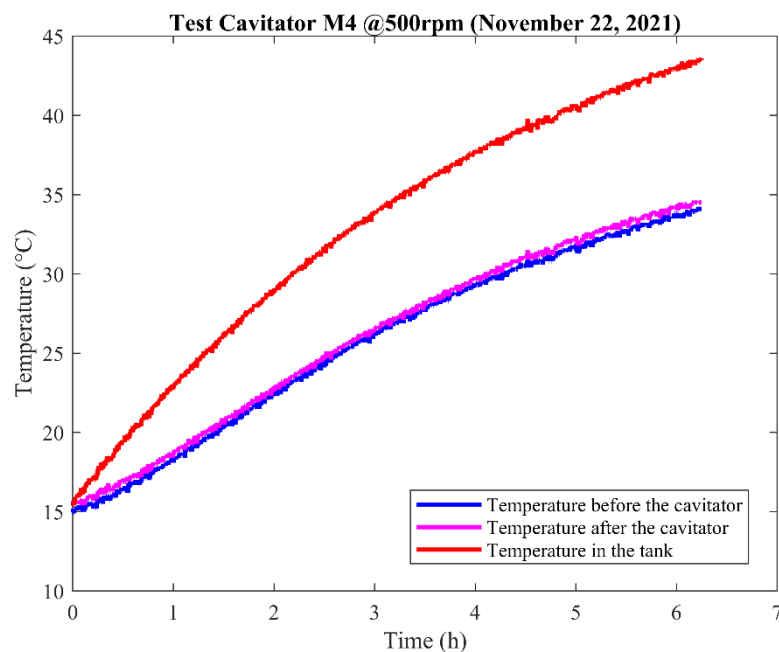


Fig. 2.48 Temperature trends from the test of the 22nd of November 2021, cavitator M4, 500rpm.

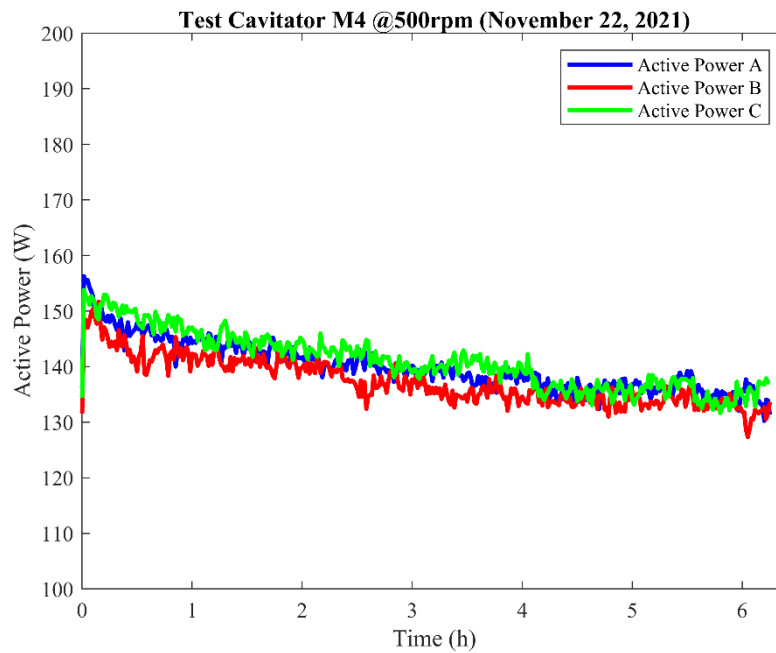


Fig. 2.49 Electric powers provided to the three-phase pump from the test of the 22nd of November 2021, cavitator M4, 500rpm.

The next values of the measured parameters were adopted in the calculations:

- mass of the water solution 25 kg;
- initial (environmental) temperature 15.5°C;
- extrapolated steady-state temperature before the cavitator 34.7°C;
- extrapolated steady-state temperature after the cavitator 35.1°C;
- extrapolated steady-state temperature in the tank 45.9°C;
- pressure drop in the cavitator 8.96 bar;
- electric power provided to the pump 418.26 W;
- pump rotation velocity 500 rpm;
- steady-state flow rate of the plant 0.01192 m³/minute;

The following energy contributions were evaluated:

- Input electric energy absorbed by the pump $E_{in} = 1505.7$ kJ
- Thermal energy stored by the water $E_w = 1172.1$ kJ
- Thermal energy dispersed in the environment $E_{disp} = 230.6$ kJ
- Mechanical energy dissipated by the cavitator $E_{mec} = 641.3$ kJ

In this case the COP assumed the next value:

$$\text{COP} = \frac{E_{out}}{E_{in}} = \frac{2044.0 \text{ kJ}}{1505.7 \text{ kJ}} = 1.36 \quad (2.35)$$

The superimposition of the temperature curves registered by the thermocouple in the tank for the insulated reactor (Fig. 2.50) highlights the repeatability of the calorimetric results obtained, since low variations between the calorimetric outputs of the different tests were revealed.

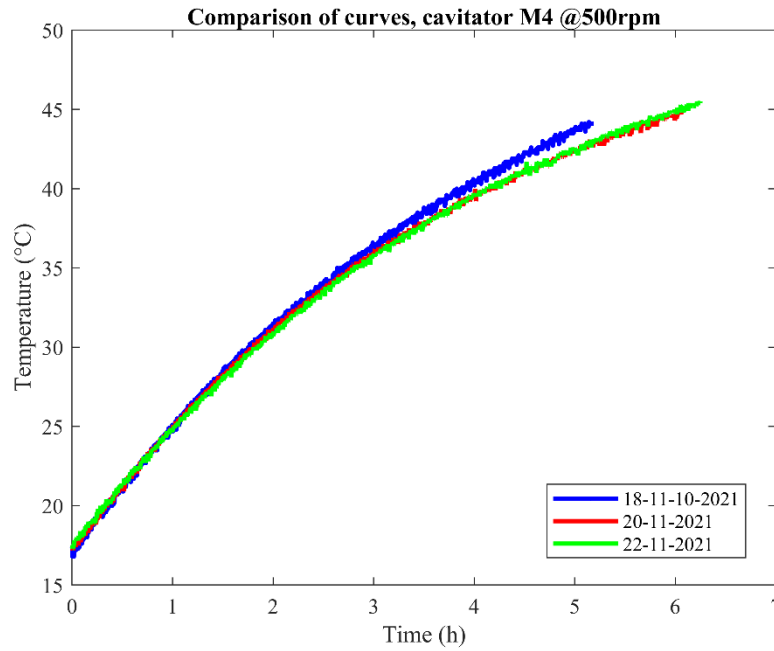


Fig. 2.50 Superimposition of the temperature trends from the insulated tests of cavitator M4 at 500rpm.

In Tab. 2.9 a summary of the Coefficients Of Performance evaluated from the tests on cavitator M4 by means of the extrapolated method is produced.

Cavitator M4	
Insulated test (indirect method)	COP
18/11/21	1.47
20/11/21	1.33
22/11/21	1.36
Average COP	1.39
St. Dev.	0.07
Rel. St. Dev.	5.0%

Tab. 2.9 Summary of the COP obtained with the cavitator M4, indirect method.

As it is possible to notice, the average value of the COP assessed for cavitator M4 was slightly lower than the the average COP estimated for cavitators M2 and M5. The calorimetric tests on the first generation of brass cavitators analysed by means of the indirect method allowed for the first time to quantify an exceedance of at least the 30% (and up to the 50%) for the energy produced by cavitation with respect to the input electric absorption.

2.6 Calorimetric results on the plant equipped by the second generation of brass cavitators according to the indirect method

Once the first calorimetric experimentation phase on the cavitators M5, M2 and M4 had ended, the attention and the laboratory activity were focused on a new set of three brass cavitators, that are collectively called in the present paper the “second generation” of nozzles. The production of the new cavitators was decided with the aim of exploring the potentialities in terms of heat generations and thermal efficiencies of reducing final diameters of the nozzles. In the design phase, a reducing factor equal to $\frac{1}{2}$ was chosen for the final diameter of the throat section, passing then from a diameter of 2.7 mm for the cavitator defined as “NB” (equal to the final diameters of the first generation of cavitators), to 1.4 mm for the cavitator defined as “NM” and finally to 0.7 mm for the cavitator called “NS”. Although cavitator NB was designed to have the same terminal diameter of the previous cavitators, its inner section was defined for the purpose to be a more performing one by means of different changes of diameter with sharp edges, that contribute to foster turbulence, and then cavitation, as stated in Chapter 1.

In the preliminary phase of the calorimetric tests on the new cavitator NB, it was decided to accomplish a series of three attempts at different pump velocities on the non-insulated cavitation reactor, with the aim of obtaining an estimate of the optimal working velocity of the plant. Since for the non-insulated tests it was possible to reach the steady-state condition without overpassing the temperatures which were considered at first as a technological limit for the plant (60°C -65°C), the energy contributions to the balance were evaluated directly with reference to the steady-state values of the parameters, avoiding thus the extrapolation procedure.

Tab. 2.10 reports the internal convection heat transfer coefficients and the Rayleigh and Nusselt numbers for the pump turning velocities tested in this first phase on cavitator NB.

Cavitator NB	
Test at the velocity of 350 rpm	
<i>Ra</i> (-)	15818.90
<i>Nu</i> (-)	1071.12

$h_i \left(\frac{W}{m^2K} \right)$	55403.01
Tests at the velocity of 500 rpm	
$Ra (-)$	22117.05
$Nu (-)$	1497.58
$h_i \left(\frac{W}{m^2K} \right)$	77461.18
Test at the velocity of 650 rpm	
$Ra (-)$	25106.97
$Nu (-)$	1700.04
$h_i \left(\frac{W}{m^2K} \right)$	87932.86

Tab. 2.10 Rayleigh and Nusselt numbers, internal convection heat transfer coefficient, cavitator NB.

The results obtained by the test at 350 rounds per minute of the three-phase pump for the non-insulated reactor are shown in Figs. 2.51-2.52, in terms of temperature trends and electric power absorptions, respectively.

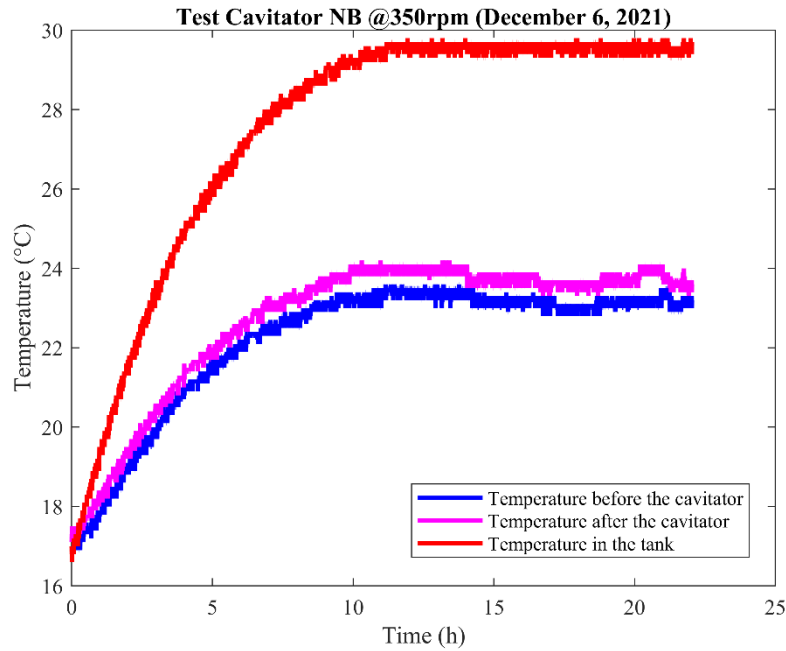


Fig. 2.51 Temperature trends from the test of the 6th of December 2021, cavitator NB, 350rpm.

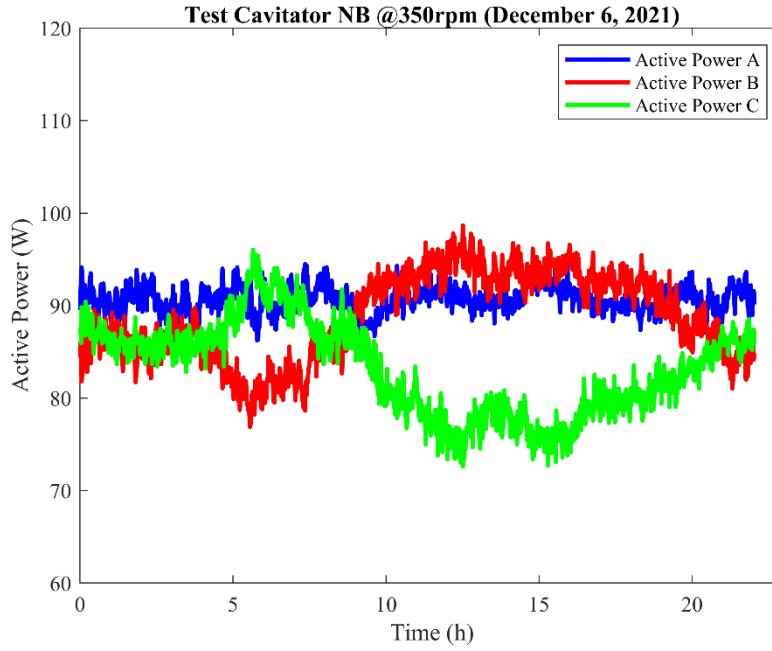


Fig. 2.52 Electric powers provided to the three-phase pump from the test of the 6th of December 2021, cavitator NB, 350rpm.

The following physical parameters were considered:

- mass of the water solution 25 kg;
- initial (environmental) temperature 17.0°C;
- steady-state temperature before the cavitator 23.2°C;
- steady-state temperature after the cavitator 23.8°C;
- steady-state temperature in the tank 29.6°C;
- pressure drop in the cavitator 5.36 bar;
- electric power provided to the pump 262.67 W;
- pump rotation velocity 350 rpm;
- steady-state flow rate of the plant 0.00865 m³/minute;

According to Eqs. 2.1-2.20, the next energy contributions were assessed:

- Input electric energy absorbed by the pump $E_{in} = 945.6$ kJ
- Thermal energy stored by the water $E_w = 669.8$ kJ
- Thermal energy dispersed in the environment $E_{disp} = 184.4$ kJ
- Mechanical energy dissipated by the cavitator $E_{mec} = 278.1$ kJ

The Coefficient of Performance was then evaluated as:

$$\text{COP} = \frac{E_{out}}{E_{in}} = \frac{1132.3 \text{ kJ}}{945.6 \text{ kJ}} = 1.20 \quad (2.36)$$

The second test on the non-insulated reactor equipped by the cavitator NB was carried out by imposing to the three-phase pump a rotation velocity of 500rpm, equal to the optimal one of the first generation of cavitators. The temperature trends and electrical power supplies are portrayed in Figs. 2.53-2.54.

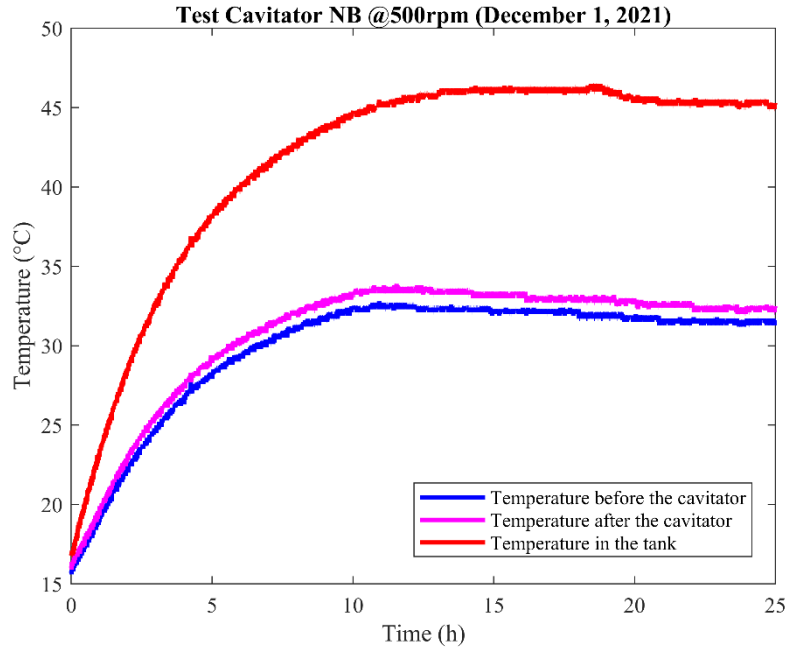


Fig. 2.53 Temperature trends from the test of the 1st of December 2021, cavitator NB, 500rpm.

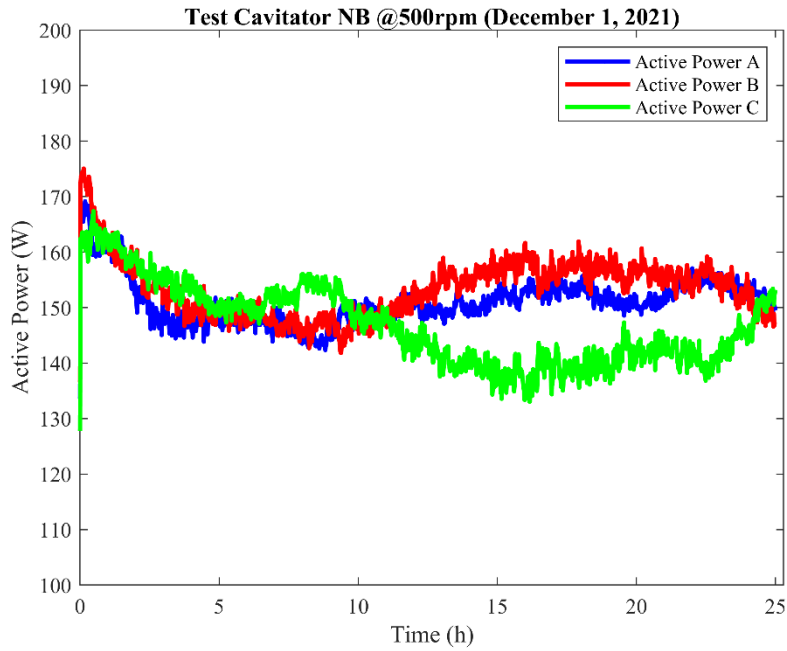


Fig. 2.54 Electric powers provided to the three-phase pump from the test of the 1st of December 2021, cavitator NB, 500rpm.

After the attempt, the next physical quantities were measured:

- mass of the water solution 25 kg;
- initial (environmental) temperature 16.9°C;
- steady-state temperature before the cavitator 31.8°C;
- steady-state temperature after the cavitator 32.7°C;
- steady-state temperature in the tank 45.7°C;
- pressure drop in the cavitator 10.47 bar;
- electric power provided to the pump 451.39 W;
- pump rotation velocity 500 rpm;
- steady-state flow rate of the plant 0.01209 m³/minute;

The energy terms were evaluated as follows:

- Input electric energy absorbed by the pump $E_{in} = 1625.0$ kJ
- Thermal energy stored by the water $E_w = 1454.6$ kJ
- Thermal energy dispersed in the environment $E_{disp} = 425.7$ kJ
- Mechanical energy dissipated by the cavitator $E_{mec} = 759.6$ kJ

The following Coefficient of Performance was calculated:

$$COP = \frac{E_{out}}{E_{in}} = \frac{2639.9 \text{ kJ}}{1625.0 \text{ kJ}} = 1.62 \quad (2.37)$$

It is worth noting that the value obtained for cavitator NB at 500 rpm was the first one which overpassed the value of one point six for the reactor. This observation highlighted the better performances of the new cavitator with respect to the efficiencies of the previous ones in the same testing conditions.

The third attempt on cavitator NB in non-insulated plant setup was accomplished by setting the turns of the pump to the higher value of 650rpm. The calorimetric and electrical power monitoring results are shown in Figs. 2.55-2.56.

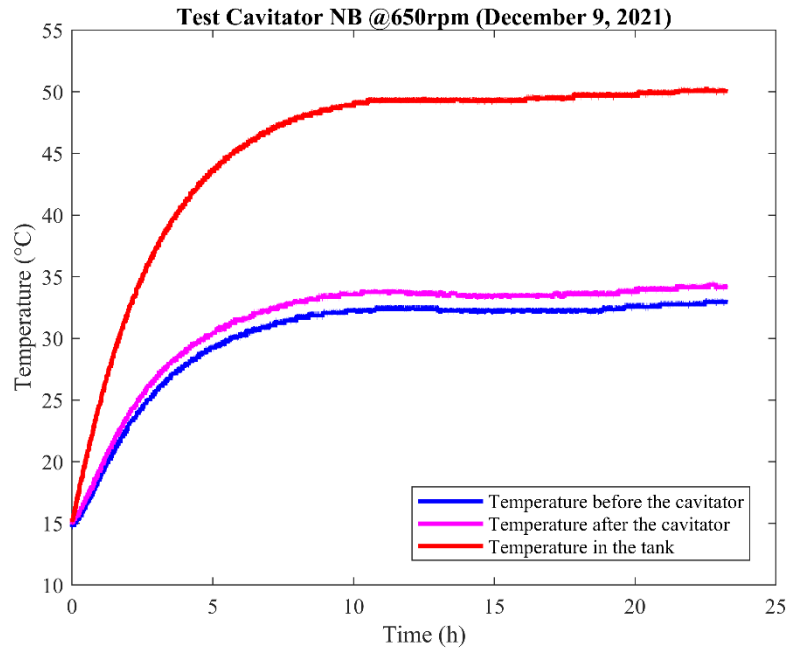


Fig. 2.55 Temperature trends from the test of the 9th of December 2021, cavitator NB, 650rpm.

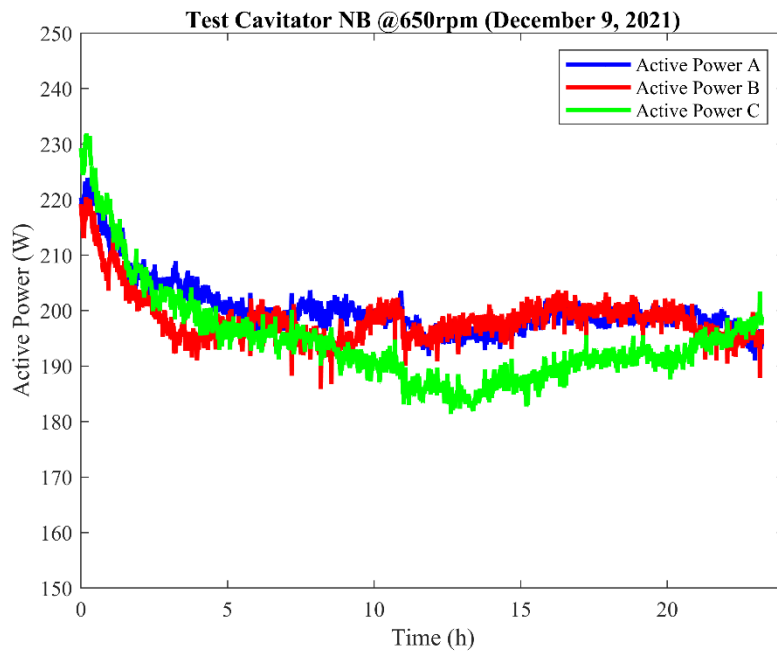


Fig. 2.56 Electric powers provided to the three-phase pump from the test of the 9th of December 2021, cavitator NB, 650rpm.

The next physical parameters of the attempt were taken into account:

- mass of the water solution 25 kg;
- initial (environmental) temperature 15.4°C;
- steady-state temperature before the cavitator 32.5°C;
- steady-state temperature after the cavitator 33.8°C;
- steady-state temperature in the tank 49.7°C;

- pressure drop in the cavitator 11.71 bar;
- electric power provided to the pump 593.50 W;
- pump rotation velocity 650 rpm;
- steady-state flow rate of the plant 0.01372 m³/minute;

The energy contributions were then calculated:

- Input electric energy absorbed by the pump $E_{in} = 2136.6$ kJ
- Thermal energy stored by the water $E_w = 1800.0$ kJ
- Thermal energy dispersed in the environment $E_{disp} = 503.1$ kJ
- Mechanical energy dissipated by the cavitator $E_{mec} = 964.4$ kJ

The Coefficient of Performance was evaluated as shown:

$$COP = \frac{E_{out}}{E_{in}} = \frac{3267.5 \text{ kJ}}{2136.6 \text{ kJ}} = 1.53 \quad (2.38)$$

As it is possible to notice, in the last attempt the further increase of the pump rotation velocity caused a sensible decrease of the efficiency of the reactor in the steady-state condition. It was a clear signal of the overpassing of the optimal working condition, that was then found by the parabolic interpolation of Fig. 2.57 to correspond to a velocity of about 549 rpm.

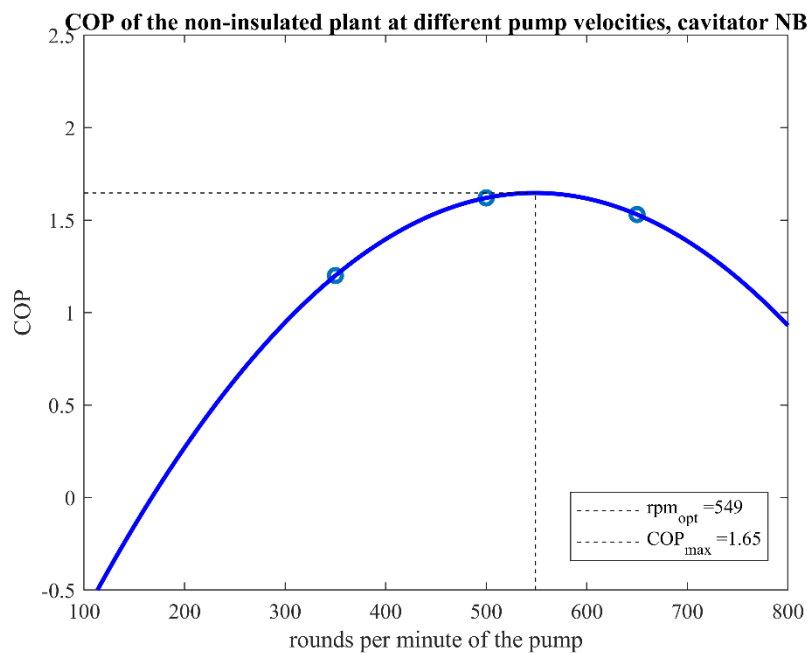


Fig. 2.57 Parabolic interpolation on the values of COP evaluated for different pump velocities, cavitator NB.

Since the optimum working condition was identified to be close to the velocity of 500rpm and to be related to a COP almost equal to the one of Eq. (2.33), it was decided to perform the calorimetric tests on cavitator NB at 500 rpm, the same rotation velocity chosen also for the cavitators M5, M2 and M4.

In order to have a direct comparison of the results between the insulated-plant tests accomplished on the first and on the second generation of brass cavitators, it was decided in a first phase of the experimental campaign to continue to refer to the indirect method for the assessment of the COP in the steady-state condition. For the assessment of the steady-state temperatures by extrapolation from the existing branch, the same expression considered for the previous cavitators was adopted (Eq. 2.26).

The first of the four attempts on the insulated cavitation reactor for cavitator NB allowed to register the curves of temperatures and electric power supplies shown in Figs. 2.58-2.59.

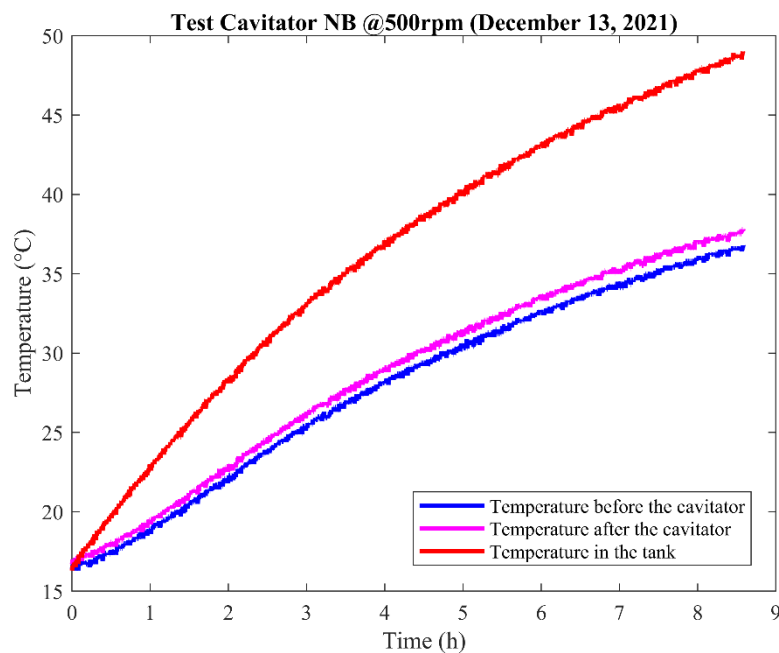


Fig. 2.58 Temperature trends from the test of the 13th of December 2021, cavitator NB, 500rpm.

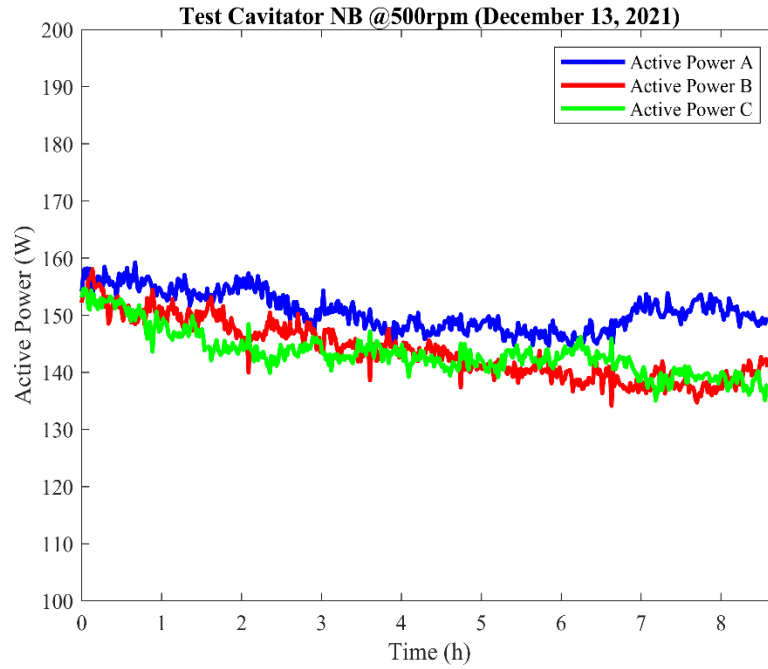


Fig. 2.59 Electric powers provided to the three-phase pump from the test of the 13th of December 2021, cavitor NB, 500rpm.

During the test, the next physical parameters were noted:

- mass of the water solution 25 kg;
- initial (environmental) temperature 16.3°C;
- extrapolated steady-state temperature before the cavitor 39.6°C;
- extrapolated steady-state temperature after the cavitor 40.8°C;
- extrapolated steady-state temperature in the tank 52.5°C;
- pressure drop in the cavitor 9.93 bar;
- electric power provided to the pump 437.81 W;
- pump rotation velocity 500 rpm;
- steady-state flow rate of the plant 0.01209 m³/minute;

The following energy input and output terms were calculated:

- Input electric energy absorbed by the pump $E_{in} = 1576.1$ kJ
- Thermal energy stored by the water $E_w = 1350.0$ kJ
- Thermal energy dispersed in the environment $E_{disp} = 276.9$ kJ
- Mechanical energy dissipated by the cavitor $E_{mec} = 720.5$ kJ

From the previous energy contributions, the Coefficient of Performance was assessed as follows:

$$\text{COP} = \frac{E_{out}}{E_{in}} = \frac{2347.4 \text{ kJ}}{1576.1 \text{ kJ}} = 1.49 \quad (2.39)$$

The results in terms of temperature curves and electric power supplies of the second test on the insulated plant equipped by the cavitator NB are portrayed in Figs. 2.60-2.61.

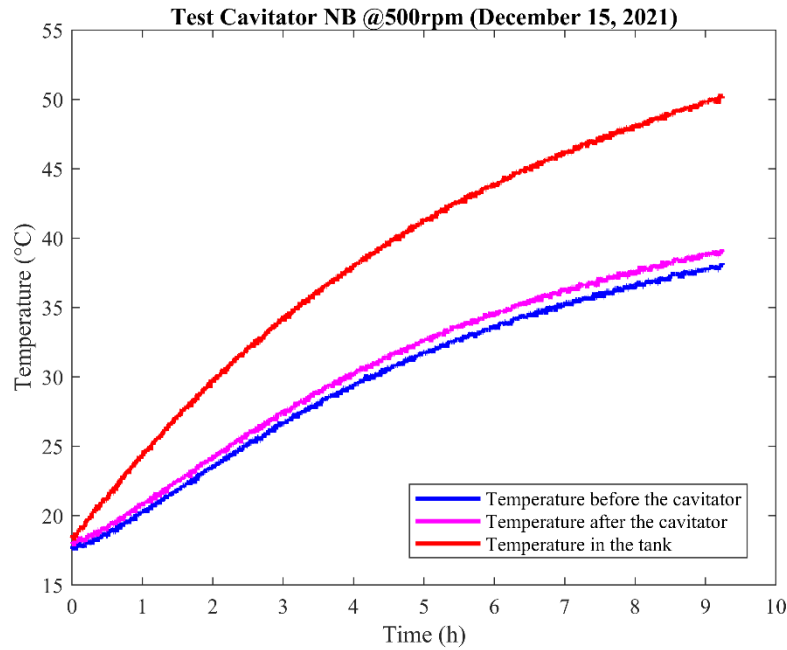


Fig. 2.60 Temperature trends from the test of the 15th of December 2021, cavitator NB, 500rpm.

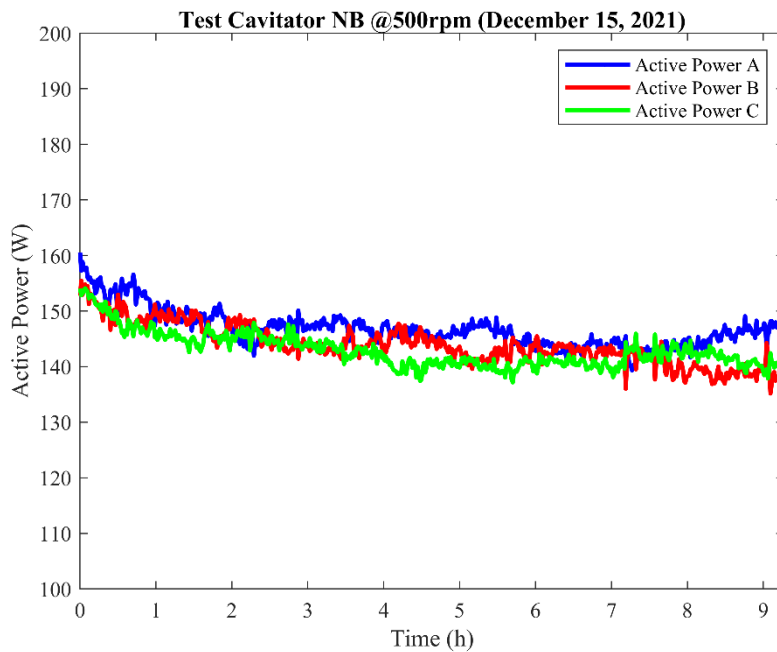


Fig. 2.61 Electric powers provided to the three-phase pump from the test of the 15th of December 2021, cavitator NB, 500rpm.

The next physical quantities were measured:

- mass of the water solution 25 kg;

- initial (environmental) temperature 18.4°C;
- extrapolated steady-state temperature before the cavitator 39.2°C;
- extrapolated steady-state temperature after the cavitator 40.2°C;
- extrapolated steady-state temperature in the tank 52.5°C;
- pressure drop in the cavitator 9.77 bar;
- electric power provided to the pump 433.56 W;
- pump rotation velocity 500 rpm;
- steady-state flow rate of the plant 0.01209 m³/minute;

The ensuing energy contributions were calculated:

- Input electric energy absorbed by the pump $E_{in} = 1560.8 \text{ kJ}$
- Thermal energy stored by the water $E_w = 1391.8 \text{ kJ}$
- Thermal energy dispersed in the environment $E_{disp} = 256.5 \text{ kJ}$
- Hydraulic energy dissipated by the cavitator $E_{mec} = 708.7 \text{ kJ}$

Therefore, the estimate of the COP in steady condition was the following one:

$$\text{COP} = \frac{E_{out}}{E_{in}} = \frac{2357.0 \text{ kJ}}{1560.8 \text{ kJ}} = 1.51 \quad (2.40)$$

The third test on the insulated reactor produced the calorimetric and electric power diagrams depicted in Figs. 2.62-2.63.

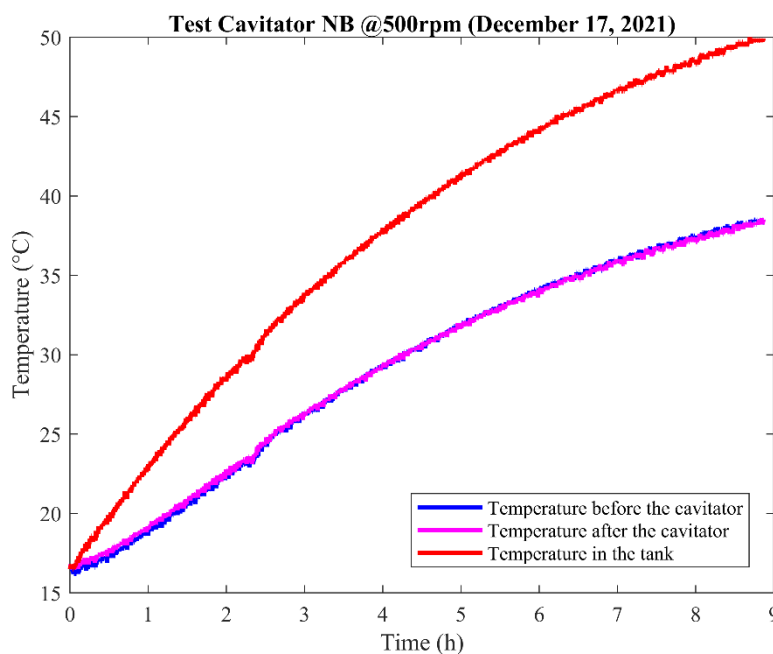


Fig. 2.62 Temperature trends from the test of the 17th of December 2021, cavitator NB, 500rpm.

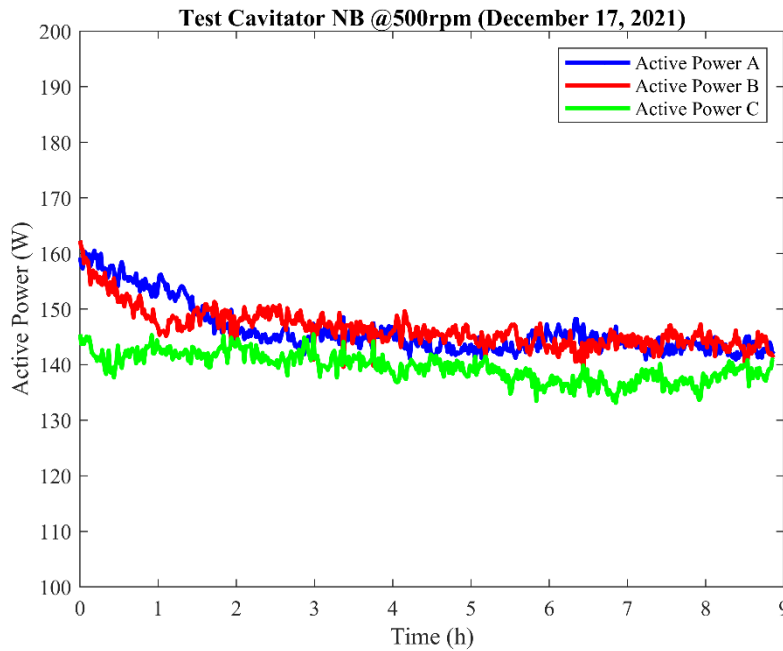


Fig. 2.63 Electric powers provided to the three-phase pump from the test of the 17th of December 2021, cavitator NB, 500rpm.

After the test, the following data were collected:

- mass of the water solution 25 kg;
- initial (environmental) temperature 19.3°C;
- extrapolated steady-state temperature before the cavitator 39.7°C;
- extrapolated steady-state temperature after the cavitator 39.7°C;
- extrapolated steady-state temperature in the tank 52.9°C;
- pressure drop in the cavitator 9.70 bar;
- electric power provided to the pump 432.06 W;
- pump rotation velocity 500 rpm;
- steady-state flow rate of the plant 0.01209 m³/minute;

The next energy contributions to the thermal balance were evaluated:

- Input electric energy absorbed by the pump $E_{in} = 1555.4$ kJ
- Thermal energy stored by the water $E_w = 1381.4$ kJ
- Thermal energy dispersed in the environment $E_{disp} = 251.8$ kJ
- Mechanical energy dissipated by the cavitator $E_{mec} = 703.6$ kJ

The COP in steady-state condition was thus estimated as:

$$\text{COP} = \frac{E_{out}}{E_{in}} = \frac{2336.8 \text{ kJ}}{1555.4 \text{ kJ}} = 1.50 \quad (2.41)$$

The fourth and last insulated test for cavitator NB produced the temperature and electric power trends of Figs. 2.64-2.65, as in the previous cases with a necessary interruption still in transient phase for the supposed technological limitations of the plant.

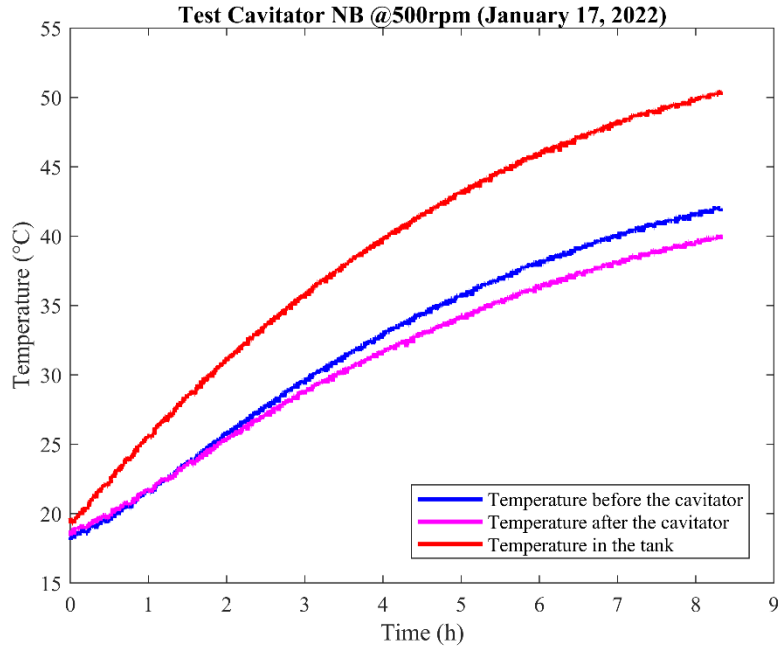


Fig. 2.64 Temperature trends from the test of the 17th of January 2022, cavitator NB, 500rpm.

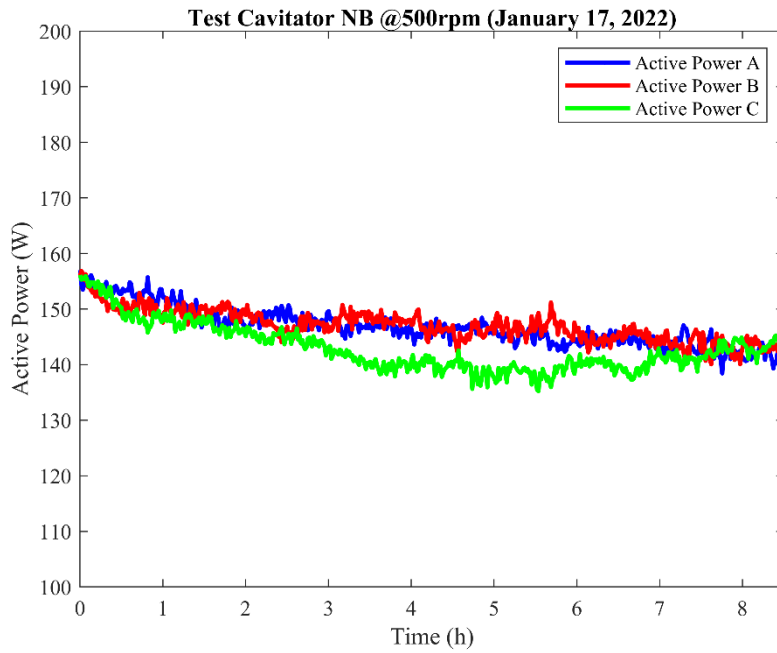


Fig. 2.65 Electric powers provided to the three-phase pump from the test of the 17th of January 2022, cavitator NB, 500rpm.

The physical parameters of the test are reported:

- mass of the water solution 25 kg;
- initial (environmental) temperature 16.5°C;
- extrapolated steady-state temperature before the cavitator 43.3°C;
- extrapolated steady-state temperature after the cavitator 41.7°C;
- extrapolated steady-state temperature in the tank 53.0°C;
- pressure drop in the cavitator 9.93 bar;
- electric power provided to the pump 436.14 W;
- pump rotation velocity 500 rpm;
- steady-state flow rate of the plant 0.01209 m³/minute;

The terms of the energetic balance were calculated at the following values:

- Input electric energy absorbed by the pump $E_{in} = 1570.1$ kJ
- Thermal energy stored by the water $E_w = 1015.1$ kJ
- Thermal energy dispersed in the environment $E_{disp} = 291.0$ kJ
- Mechanical energy dissipated by the cavitator $E_{mec} = 720.4$ kJ

Consequently, COP in steady- state condition was assessed as follows:

$$COP = \frac{E_{out}}{E_{in}} = \frac{2026.5 \text{ kJ}}{1570.1 \text{ kJ}} = 1.29 \quad (2.42)$$

By the analysis of the temperature curves which were registered during the test of the 17th of January 2021, it is clearly possible to observe the anomaly constituted by the fact that the temperature after the cavitator increased slower than the temperature of the section before the nozzle. The told anomaly affects also the COP estimated from the test, which is lower than the average value of the previous attempts of about the 14%.

The superimposition of the thermal trends measured by the thermocouple placed in the tank of the cavitation reactor for the insulated tests on cavitator NB is portrayed in Fig. 2.66.

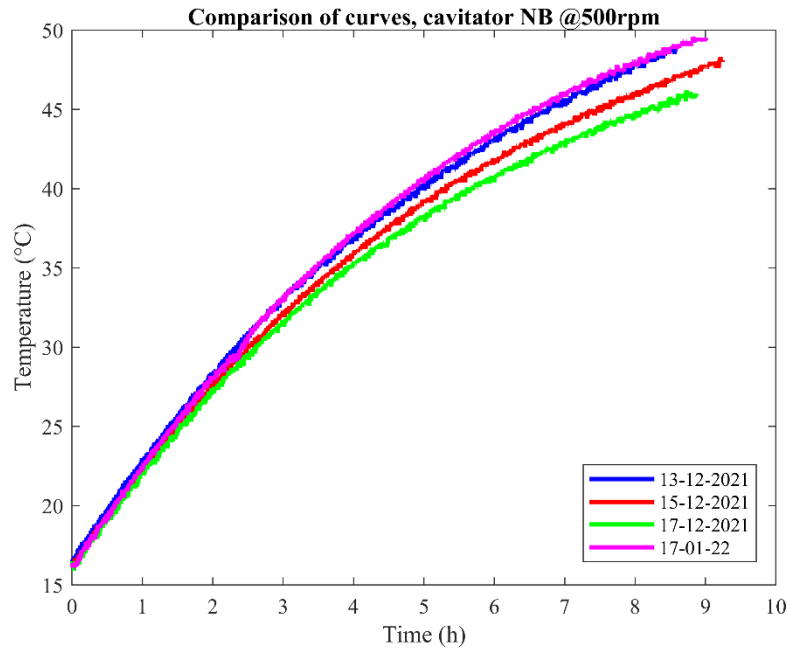


Fig. 2.66 Superimposition of the temperature trends from the insulated tests of cavitator NB at 500rpm.

The final summary of the calorimetric results obtained by means of cavitator NB is given in Tab. 2.11. For the first of the new brass cavitator, the assessment by means of the indirect method allowed to obtain higher values of COP than the average ones of the previous cavitators M2 and M4.

Cavitator NB	
Insulated test (indirect method)	COP
13/12/21	1.49
15/12/21	1.51
17/12/21	1.50
17/01/21	1.29
Average COP	1.45
St. Dev.	0.11
Rel. St. Dev.	7.6%

Tab. 2.11 Summary of the COP obtained with the cavitator NB, indirect method.

Cavitator NM was the second one of the new generation of brass nozzles to be tested from the calorimetric perspective. It was designed, as said, to have a final diameter of dimension equal to 1.4 mm, reached as in the previous cases by sudden reductions of the internal section. By some

preliminary attempts on the new NM cavitator, the impossibility of testing the nozzle at high pump turning velocities was acknowledged. Actually, it was observed that for pump velocities higher than about 300 rpm the flow rate collected by the safety by-pass of the pump tended to clearly overpass the flux collected by the main duct. This phenomenon had the consequence that a considerable part of the electric energy employed by the pump engine was used not to promote cavitation in the solution, but just to establish a useless cyclic flux between the tank and the pump itself. In order to reduce the impact of the by-pass flux on the final thermal balance evaluation, it was decided to adopt for the calorimetric tests on cavitator NM a pump velocity equal to 250rpm, one half of the velocity previously chosen for cavitator NB.

The internal convection heat transfer coefficient adopted for cavitator NM is reported in Tab. 2.12.

Cavitator NM	
Tests at the velocity of 250 rpm	
Ra (-)	8199.22
Nu (-)	555.18
h_i ($\frac{W}{m^2K}$)	28716.38

Tab. 2.12 Rayleigh and Nusselt numbers, internal convection heat transfer coefficient, cavitator NM.

For the first of the four insulated test analysed by the indirect method which were performed for cavitator NM, the trends of the measured temperatures and of the electric power absorptions are portrayed in Figs. 2.67-2.68.

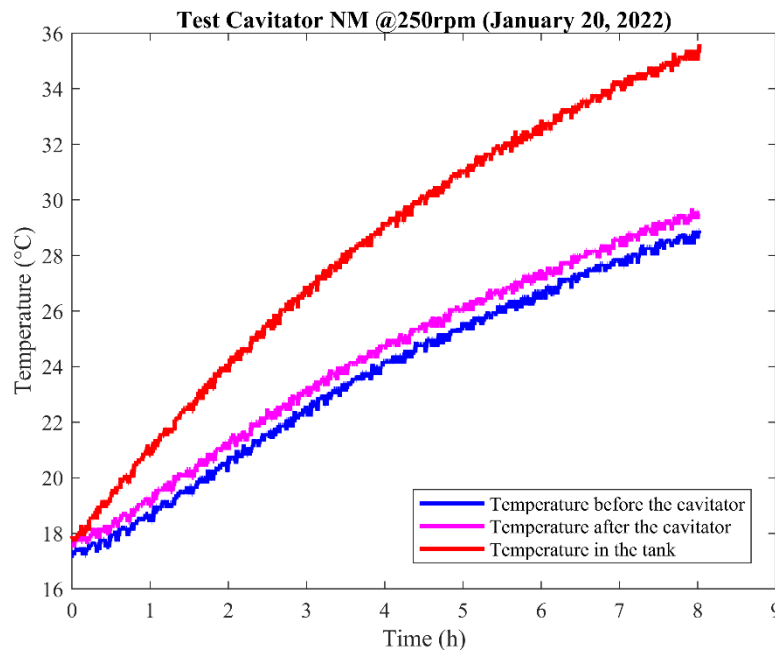


Fig. 2.67 Temperature trends from the test of the 20th of January 2022, cavitator NM, 250rpm.

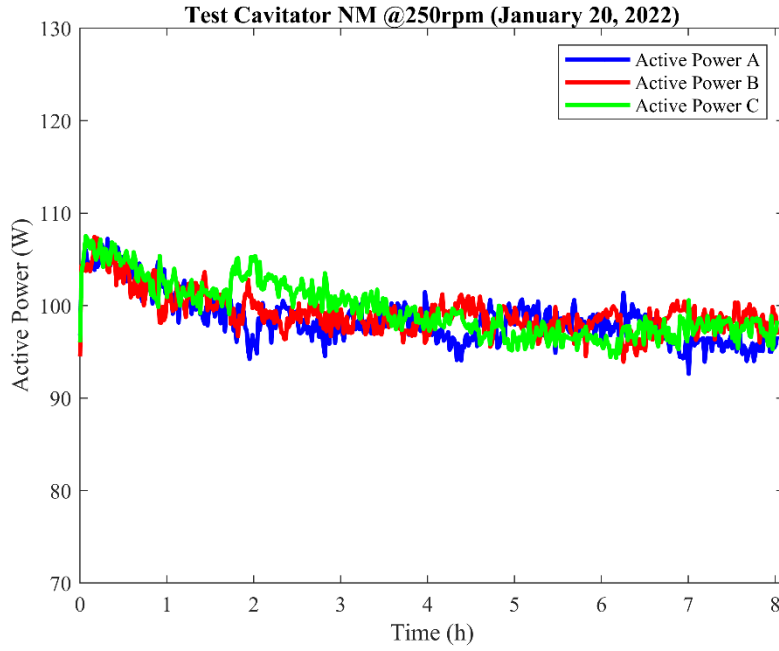


Fig. 2.68 Electric powers provided to the three-phase pump from the test of the 20th of January 2022, cavitator NM, 250rpm.

The ensuing physical quantities were measured:

- mass of the water solution 25 kg;
- initial (environmental) temperature 17.9°C;
- extrapolated steady-state temperature before the cavitator 30.1°C;
- extrapolated steady-state temperature after the cavitator 32.1°C;
- extrapolated steady-state temperature in the tank 38.2°C;
- pressure drop in the cavitator 12.61 bar;
- electric power provided to the pump 297.32 W;
- pump rotation velocity 250 rpm;
- steady-state flow rate of the plant 0.00448 m³/minute;

The next energy contributions were calculated:

- Input electric energy absorbed by the pump $E_{in} = 1070.4$ kJ
- Thermal energy stored by the water $E_w = 847.7$ kJ
- Thermal energy dispersed in the environment $E_{disp} = 152.5$ kJ
- Mechanical energy dissipated by the cavitator $E_{mec} = 338.9$ kJ

According to the indirect method, the COP in steady-state condition was then assessed as follows:

$$\text{COP} = \frac{E_{out}}{E_{in}} = \frac{1339.1 \text{ kJ}}{1070.4 \text{ kJ}} = 1.25 \quad (2.43)$$

The monitoring of the thermal and electric power supply trends fulfilled during the second test on the insulated plant allowed to obtain the curves reported in Figs. 2.69-2.70.

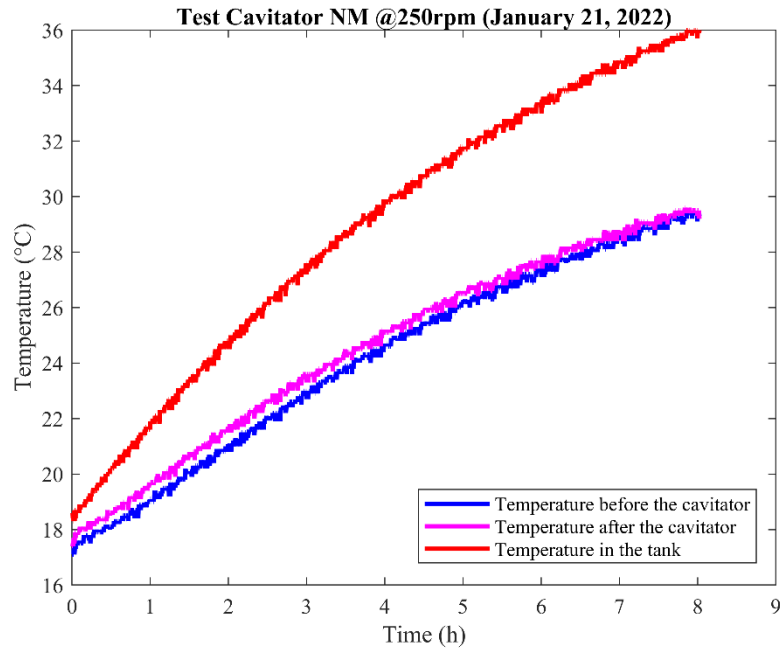


Fig. 2.69 Temperature trends from the test of the 21st of January 2022, cavitator NM, 250rpm.

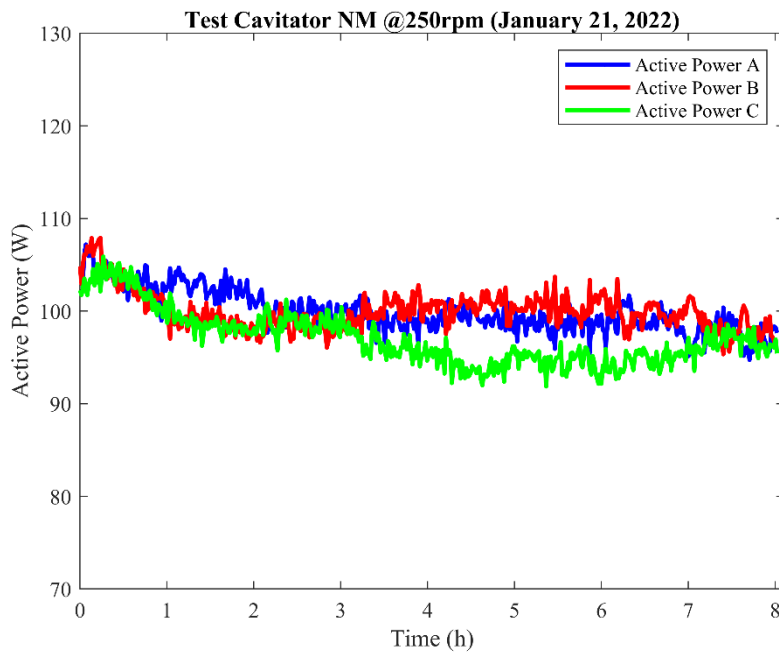


Fig. 2.70 Electric powers provided to the three-phase pump from the test of the 21st of January 2022, cavitator NM, 250rpm.

During the test, the following physical data were collected:

- mass of the water solution 25 kg;

- initial (environmental) temperature 18.6°C;
- extrapolated steady-state temperature before the cavitator 30.3°C;
- extrapolated steady-state temperature after the cavitator 30.5°C;
- extrapolated steady-state temperature in the tank 39.3°C;
- pressure drop in the cavitator 12.64 bar;
- electric power provided to the pump 296.93 W;
- pump rotation velocity 250 rpm;
- steady-state flow rate of the plant 0.00448 m³/minute;

The input and output energy terms were then evaluated as follows:

- Input electric energy absorbed by the pump $E_{in} = 1069.0 \text{ kJ}$
- Thermal energy stored by the water $E_w = 941.9 \text{ kJ}$
- Thermal energy dispersed in the environment $E_{disp} = 151.8 \text{ kJ}$
- Mechanical energy dissipated by the cavitator $E_{mec} = 339.7 \text{ kJ}$

Therefore, the reported COP in steady-state condition was estimated:

$$\text{COP} = \frac{E_{out}}{E_{in}} = \frac{1433.4 \text{ kJ}}{1069.0 \text{ kJ}} = 1.34 \quad (2.44)$$

The third test on the insulated plant produced the calorimetric and electric power absorption results depicted in Figs. 2.71-2.72.

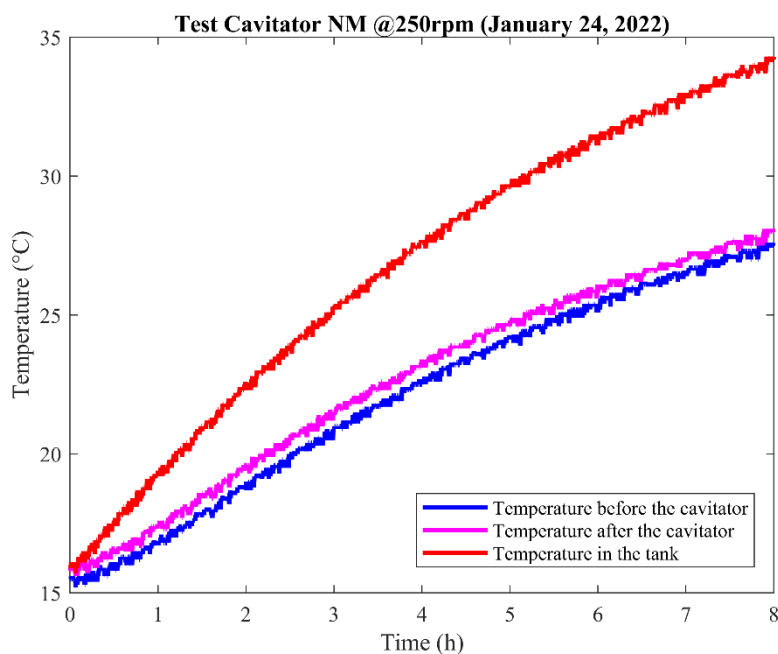


Fig. 2.71 Temperature trends from the test of the 24th of January 2022, cavitator NM, 250rpm.

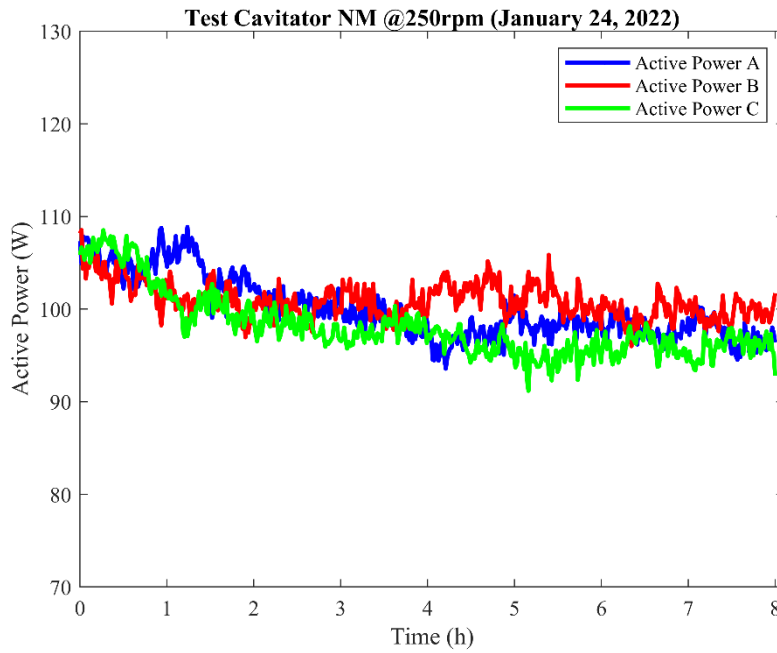


Fig. 2.72 Electric powers provided to the three-phase pump from the test of the 24th of January 2022, cavitator NM, 250rpm.

The physical parameters of the test are enclosed in the following list:

- mass of the water solution 25 kg;
- initial (environmental) temperature 16.0°C;
- extrapolated steady-state temperature before the cavitator 28.2°C;
- extrapolated steady-state temperature after the cavitator 28.6°C;
- extrapolated steady-state temperature in the tank 37.6°C;
- pressure drop in the cavitator 12.76 bar;
- electric power provided to the pump 298.87 W;
- pump rotation velocity 250 rpm;
- steady-state flow rate of the plant 0.00448 m³/minute;

From the previous data, the energy contributions were calculated:

- Input electric energy absorbed by the pump $E_{in} = 1075.9$ kJ
- Thermal energy stored by the water $E_w = 983.7$ kJ
- Thermal energy dispersed in the environment $E_{disp} = 158.4$ kJ
- Mechanical energy dissipated by the cavitator $E_{mec} = 343.0$ kJ

The COP in steady-state condition was then assessed as follows:

$$\text{COP} = \frac{E_{out}}{E_{in}} = \frac{1485.1 \text{ kJ}}{1075.9 \text{ kJ}} = 1.38 \quad (2.45)$$

The temperature curves and electric power supplies of the three-phase pump engine registered during the fourth attempt on the insulated reactor equipped by cavitator NM are shown in Figs. 2.73-2.74.

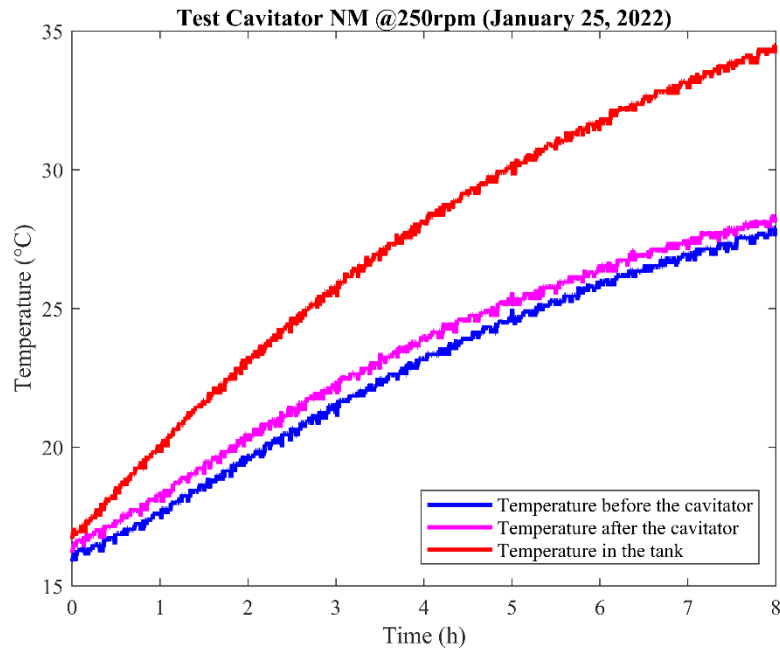


Fig. 2.73 Temperature trends from the test of the 25th of January 2022, cavitator NM, 250rpm.

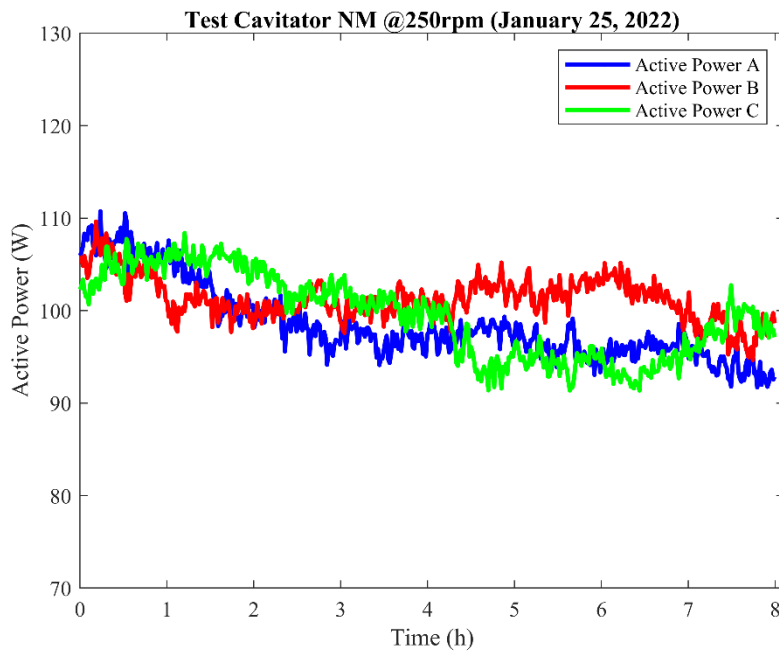


Fig. 2.74 Electric powers provided to the three-phase pump from the test of the 25th of January 2022, cavitator NM, 250rpm.

The following physical quantities were noted:

- mass of the water solution 25 kg;
- initial (environmental) temperature 16.8°C;
- extrapolated steady-state temperature before the cavitator 28.2°C;
- extrapolated steady-state temperature after the cavitator 28.8°C;
- extrapolated steady-state temperature in the tank 37.5°C;
- pressure drop in the cavitator 12.84 bar;
- electric power provided to the pump 299.29 W;
- pump rotation velocity 250 rpm;
- steady-state flow rate of the plant 0.00448 m³/minute;

The next energy terms were thus evaluated:

- Input electric energy absorbed by the pump $E_{in} = 1077.4 \text{ kJ}$
- Thermal energy stored by the water $E_w = 973.2 \text{ kJ}$
- Thermal energy dispersed in the environment $E_{disp} = 151.1 \text{ kJ}$
- Mechanical energy dissipated by the cavitator $E_{mec} = 345.0 \text{ kJ}$

The estimate of the COP in steady-state condition provided the following result:

$$\text{COP} = \frac{E_{out}}{E_{in}} = \frac{1469.3 \text{ kJ}}{1077.4 \text{ kJ}} = 1.36 \quad (2.46)$$

The repeatability of the results obtained in terms of temperature paths with reference to the thermocouple placed in the tank is highlighted by the low variances between the curves of the insulated-plant tests portrayed in Fig. 2.75.

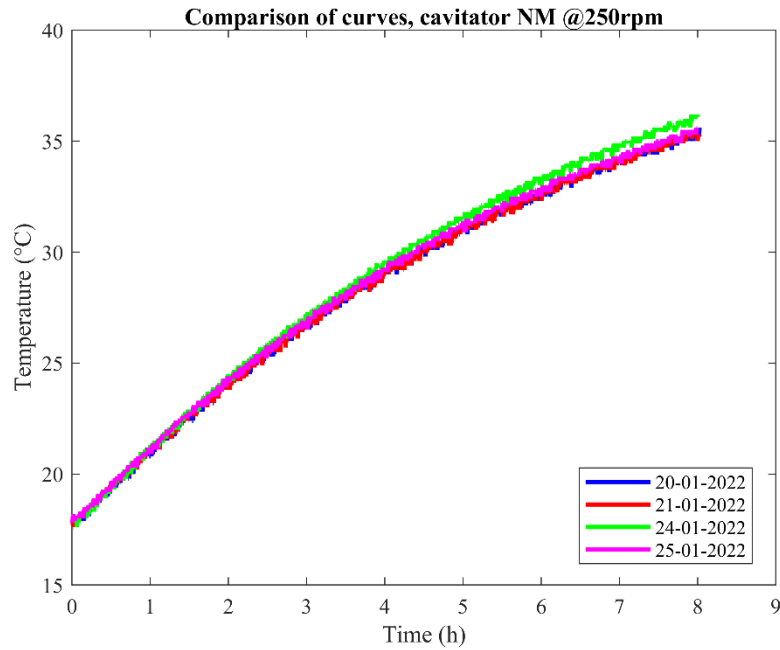


Fig. 2.75 Superimposition of the temperature trends from the insulated tests of cavitator NM at 250rpm.

The recapitulatory table which shows the COP obtained for cavitator NM (Tab. 2.13) allows to formulate an important consideration about the new nozzle: although the reduced final diameter of the nozzle had forced to a reduction of the 50% of the velocity of the pump, aimed to limit the flow rate through the by-pass, a still relevant extra-heat generation was revealed. This effect was detected even though the noticeable reduction of the flux through the cavitator (due to the lower ultimate section of the throat and the lower velocity of the pump), which caused a lower final temperature in the tank and a limited difference in temperature from the environmental one. The previous observation might lead to define the reduction of the throat section as a positive factor for the promotion of cavitation and of the production of nano-bubbles in the solution. To explore this possibility, a new series of tests would probably be done in the future on new-concept cavitators provided with more holes of lower diameters, that would allow to reach higher flow rates without needing the enlargement of the final section nor the adoption of more performing pumps.

Cavitator NM	
Insulated test (indirect method)	COP
20/01/22	1.25
21/01/22	1.34
24/01/22	1.38
25/01/22	1.36

Average COP	1.33
St. Dev.	0.06
Rel. St. Dev.	4.5%

Tab. 2.13 Summary of the COP obtained with the cavitator NM, indirect method.

Cavitator NS, which had been designed to have a final diameter of 0.7 mm, was the last of the three cavitators of the new generation to be thermally tested. Analogously to what had been needed to be done for cavitator NM, a further reduction of the pump turning velocity was essential in this case. The main reason of the reduction was that the too high pressures revealed in the pump for values higher than about 200-220 rpm caused the activation of the safety by-pass of the pump itself with an excessive flow rate. As a first attempt, an additional reduction of the 50% of the pump velocity was tested (down to 125rpm). The temperature curves and the electric power absorptions registered under the previous condition for the non-insulated plant during the first trial attempt are portrayed in Figs. 2.76-2.77.

Tab. 2.14 provides the Rayleigh and Nusselt number and the internal convection heat transfer coefficient evaluated for cavitator NS.

Cavitator NS	
Test at the velocity of 125 rpm	
Ra (-)	3475.80
Nu (-)	235.35
h_i ($\frac{W}{m^2K}$)	12173.39

Tab. 2.14 Rayleigh and Nusselt numbers, internal convection heat transfer coefficient, cavitator NS.

As far as the assessment method for COP is concerned, for the non-insulated test on cavitator NS the direct evaluation of COP was possible to be accomplished, since the steady-state condition had been reached.

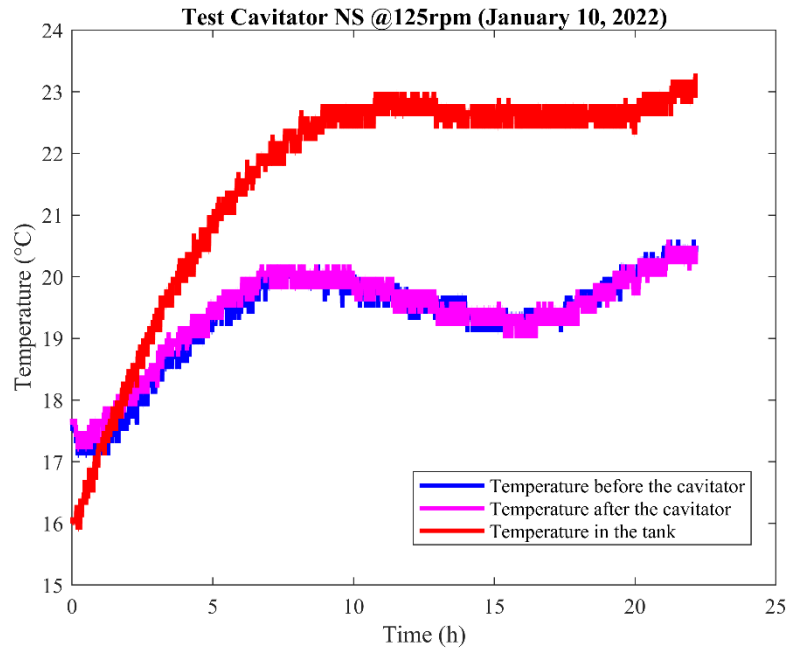


Fig. 2.76 Temperature trends from the test of the 10th of January 2022, cavitator NS, 250rpm.

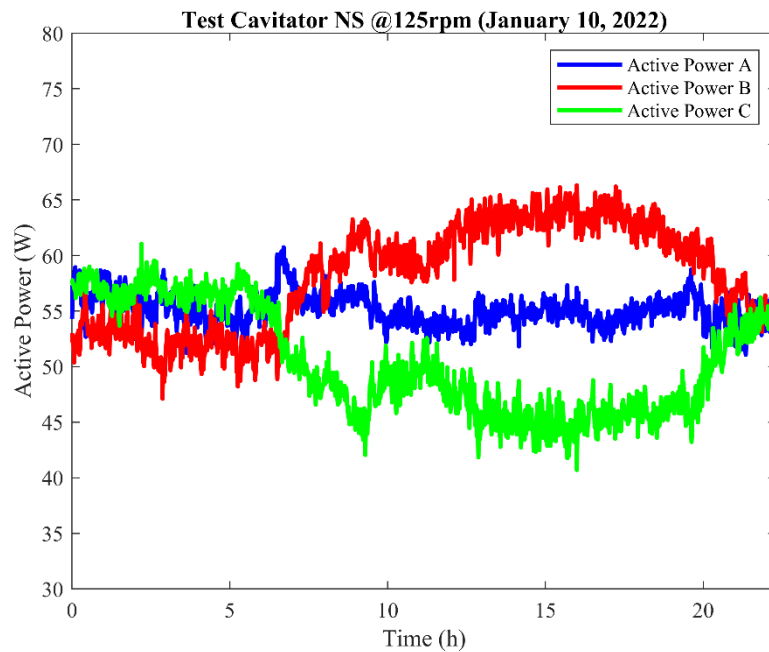


Fig. 2.77 Electric powers provided to the three-phase pump from the test of the 10th of January 2022, cavitator NS, 250rpm.

The following physical data were considered in the evaluations:

- mass of the water solution 25 kg;
- initial (environmental) temperature 16.0°C;
- steady-state temperature before the cavitator 19.7°C;
- steady-state temperature after the cavitator 19.7°C;
- steady-state temperature in the tank 22.7°C;

- pressure drop in the cavitator 9.60 bar;
- electric power provided to the pump 163.67 W;
- pump rotation velocity 250 rpm;
- steady-state flow rate of the plant 0.0019 m³/minute;

The next energy contributions in the steady-state condition were calculated as follows:

- Input electric energy absorbed by the pump $E_{in} = 589.2 \text{ kJ}$
- Thermal energy stored by the water $E_w = 314.0 \text{ kJ}$
- Thermal energy dispersed in the environment $E_{disp} = 100.4 \text{ kJ}$
- Mechanical energy dissipated by the cavitator $E_{mec} = 109.2 \text{ kJ}$

From the previous terms, the Coefficient of Performance of the non-insulated cavitation reactor was evaluated:

$$\text{COP} = \frac{E_{out}}{E_{in}} = \frac{523.6 \text{ kJ}}{589.2 \text{ kJ}} = 0.89 \quad (2.47)$$

It is worth noting that the further reduction of the flux through the cavitator produced both a reduction of the measured COP and a reduction of the steady-state temperature in the tank, that in this case was detected to be only about 4°C above the starting environmental temperature. Some other attempts at higher pump velocities could be done for this last cavitator and rather higher COP values are expected to be revealed. Nevertheless, also for the cavitator with a final diameter equal to 0.7 mm, the most interesting advancements seem to be possible to be obtained by means of cavitators produced with several holes, in order to ensure more relevant water flow rates.

Chapter 3

Optic tests for the determination of the dimension and the energy per imploded nano-bubble

3.1 Phase Doppler Anemometry technique

Subsequently to the first phase of the calorimetric tests, the three best brass cavitators of the first generation were tested from the so called “optic” perspective, which focused on the measurement of the dimensions and the number of the bubbles produced by effect of the passage of the fluid through each nozzle.

In order to measure those parameters, the Phase Doppler Anemometry (PDA) technique was used, which bases on the laser interferometry to measure the dimensions, velocity and concentration of spherical particles suspended in liquid or gaseous means. These spherical particles can be constituted by bubbles in a fluid (as in the case of interest) or also small drops. The instrument is equipped by two laser emitters pointing on a lens that diverts the laser beams and forces them to converge in a small area. The small area given by the intersection of the two laser beams is called “monitoring section”, a term that for the case of a flux it is possible to refer both to an area, knowing the fluid velocity, or to a volume. Here the light beams encounter the surfaces of the spherical bubbles suspended in the fluid (with their own velocities), they are refracted with different angles and then received by detectors, at least two, called “photo multipliers” and placed on the opposite side with respect to the emitters. A scheme of the measurement process is shown in Fig. 3.1.

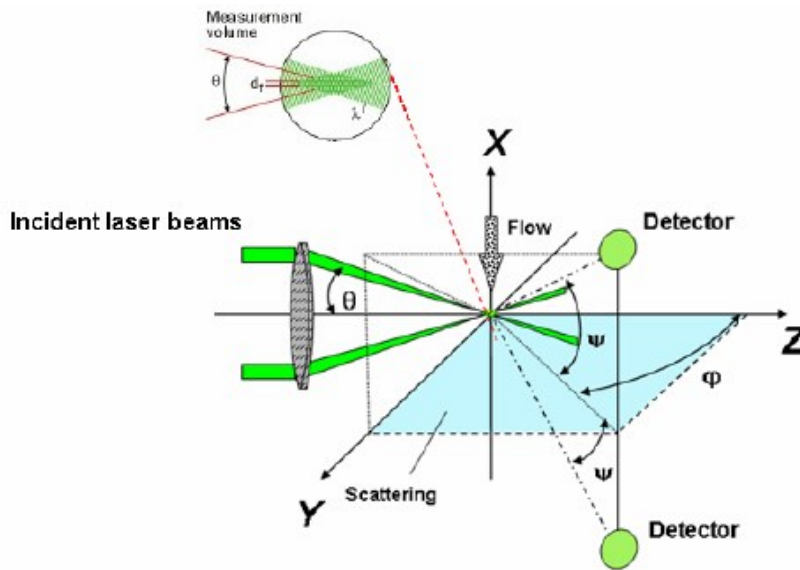


Fig. 3.1 Phase Doppler Anemometry behaviour.

The Doppler effect allows the measurement of the velocity of the bubbles in the fluid because of the fact that the frequency of the laser beam is modified by the passage through a bubble proportionally to its velocity. Therefore, the velocity can be determined from the difference between the emitted and the received frequencies. Instead, the difference in phase of the signals collected by the at least two receivers allows to determine the diameter of the bubble in the monitoring volume or section. On the bases of what has been declared, the detection of the quantities of interest is done by just the survey of the frequencies and phases of the laser beams emitted. The measurement apparatus for PDA adopted in the optic tests was characterised by a monitoring section of about 0.125 mm^2 and a sensitivity to bubbles with dimensions of orders of magnitude between the hundred of nanometres and the millimetre. In Fig. 3.2 the optic test setup is shown.

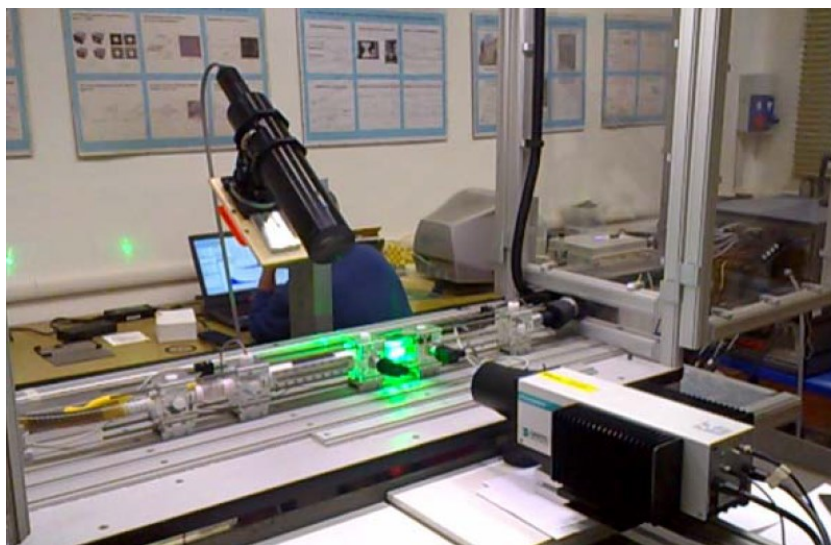


Fig. 3.2 Phase Doppler Anemometry measurement setup.

The sampling technique adopted was based on the acquisition of 20.000 spherical bubbles in a time set to a maximum duration of 100 seconds for every measure, in order to assess velocities and dimensions of the bubbles and their relative statistical distributions. Therefore, a statistic on basis 20.000 bubbles was done for the parameters measured by Phase Doppler Anemometry. If less than 20.000 bubbles were sampled during the time interval of 100 seconds, the monitoring system would have displayed the real number of bubbles found and the confidence factor of the data collected. This would have allowed to consider this data, if a plausible value had been got, or to neglect it and stop the test if the number of bubbles in the 100 seconds was judged to be too low, leading then to the evaluation of the causes of the anomaly (such as poor test setup, poor choice of the geometry of the cavitator or disruptions of the plant). It is important to underline that the PDA technique is able to evaluate dimensions and velocities just of spherical bubbles and not of suspended particles of other shapes. The spherical gaseous inclusions were but assumed to be the most common ones for the test setup and the geometries of the cavitators adopted.

As previously said, the detection capability of the PDA is limited between the magnitudes of the hundred of nanometres and the millimetre, but the bubble diameters in the range of interest for the production of TeraHertz phonons in the fluid have smaller dimensions, around the nanometre. The problem of determining the number of the bubbles of nanometric dimensions was solved by statistic extrapolation from the effectively measured occurrence rates of the greater dimensions by means of the assumption of a gaussian statistical distribution.

3.2 Optic test results for the best three brass cavitators: number and dimension of the bubbles produced

The optic tests were conducted by adopting increasing fluid pressure levels, which were established at 2 atm, 3 atm, 3.5 atm, 4 atm, 4.5 atm, 5 atm, 6 atm, 7 atm and 8 atm, and in the case of study focused mainly on the measurement of the dimensions of the bubbles rather than on their velocities. The two lower pressure levels were chosen to be lower than the pressure threshold of the cavitation, detected at about 4 atmospheres during the acoustic tests (for the actual geometries of the cavitators). The results of these attempts have been neglected in the treatise, since they did not promote a significant bubble production. The highest pressures tested were defined at the previously declared values for the double reason of avoiding excessive background noise in the previous acoustic characterisation and of evaluating the potentialities of reduced velocity tests for the promotion of relevant thermal efficiencies. The most significant results were obtained in the field of

pressures between 3.5 and 6 atm. In the following, just these optical monitoring data are going to be analysed with reference to the three best brass cavitators of the first generation. The three best nozzles had been recognised to be the M2, M4 and M5 from the first calorimetric tests.

The tests started from the cavitator M2. Its internal geometry was characterised by three different diameters which reduced down to the final value of 2.7 mm by means of sharp-edge transitions. As previously outlined, the first cavitation phenomena were observed departing from a fluid pressure of 3.5 atm. The curve of the found dimensional distribution is depicted in Fig. 3.3, and it was obtained by means of the normalisation of the values on the ordinate axis through the division by the maximum dimensional recurrence.

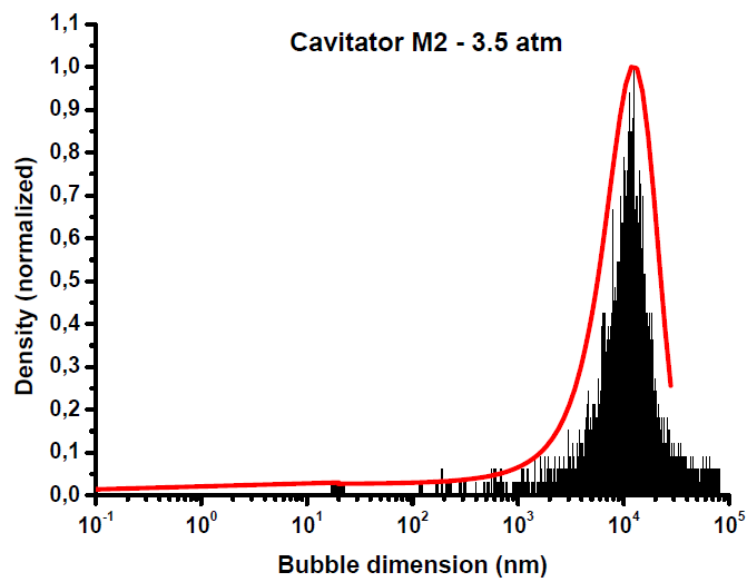


Fig. 3.3 Dimensional distribution of the bubbles, cavitator M2, 3.5 atm.

By extrapolation by means of the shown gaussian distribution, the percentages of the bubble dimensions on the whole population of Tab. 3.1 were got.

CAVITATOR M2	
Pressure: 3.5 atm	
Bubble dimension (nm)	Quantity
0.1 – 1	0.0007%
1 – 10	0.009%
10 – 100	0.11%
100 – 1000	0.21%
1000 – 10000	24.81%

>10000	74.88%
--------	--------

Tab. 3.1 Dimensional distribution of the bubbles, cavitator M2, 3.5 atm.

As it is possible to note, the peak of the gaussian curve and the greatly major percentage of the bubbles produced were around to or higher than 10^4 nm, but a little population of nano-bubbles (considering with this term mainly the ones in the range 0.1-10 nm) were produced at the same time. This population maintained an almost constant value by passing to a pressure of 4 atmospheres, as shown in Fig. 3.4 and Tab. 3.2.

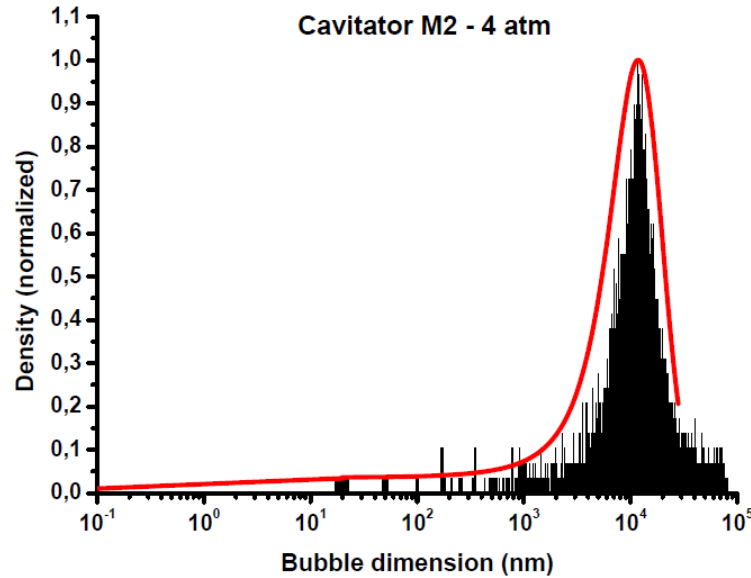


Fig. 3.4 Dimensional distribution of the bubbles, cavitator M2, 4 atm.

CAVITATOR M2	
Pressure: 4 atm	
Bubble dimension (nm)	Quantity
0.1 – 1	0.0004%
1 – 10	0.008%
10 – 100	0.12%
100 – 1000	0.23%
1000 – 10000	22.93%
>10000	76.72%

Tab. 3.2 Dimensional distribution of the bubbles, cavitator M2, 4 atm.

An increase in the population of the nano-bubbles (0.1-10 nm) was noticed at 4.5 atm, as can be seen from Fig. 3.5 and Tab. 3.3.

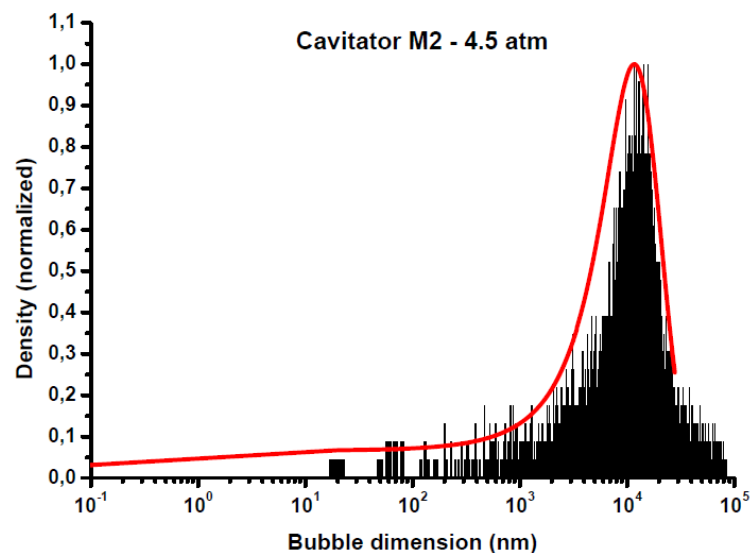


Fig. 3.5 Dimensional distribution of the bubbles, cavitator M2, 4.5 atm.

CAVITATOR M2	
Pressure: 4.5 atm	
Bubble dimension (nm)	Quantity
0.1 – 1	0.001%
1 – 10	0.02%
10 – 100	0.24%
100 – 1000	0.52%
1000 – 10000	23.11%
>10000	76.12%

Tab. 3.3 Dimensional distribution of the bubbles, cavitator M2, 4.5 atm.

By increasing the pressure of the fluid, at first to 5 atmospheres and then to 6, a new decrease of the number of nano-bubbles was detected (more relevant for the higher pressure) as it is possible to be noted in Figs. 3.6-3.7 and Tabs. 3.4-3.5.

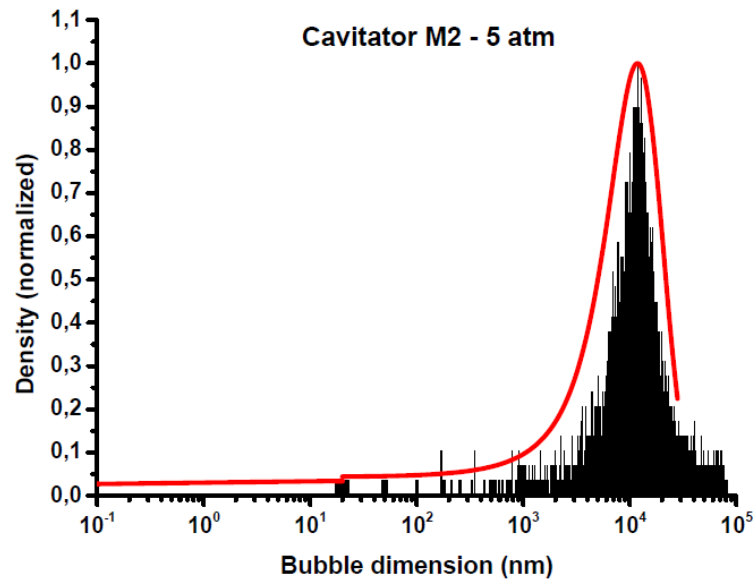


Fig. 3.6 Dimensional distribution of the bubbles, cavitator M2, 5 atm.

CAVITATOR M2	
Pressure: 5 atm	
Bubble dimension (nm)	Quantity
0.1 – 1	0.0007%
1 – 10	0.009%
10 – 100	0.11%
100 – 1000	0.23%
1000 – 10000	22.93%
>10000	76.73%

Tab. 3.4 Dimensional distribution of the bubbles, cavitator M2, 5 atm.

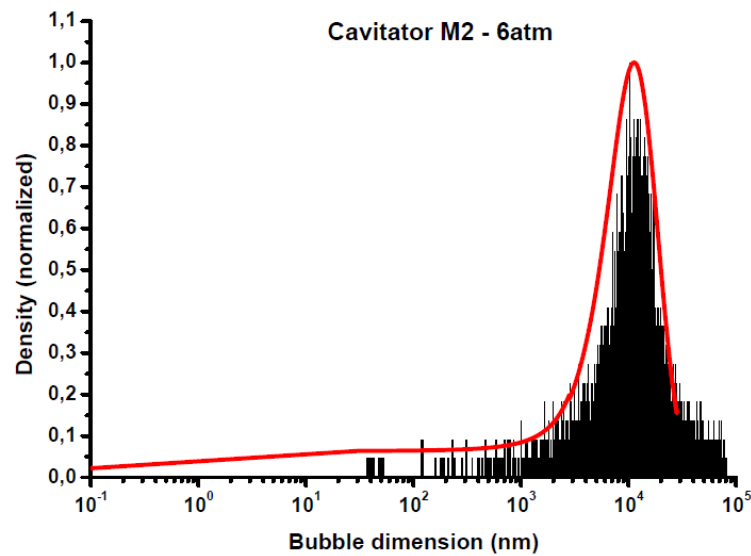


Fig. 3.7 Dimensional distribution of the bubbles, cavitator M2, 6 atm.

CAVITATOR M2	
Pressure: 6 atm	
Bubble dimension (nm)	Quantity
0.1 – 1	0.0004%
1 – 10	0.006%
10 – 100	0.08%
100 – 1000	0.36%
1000 – 10000	23.45%
>10000	76.32%

Tab. 3.5 Dimensional distribution of the bubbles, cavitator M2, 6 atm.

The optic experimentation was accomplished then on the cavitator M5, the second of the best three ones that have been tested. The geometry of the cavitator is similar to previous one since it has three progressively reducing internal diameters and sudden changes of section, but in this case for different lengths.

The result of the test at 3.5 atmospheres is reported in Fig. 3.8 and in Tab. 3.5, that revealed a low production of nano-bubbles.

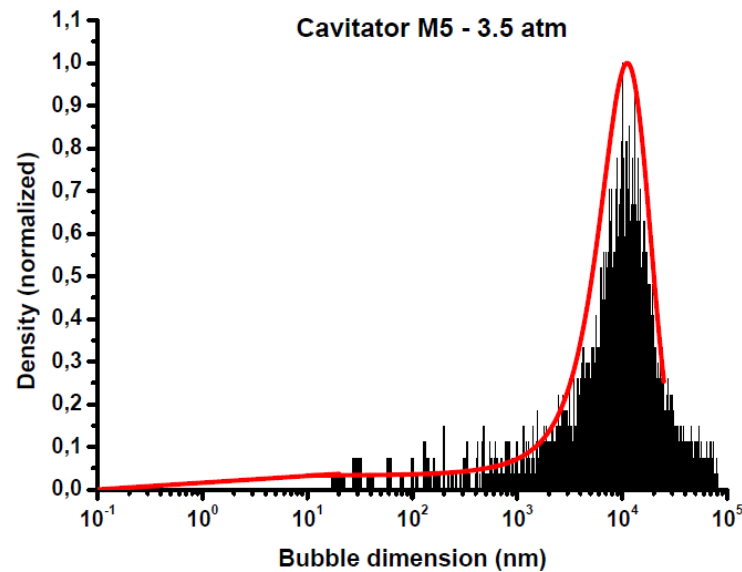


Fig. 3.8 Dimensional distribution of the bubbles, cavitator M5, 3.5 atm.

CAVITATOR M5

Pressure: 3.5 atm	
Bubble dimension (nm)	Quantity
0.1 – 1	0.0001%
1 – 10	0.0025%
10 – 100	0.035%
100 – 1000	0.535%
1000 – 10000	28.10%
>10000	71.33%

Tab. 3.6 Dimensional distribution of the bubbles, cavitator M5, 3.5 atm.

A slight increase in the nano-bubble population was observed for the pressure of 4 atm (Fig. 3.9 and Tab. 3.7).

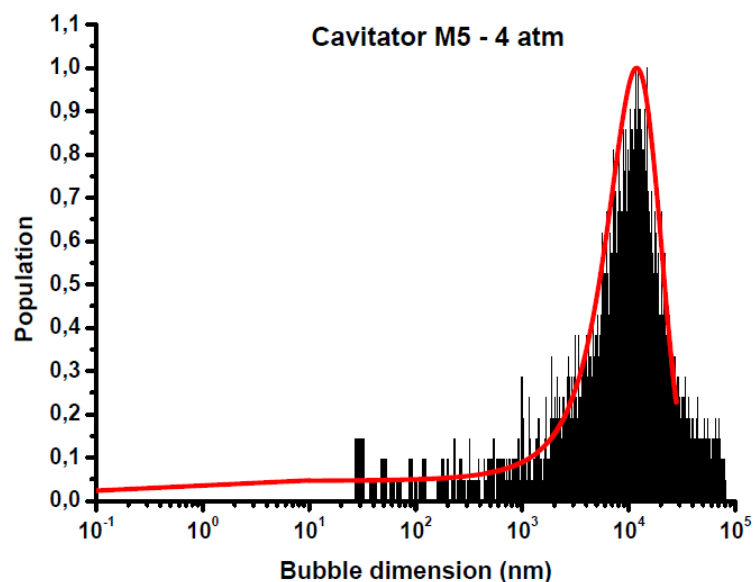


Fig. 3.9 Dimensional distribution of the bubbles, cavitator M5, 4 atm.

CAVITATOR M5	
Pressure: 4 atm	
Bubble dimension (nm)	Quantity
0.1 – 1	0.0003%
1 – 10	0.004%
10 – 100	0.05%
100 – 1000	0.53%
1000 – 10000	25.80%

>10000	73.62%
--------	--------

Tab. 3.7 Dimensional distribution of the bubbles, cavitator M5, 4 atm.

Passing then to 4.5 atm, no relevant further increase in the number of nano-bubbles was found, but a noticeable one in the number of greater bubbles was observed, with diameters larger than 10^4 nm, as can be seen in Fig. 3.10 and Tab. 3.8.

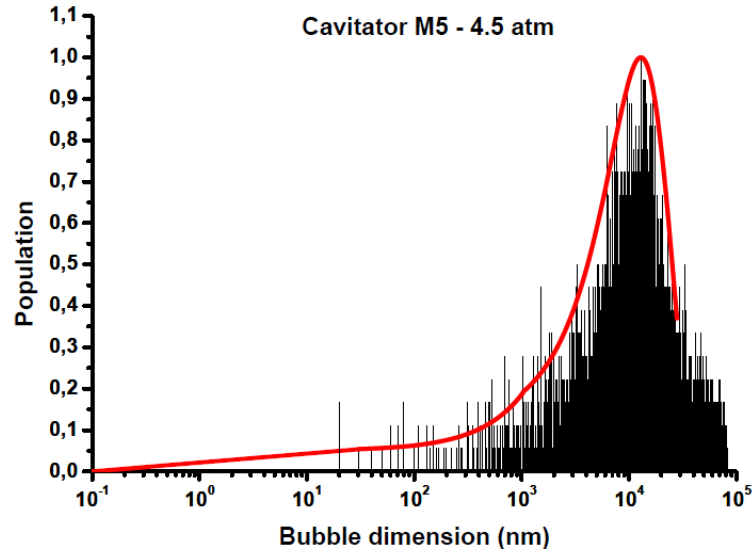


Fig. 3.10 Dimensional distribution of the bubbles, cavitator M5, 4.5 atm.

CAVITATOR M5	
Pressure: 4.5 atm	
Bubble dimension (nm)	Quantity
0.1 – 1	0.0003%
1 – 10	0.005%
10 – 100	0.065%
100 – 1000	0.55%
1000 – 10000	22.24%
>10000	77.14%

Tab. 3.8 Dimensional distribution of the bubbles, cavitator M5, 4.5 atm.

The population of the nano-bubbles increased instead for the passage to 5 atmospheres of fluid pressure (Fig. 3.11 and Tab. 3.9).

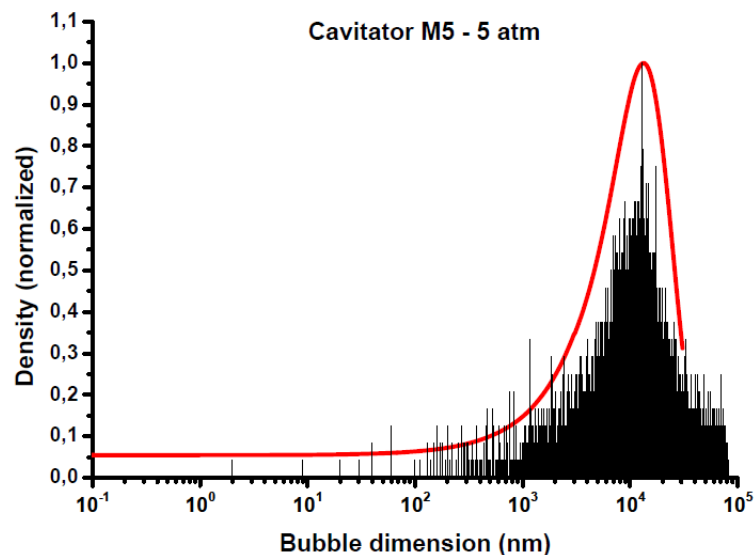


Fig. 3.11 Dimensional distribution of the bubbles, cavitor M5, 5 atm.

CAVITATOR M5	
Pressure: 5 atm	
Bubble dimension (nm)	Quantity
0.1 – 1	0.001%
1 – 10	0.011%
10 – 100	0.045%
100 – 1000	0.63%
1000 – 10000	23.84%
>10000	75.34%

Tab. 3.9 Dimensional distribution of the bubbles, cavitor M5, 5 atm.

By reaching the pressure of 6 atmospheres, the decrease of the concentration of the nano-bubbles was noticed to be accompanied by a further increase in the population of greater bubbles, as shown in Fig. 3.12 and Tab. 3.10.

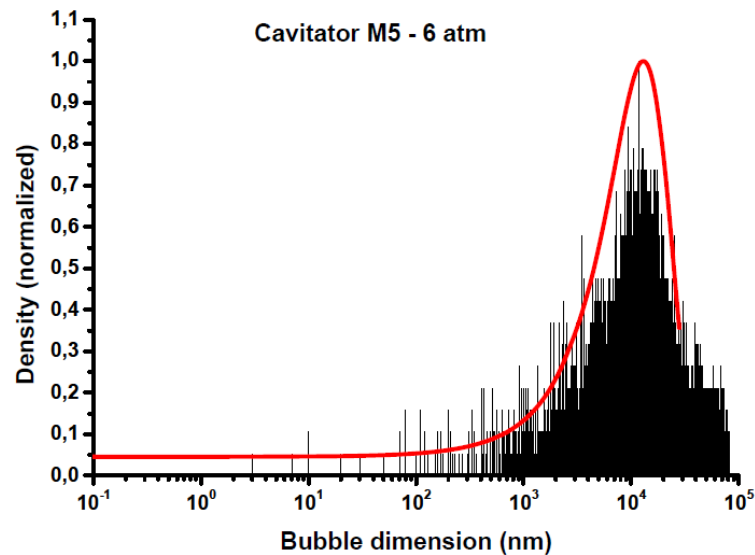


Fig. 3.12 Dimensional distribution of the bubbles, cavitator M5, 6 atm.

CAVITATOR M5	
Pressure: 6 atm	
Bubble dimension (nm)	Quantity
0.1 – 1	0.0005%
1 – 10	0.005%
10 – 100	0.045%
100 – 1000	0.63%
1000 – 10000	23.84%
>10000	75.34%

Tab. 3.10 Dimensional distribution of the bubbles, cavitator M5, 6 atm.

Cavitator M4 was the last of the three best cavitators for the number of nano-bubble produced to be tested. As a difference from the previous two cases, the geometry of this cavitator has been changed not only in the length of the inner sections having constant diameters but also in the intermediate internal diameter of the throat section itself.

After the test at 3.5 atmospheres with cavitator M4, the lowest percentage of nano-bubbles of the field 0.1-10 nm measured during all the optic experimentation campaign was detected, as well as a peak of the gaussian curve for the first time in the field of dimensions $10^3 - 10^4$ nm (Fig. 3.13 and Tab. 3.11).

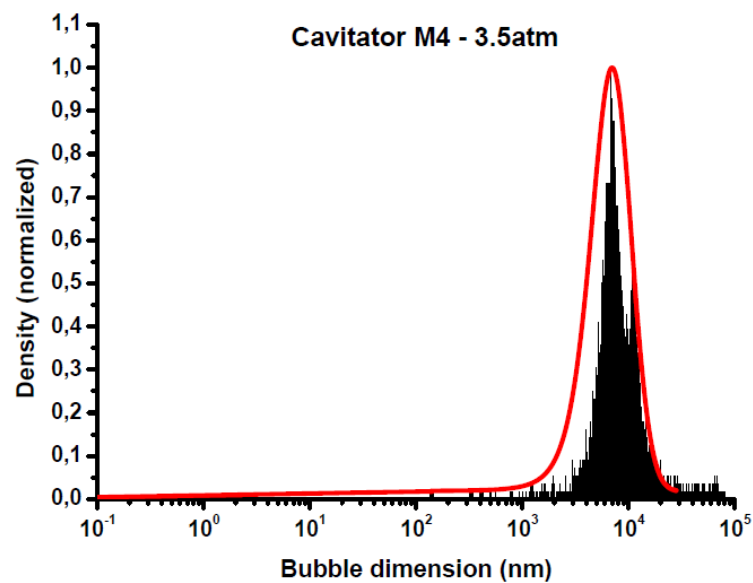


Fig. 3.13 Dimensional distribution of the bubbles, cavitator M4, 3.5 atm.

CAVITATOR M4	
Pressure: 3.5 atm	
Bubble dimension (nm)	Quantity
0.1 – 1	0.00006%
1 – 10	0.001%
10 – 100	0.02%
100 – 1000	0.26%
1000 – 10000	63.09%
>10000	36.65%

Tab. 3.11 Dimensional distribution of the bubbles, cavitator M4, 3.5 atm.

A noticeable increase in the nano-bubbles population was observed by increasing the fluid pressure up to 4 atm, again with the peak of the gaussian curve below the value of 10^4 nm (Fig. 3.14 and Tab. 3.11).

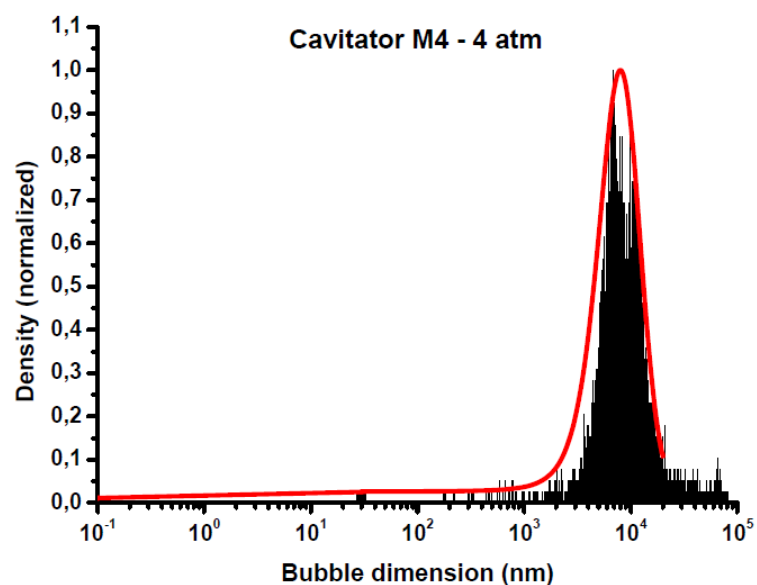


Fig. 3.14 Dimensional distribution of the bubbles, cavitator M4, 4 atm.

CAVITATOR M4	
Pressure: 4 atm	
Bubble dimension (nm)	Quantity
0.1 – 1	0.0006%
1 – 10	0.008%
10 – 100	0.04%
100 – 1000	0.11%
1000 – 10000	52.2%
>10000	47.6%

Tab. 3.12 Dimensional distribution of the bubbles, cavitator M4, 4 atm.

Increasing the pressure to 4.5 atm, an even more relevant increase of the number of nano-bubbles was detected, as shown in Fig. 3.15 and Tab. 3.12.

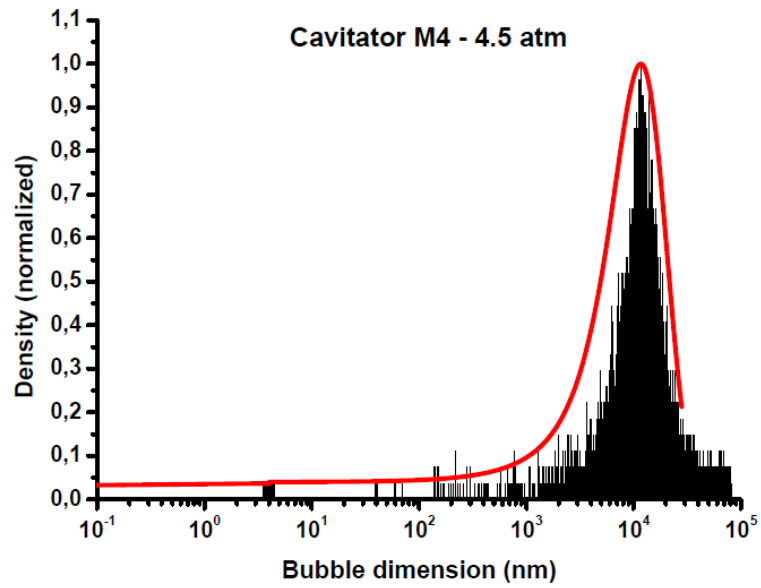


Fig. 3.15 Dimensional distribution of the bubbles, cavitator M4, 4.5 atm.

CAVITATOR M4	
Pressure: 4.5 atm	
Bubble dimension (nm)	Quantity
0.1 – 1	0.001%
1 – 10	0.02%
10 – 100	0.17%
100 – 1000	0.27%
1000 – 10000	19.53%
>10000	80.03%

Tab. 3.13 Dimensional distribution of the bubbles, cavitator M4, 4.5 atm.

A further slight increase in the population of nano-bubbles was noticed for the test at 5 atmospheres, as portrayed in Fig. 3.16 and Tab. 3.14.

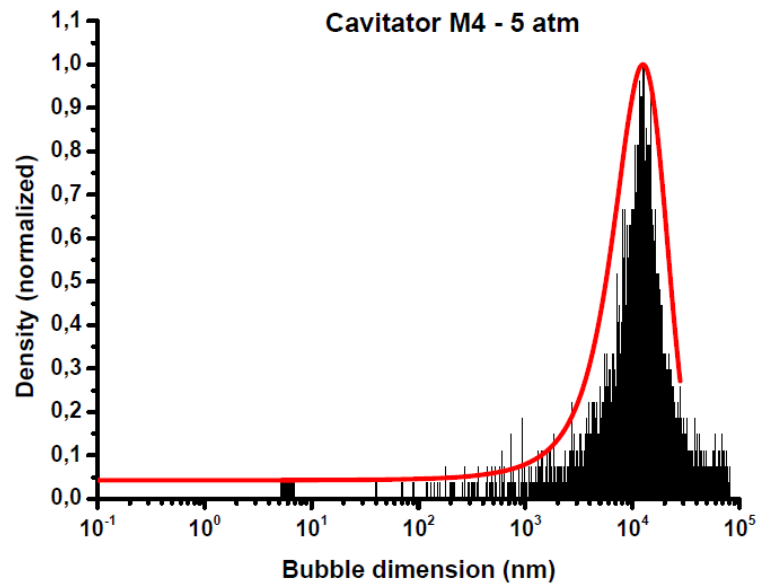


Fig. 3.16 Dimensional distribution of the bubbles, cavitor M4, 5 atm.

CAVITATOR M4	
Pressure: 5 atm	
Bubble dimension (nm)	Quantity
0.1 – 1	0.003%
1 – 10	0.03%
10 – 100	0.3%
100 – 1000	0.35%
1000 – 10000	20%
>10000	79%

Tab. 3.14 Dimensional distribution of the bubbles, cavitor M4, 5 atm.

Finally, after the test at 6 atmospheres, a light decrease of the percentage of the nano-bubbles has been observed (Fig. 3.17 and Tab. 3.15).

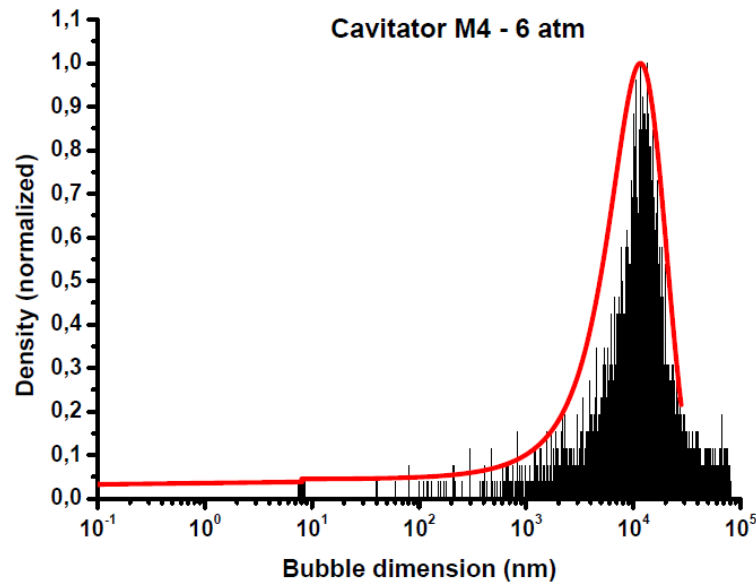


Fig. 3.17 Dimensional distribution of the bubbles, cavitator M4, 6 atm.

CAVITATOR M4	
Pressure: 6 atm	
Bubble dimension (nm)	Quantity
0.1 – 1	0.002%
1 – 10	0.02%
10 – 100	0.23%
100 – 1000	0.43%
1000 – 10000	20.54%
>10000	78.91%

Tab. 3.15 Dimensional distribution of the bubbles, cavitator M4, 6 atm.

As a final remark for the section about the optic surveys on the plant, it is possible to notice that, for cavitator M4, the tests at 4.5, 5 and 6 atmospheres showed an almost constant bubble populations in the diameter field of 0.1-10 nm while a more substantial variability was found between the effects of these pressures for the cavitators M2 and M5.

3.3 Evaluation of the energy per imploded nano-bubble

In order to evaluate from the theoretical point of view whether the implosion of nano-bubbles produced by cavitation was the real cause of the promotion of piezonuclear reactions in the water

solution, a paramount importance had the calculation of the energy per imploded nano-bubble for the cavitators optically tested by PDA. This evaluation was accomplished for each cavitator by considering the optimal working pressure of the plant layout, therefore the pressure producing the larger amount of nano-bubbles. The nano-bubbles were considered as having diameters included between 0.1 and 10 nanometres. The optimal working pressures in terms of number of nano-bubbles produced were found to be 4.5 atm for cavitator M2, 5 atm for cavitator M5 and 5 atm for cavitator M4.

The total number of bubbles (both of nanometric and of greater dimensions) produced per hour on the final section of the cavitator was taken into account. This estimate needed a double extension, both in time and in space, of the results given by PDA. Considering time, it was necessary, at first, to extend the results in terms of number of bubbles from the default maximum monitoring time of PDA, 100 seconds (maximum time allowed by the instrument setting to get the reference number of 20.000 bubbles of all dimensions) to the desired period of 1 hour. Considering space, it was needed, then, to extend the results obtained on the monitoring area considered by PDA, equal to 0.125 mm^2 , to the whole section of the cavitator, in the cases of nozzles M2, M5 and M4 equal about to 5.726 mm^2 . The spatial extension of the results was done by referring to the following simple expression:

$$n_{b \text{ on area of cavitator in } 1 \text{ h}} = \frac{A_{\text{cavitator}}}{A_{\text{PDA}}} \cdot n_{b \text{ on monitoring area of PDA in } 1 \text{ h}} \quad (3.1)$$

Once these two calculations had been accomplished, the total number of bubbles of every dimension per hour on the section of the cavitator was found. From this value, the number of nano-bubbles per hour was possible to be evaluated by simply multiplying it by the nano-bubble percentage at the optimal working pressure for each cavitator. Therefore, the energy per imploded nano-bubble was obtained by dividing the total thermal energy released at the optimal working pressure by the number of nano-bubbles per hour. The results of these assessments are shown in the following.

For the cavitator M2 the following quantities have been evaluated:

- Bubbles produced in one hour: 183.200.000
- Nano-bubbles produced in one hour: 3.874.200 (0.021%)
- Thermal energy released at optimal pressure: 139 kJ
- Thermal energy per imploded nano-bubble: 36.13 mJ

For the cavitator M5 the next values have been got:

- Bubbles produced in one hour: 412.200.000

- Nano-bubbles produced in one hour: 4.946.400 (0.012%)
- Thermal energy released at optimal pressure: 171 kJ
- Thermal energy per imploded nano-bubble: 34.57 mJ

For cavitator M6, finally, the results below have been obtained:

- Bubbles produced in one hour: 219.840.000
- Nano-bubbles produced in one hour: 7.254.720 (0.033%)
- Thermal energy released at optimal pressure: 237 kJ
- Thermal energy per imploded nano-bubble: 32.67 mJ

By analysing the previous evaluations, a very relevant outcome has to be pointed out: despite the number of bubbles and nano-bubbles produced showed large variations between the different cavitators, as well as the thermal energy released, the energy per imploded nano-bubble was found to be almost constant for the three cases, with a variation from the mean value enclosed in the range $\pm 5\%$. The substantial consistency of this fundamental parameter is clearly underlined by the graph in Fig. 3.18, which represents the previous values and, in grey, the error band with largeness 5% per side.

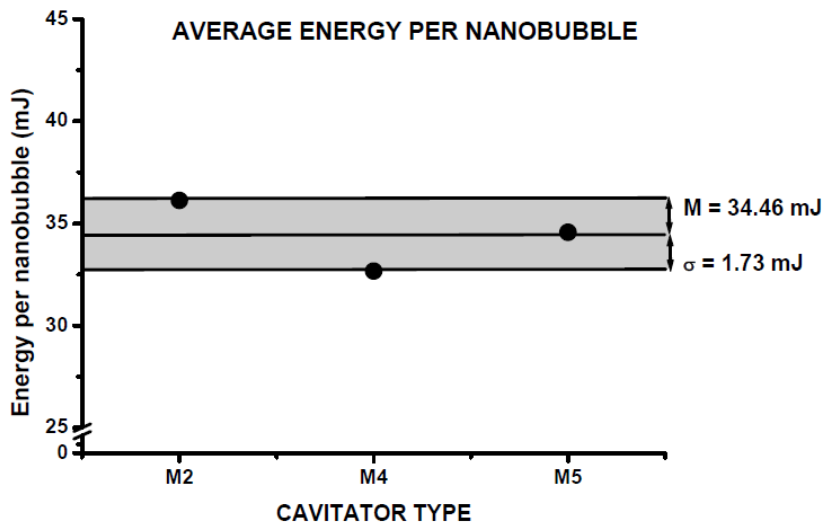


Fig. 3.18 Energy per imploded nano-bubble of cavitators M2, M4, M5.

The importance of the consistency of the released thermal energy per nano-bubble can be explained considering that, since it is the only parameter which does not significantly change between the three test, while all the other measured ones show great variations, it is a clear evidence of the fact that the extra-heat generations in the water solution are caused really by the implosion of the nano-bubbles themselves and not by other causes or factors. Just the implosion of nano-bubbles, then, is able to produce the low energy nuclear reactions and positive thermal variations observed in the fluid enriched with iron salts, causing phonons at TeraHertz frequencies. This outcome can

exclude for example the effect of bubbles of greater dimensions, since all the other physical parameters change, while the energy released by the implosion of nano-bubbles behaves as a physical constant. This evidence has encouraged to focus mainly on the improvement of the nozzles to enlarge the field and the population of the bubbles of nanometric dimensions (0.1-10 nm) and then to try to get more relevant energy productions and efficiencies.

Chapter 4

Calorimetric experimental results: direct method for COP evaluation

4.1 Overcoming of the indirect method and direct evaluation of COP for cavitators NB and NM

The analysis of the results in terms of Coefficients Of Performance obtained from the tests on the insulated cavitation reactor for both the first and the second generation of brass cavitators led to reveal some vulnerabilities of the indirect method of assessment of the COP adopted in the first phase of the calorimetric experimentation. Indeed, as previously outlined in Chapter 2, the indirect method of evaluation of the COP still in transient phase by means of the polynomial extrapolation and the application of the least square method for assessment of the steady-state temperatures revealed some numerical instability problems which affected the estimation. Despite the indirect method used in the first phase of the experimentation was still considered as an adequate first-phase assessment technique, in the second phase of the experimental campaign it was decided to research new estimation techniques for the COP of the insulated plant, that would have been able to nearer to a direct evaluation.

In order to try to overcome the problems revealed by the indirect assessment method tested for the insulated cavitation reactor in the steady-state condition, it was planned a series of attempts at reduced velocity of the pump, to gradually nearer to the steady-state condition for the optimal value of 500rpm.

The internal convection heat transfer coefficients adopted for cavitator NB, together with the relative Rayleigh and Nusselt numbers are reported in Tab. 4.1.

Cavitator NB	
Test at the velocity of 300 rpm	
$Ra (-)$	13948.56
$Nu (-)$	944.48
$h_i \left(\frac{W}{m^2K} \right)$	48852.44
Test at the velocity of 350 rpm	
$Ra (-)$	15818.90
$Nu (-)$	1071.12

$h_i \left(\frac{W}{m^2K} \right)$	55403.01
Test at the velocity of 400 rpm	
$Ra (-)$	17705.71
$Nu (-)$	1198.88
$h_i \left(\frac{W}{m^2K} \right)$	62011.23
Test at the velocity of 450 rpm	
$Ra (-)$	19994.98
$Nu (-)$	1353.89
$h_i \left(\frac{W}{m^2K} \right)$	70029.01
Tests at the velocity of 500 rpm	
$Ra (-)$	22117.05
$Nu (-)$	1497.58
$h_i \left(\frac{W}{m^2K} \right)$	77461.18

Tab. 4.1 Rayleigh and Nusselt numbers, internal convection heat transfer coefficient, cavitator NB.

A first test at the pump turning velocity of 350 rpm for the insulated reactor equipped by cavitator NB (having 2.7mm of final diameter) allowed to measure the temperature and electric power supply curves which are shown in Figs. 4.1-4.2. Since the steady-state condition was reached, the actual measurement of the physical parameters in the thermal equilibrium phase was possible to be fulfilled, according to the defined “direct method” for the evaluation of COP.

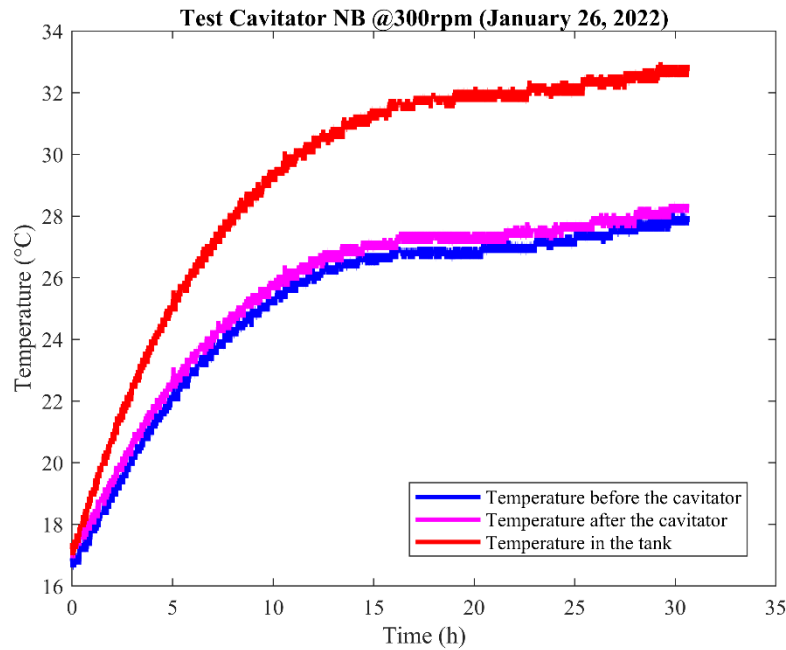


Fig. 4.1 Temperature trends from the test of the 26th of January 2022, cavitator NB, 300 rpm.

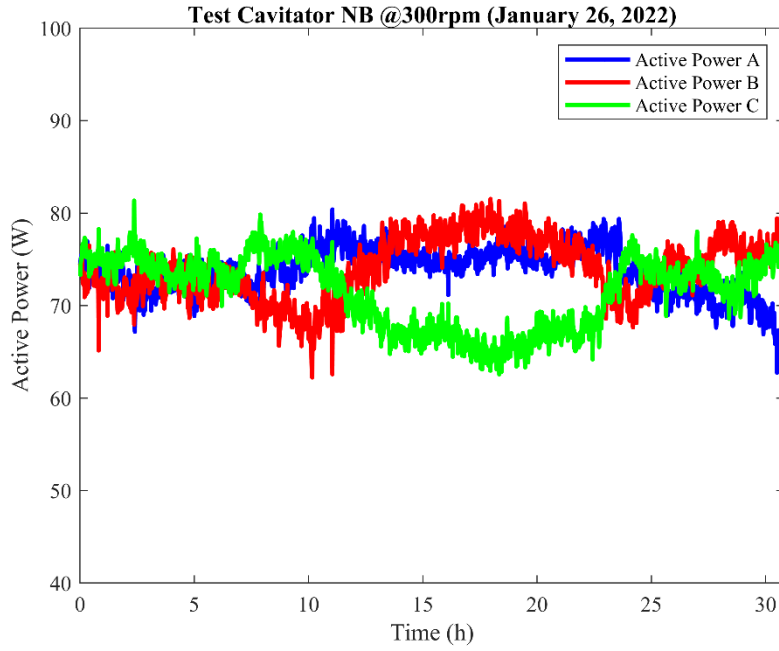


Fig. 4.2 Electric powers provided to the three-phase pump from the test of the 26th of January 2022, cavitator NB, 300 rpm.

The following physical parameters were measured:

- mass of the water solution 25 kg;
- initial (environmental) temperature 17.2°C;
- steady-state temperature before the cavitator 27.2°C;
- steady-state temperature after the cavitator 27.6°C;
- steady-state temperature in the tank 32.1°C;
- pressure drop in the cavitator 3.77 bar;
- electric power provided to the pump 219.37 W;
- pump rotation velocity 300 rpm;
- steady-state flow rate of the plant 0.00762 m³/minute;

The energy terms of the balance in steady-state conditions were evaluated as follows:

- Input electric energy absorbed by the pump $E_{in} = 789.7$ kJ
- Thermal energy stored by the water $E_w = 512.8$ kJ
- Thermal energy dispersed in the environment $E_{disp} = 115.7$ kJ
- Mechanical energy dissipated by the cavitator $E_{mec} = 172.3$ kJ

The Coefficient of Performance of insulated plant was thus calculated according to the direct method:

$$\text{COP} = \frac{E_{out}}{E_{in}} = \frac{800.8 \text{ kJ}}{789.7 \text{ kJ}} = 1.01 \quad (4.1)$$

Another test was then performed by increasing the turning velocity of the pump of 50rpm to a value of 350 rpm. The results in terms of calorimetric and electric power absorption paths are shown in Figs. 4.3-4.4.

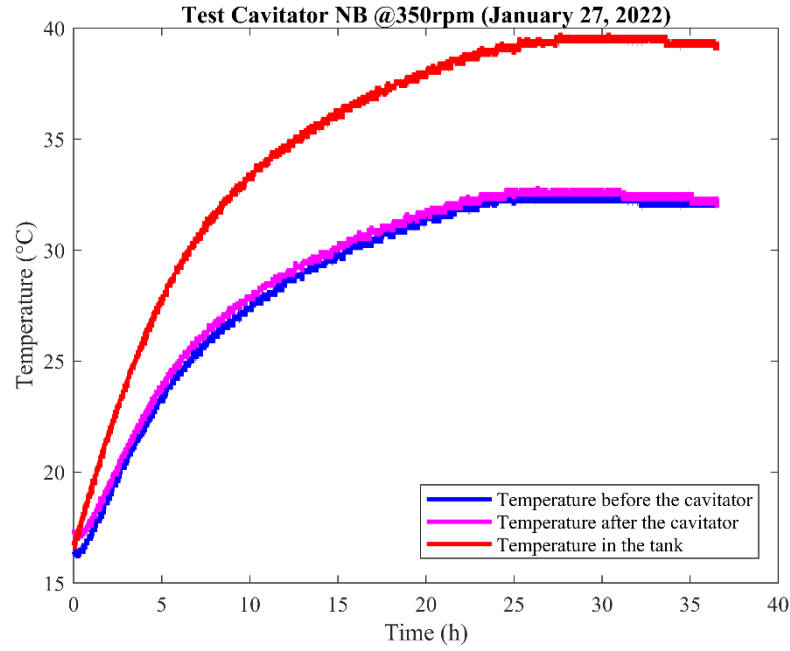


Fig. 4.3 Temperature trends from the test of the 27th of January 2022, cavitator NB, 350 rpm.

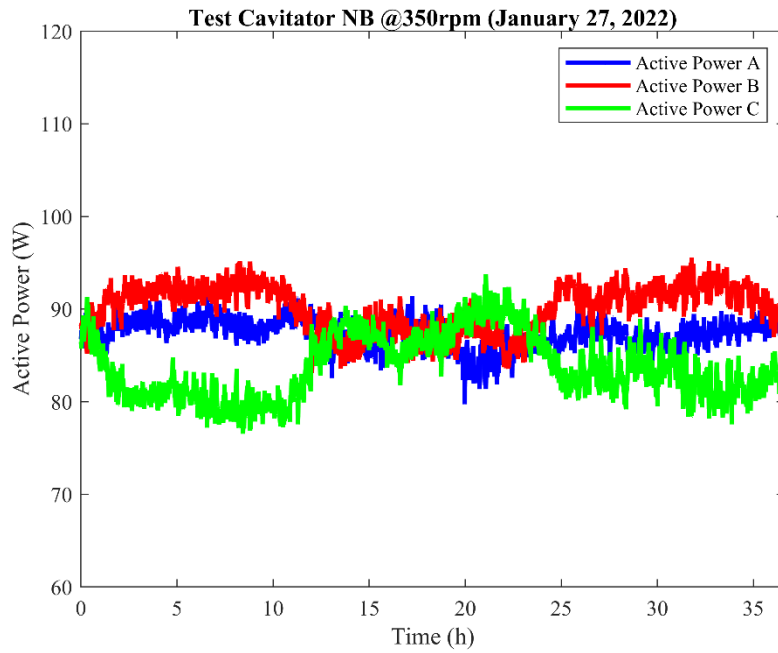


Fig. 4.4 Electric powers provided to the three-phase pump from the test of the 27th of January 2022, cavitator NB, 350 rpm.

The physical quantities describing the thermal equilibrium state are reported in the following list:

- mass of the water solution 25 kg;
- initial (environmental) temperature 16.7°C;
- steady-state temperature before the cavitator 32.2°C;
- steady-state temperature after the cavitator 32.5°C;
- steady-state temperature in the tank 39.5°C;
- pressure drop in the cavitator 5.48 bar;
- electric power provided to the pump 261.24 W;
- pump rotation velocity 350 rpm;
- steady-state flow rate of the plant 0.00865 m³/minute;

The energy input and output contributions were thus calculated:

- Input electric energy absorbed by the pump $E_{in} = 940.5 \text{ kJ}$
- Thermal energy stored by the water $E_w = 763.9 \text{ kJ}$
- Thermal energy dispersed in the environment $E_{disp} = 176.9 \text{ kJ}$
- Mechanical energy dissipated by the cavitator $E_{mec} = 284.3 \text{ kJ}$

The Coefficient of Performance of insulated plant was in this case:

$$\text{COP} = \frac{E_{out}}{E_{in}} = \frac{1225.1 \text{ kJ}}{940.5 \text{ kJ}} = 1.30 \quad (4.2)$$

A further increase of the pump turning velocity up to the value of 400rpm made possible to register the temperature and electric power supply trends of Figs. 4.5-4.6.

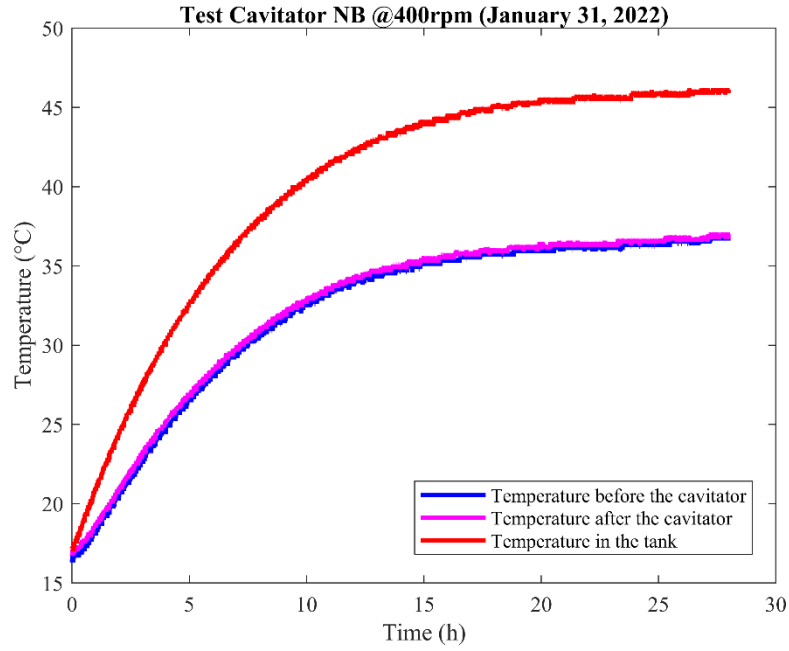


Fig. 4.5 Temperature trends from the test of the 31st of January 2022, cavitator NB, 400 rpm.

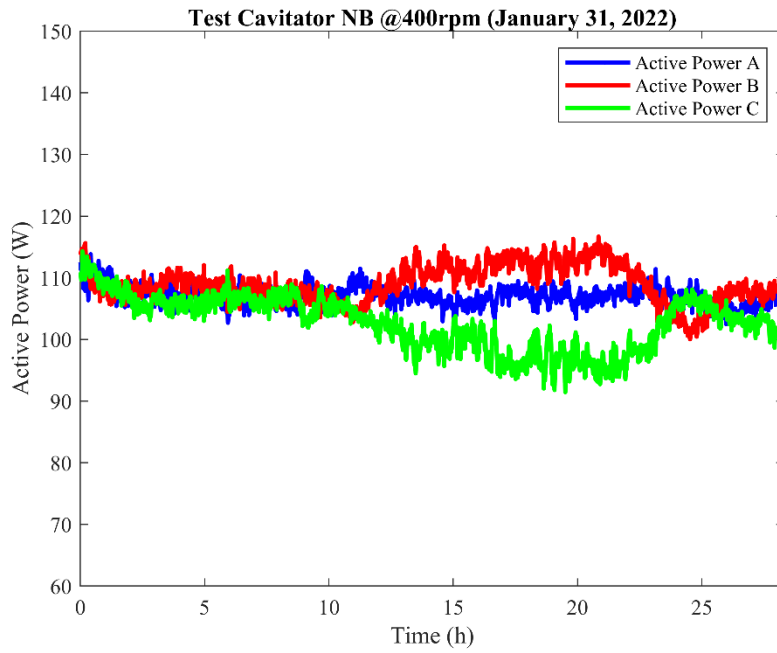


Fig. 4.6 Electric powers provided to the three-phase pump from the test of the 31st of January 2022, cavitator NB, 400 rpm.

The ensuing physical parameters of the test were considered:

- mass of the water solution 25 kg;
- initial (environmental) temperature 17.2°C;
- steady-state temperature before the cavitator 36.7°C;
- steady-state temperature after the cavitator 36.8°C;

- steady-state temperature in the tank 46.0°C;
- pressure drop in the cavitator 7.28 bar;
- electric power provided to the pump 318.72 W;
- pump rotation velocity 400 rpm;
- steady-state flow rate of the plant 0.00968 m³/minute;

The energy terms were then evaluated as follows:

- Input electric energy absorbed by the pump $E_{in} = 1147.4$ kJ
- Thermal energy stored by the water $E_w = 973.2$ kJ
- Thermal energy dispersed in the environment $E_{disp} = 223.1$ kJ
- Mechanical energy dissipated by the cavitator $E_{mec} = 422.9$ kJ

Therefore, the Coefficient of Performance was evaluated at the following value, according to the direct method:

$$COP = \frac{E_{out}}{E_{in}} = \frac{1619.2 \text{ kJ}}{1147.4 \text{ kJ}} = 1.41 \quad (4.3)$$

The fourth attempt at reduced velocity was then performed at a level of 450 rpm, just 50rpm below the estimate optimal value of 500rpm. Under this condition, the graphs of Figs. 4.7-4.8 were obtained.

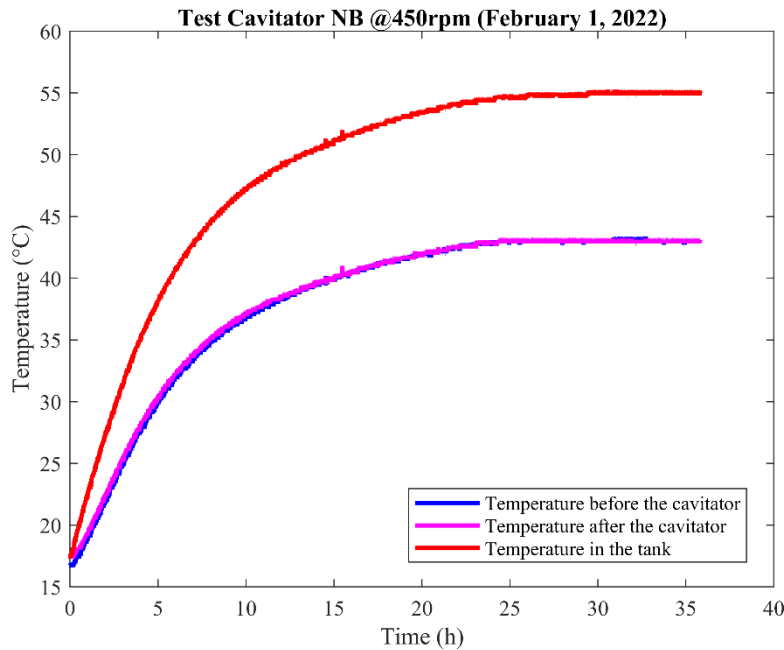


Fig. 4.7 Temperature trends from the test of the 1st of February 2022, cavitator NB, 450rpm.

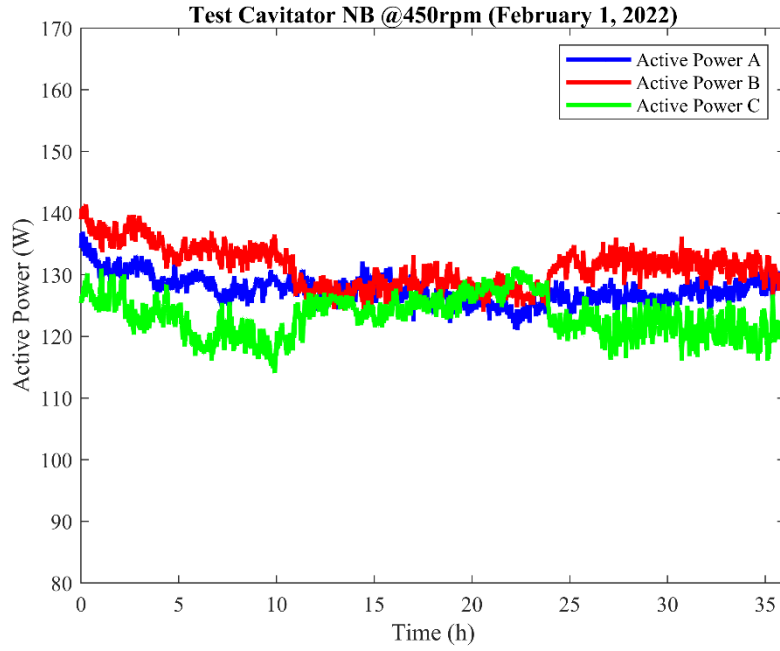


Fig. 4.8 Electric powers provided to the three-phase pump from the test of the 1st of February 2022, cavitator NB, 450rpm.

With reference to the steady-state condition of the insulated cavitation reactor, the next data were collected:

- mass of the water solution 25 kg;
- initial (environmental) temperature 17.4°C;
- steady-state temperature before the cavitator 43.0°C;
- steady-state temperature after the cavitator 43.0°C;
- steady-state temperature in the tank 55.0°C;
- pressure drop in the cavitator 9.10 bar;
- electric power provided to the pump 382.00 W;
- pump rotation velocity 450 rpm;
- steady-state flow rate of the plant 0.01087 m³/minute;

The energy terms were then calculated as follows:

- Input electric energy absorbed by the pump $E_{in} = 1375.2$ kJ
- Thermal energy stored by the water $E_w = 1255.8$ kJ
- Thermal energy dispersed in the environment $E_{disp} = 292.3$ kJ
- Mechanical energy dissipated by the cavitator $E_{mec} = 596.8$ kJ

The following COP was finally evaluated:

$$\text{COP} = \frac{E_{out}}{E_{in}} = \frac{2144.9 \text{ kJ}}{1375.2 \text{ kJ}} = 1.56 \quad (4.4)$$

On the bases of the tests at reduced velocity performed, it was possible to notice that the steady-state temperature in the tank increased almost according to a linear law as function of the pump turning velocity (Fig. 4.9), as well as the temperature measured before and after the cavitator section and the flow rate of the plant. In the original purpose, the observation of the good representativity of the linear regression on the previously declared parameters would have been able to provide a reliable assessment method for the COP in steady-state condition at the pump optimal working velocity.

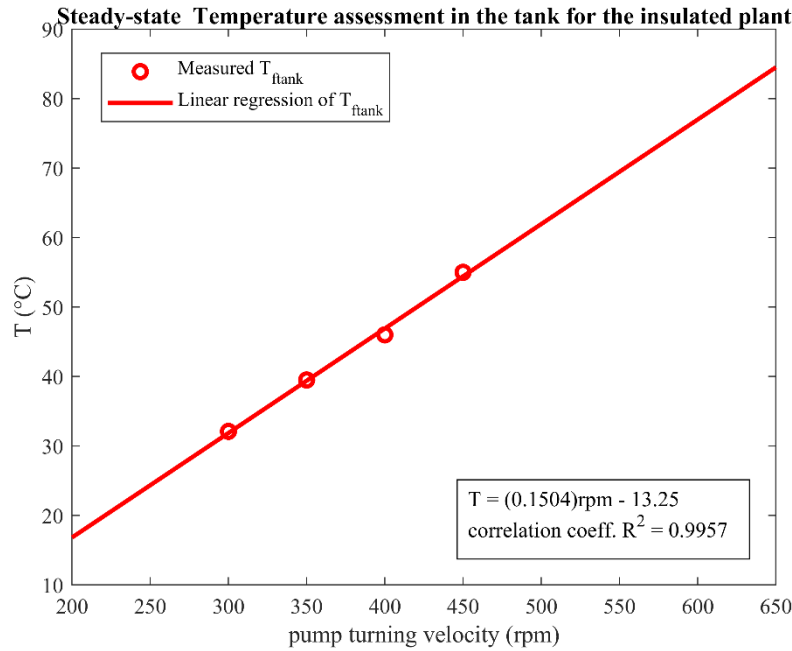


Fig. 4.9 Measured values of steady-state tank temperature as function of the pump turning velocity and linear regression, cavitator NB.

Actually, after having accomplished the test on the insulated plant at 450 rpm, it was decided to try a direct evaluation of the COP by taking the plant to the thermal equilibrium condition at 500 rpm. The decision was justified by the proximity of the previous velocity condition to the optimal one and by the lack of watertightness problems which had been observed until a tank temperature of about 55°C. The linear extrapolation of Fig. 4.9 allowed to estimate a maximum temperature of about 60°C for the optimum velocity of 500 rpm, which was considered to be bearable by the plant.

The temperature and electric power absorption trends registered during the first test on the insulated plant at the velocity of 500 rpm are depicted in Figs. 4.10-4.11.

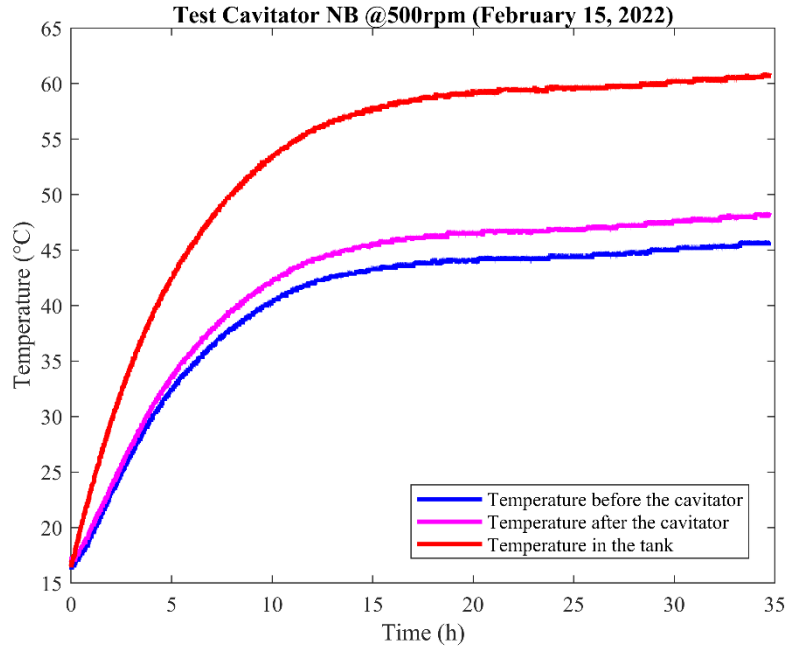


Fig. 4.10 Temperature trends from the test of the 15th of February 2022, cavitator NB, 500rpm.

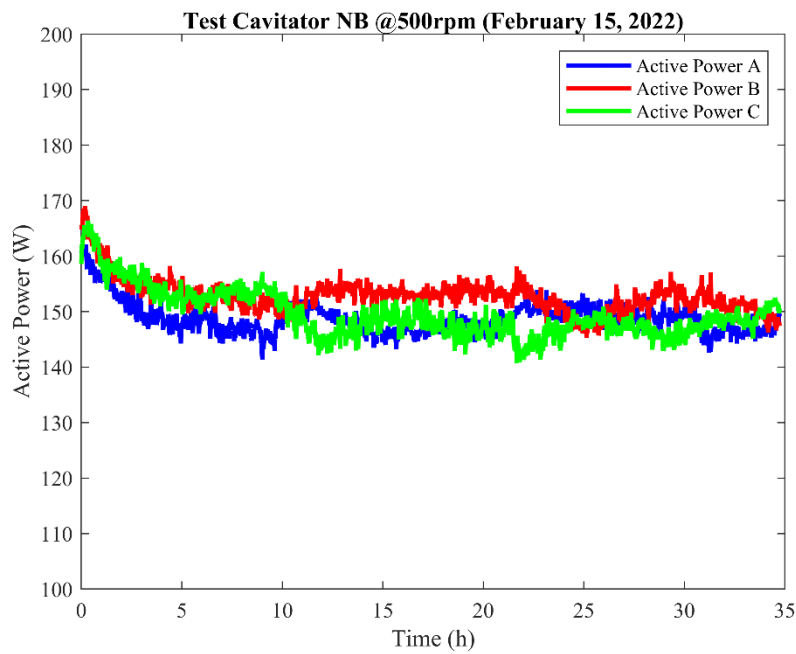


Fig. 4.11 Electric powers provided to the three-phase pump from the test of the 15th of February 2022, cavitator NB, 500rpm.

The following physical parameters were measured during the test:

- mass of the water solution 25 kg;
- initial (environmental) temperature 16.7°C;
- steady-state temperature before the cavitator 44.9°C;
- steady-state temperature before the cavitator 47.3°C;

- steady-state temperature in the tank 60.0°C;
- pressure drop in the cavitator 10.57 bar;
- electric power provided to the pump 451.07 W;
- pump rotation velocity 500 rpm;
- steady-state flow rate of the plant 0.01209 m³/minute;

According to the direct method, the energy contributions were evaluated as follows:

- Input electric energy absorbed by the pump $E_{in} = 1623.9 \text{ kJ}$
- Thermal energy stored by the water $E_w = 1580.2 \text{ kJ}$
- Thermal energy dispersed in the environment $E_{disp} = 332.2 \text{ kJ}$
- Mechanical energy dissipated by the cavitator $E_{mec} = 766.8 \text{ kJ}$

Therefore, the COP was found to assume the ensuing value:

$$\text{COP} = \frac{E_{out}}{E_{in}} = \frac{2679.2 \text{ kJ}}{1623.9 \text{ kJ}} = 1.65 \quad (4.5)$$

The slight increase of efficiency that can be underlined between the insulated tests at 450rpm and 500rpm is an indicator of the proximity to the optimum pump turning velocity of the second of these two values, similarly to what was observed for the non-insulated conditions of the reactor.

Despite the second indirect method of assessment for the COP in insulated conditions had been overcome by the direct evaluation of the coefficient in the steady-state condition, it is worth noting that the hypothesis of the linearity of the tank temperatures as a function of the pump turning velocity had a further confirmation from the test of the 15th of February 2022 (Fig. 4.12).

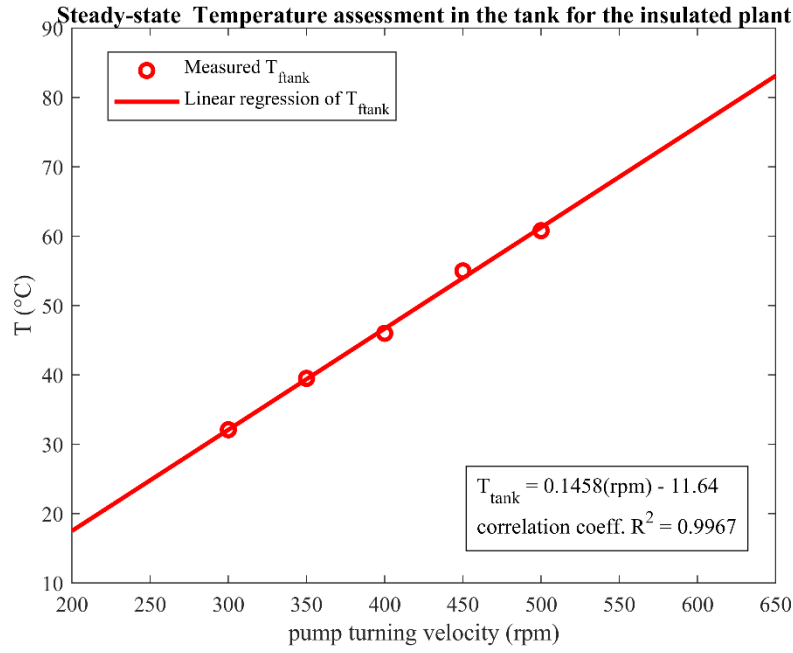


Fig. 4.12 Measured values of steady-state tank temperature as function of the pump turning velocity and linear regression over five tests, cavitator NB.

The results of the second test on the insulated plant equipped by cavitator NB in terms of temperature and electric power absorption paths are portrayed in Fig. 4.13-4.14.

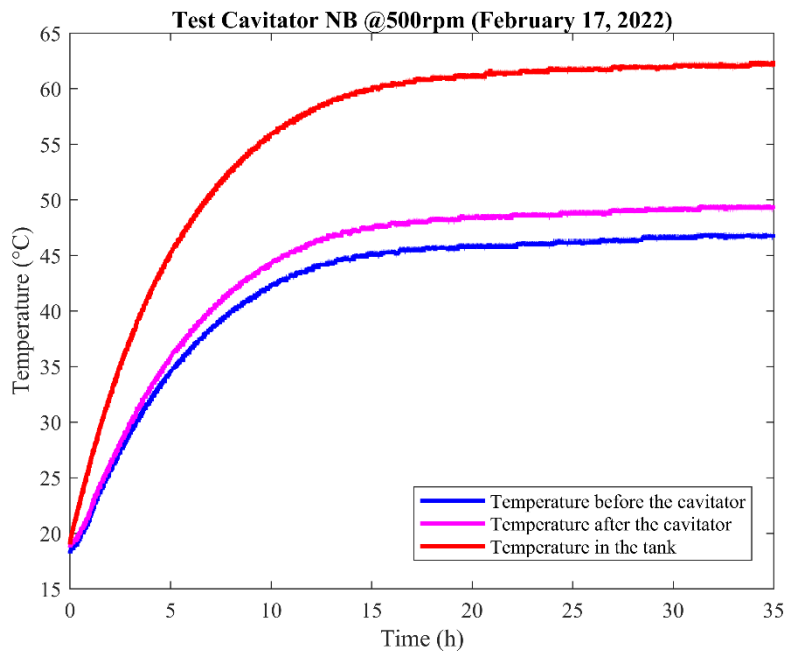


Fig. 4.13 Temperature trends from the test of the 17th of February 2022, cavitator NB, 500rpm.

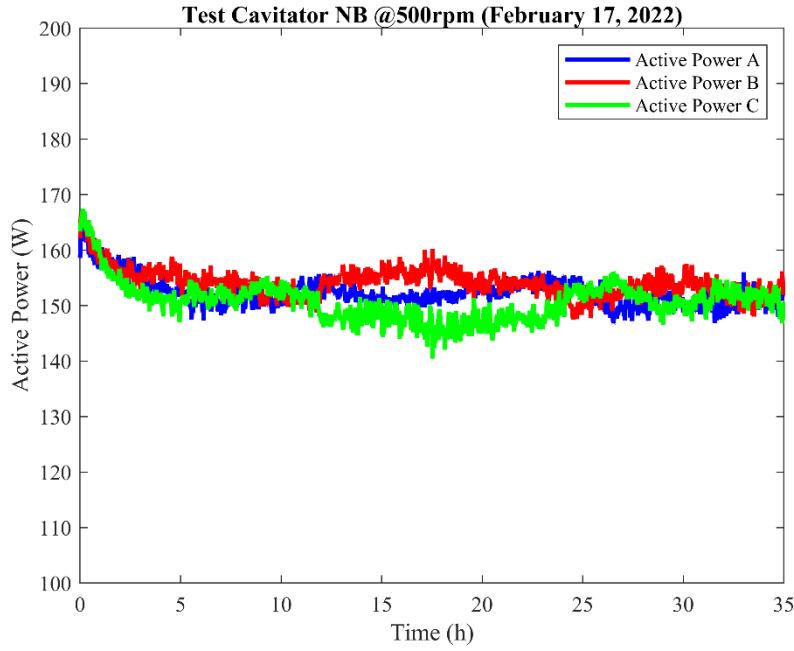


Fig. 4.14 Electric powers provided to the three-phase pump from the test of the 17th of February 2022, cavitator NB, 500 rpm.

The ensuing physical parameters were registered:

- mass of the water solution 25 kg;
- initial (environmental) temperature 19.0°C;
- steady-state temperature before the cavitator 46.4°C;
- steady-state temperature after the cavitator 49.0°C;
- steady-state temperature in the tank 61.9°C;
- pressure drop in the cavitator 10.75 bar;
- electric power provided to the pump 457.06 W;
- pump rotation velocity 500 rpm;
- steady-state flow rate of the plant 0.01209 m³/minute;

The energy terms evaluated according to the direct method are reported in the following:

- Input electric energy absorbed by the pump $E_{in} = 1645.4 \text{ kJ}$
- Thermal energy stored by the water $E_w = 1622.1 \text{ kJ}$
- Thermal energy dispersed in the environment $E_{disp} = 316.6 \text{ kJ}$
- Mechanical energy dissipated by the cavitator $E_{mec} = 779.5 \text{ kJ}$

The next COP was thus evaluated:

$$\text{COP} = \frac{E_{out}}{E_{in}} = \frac{2718.2 \text{ kJ}}{1645.4 \text{ kJ}} = 1.65 \quad (4.6)$$

The third test on the insulated cavitation reactor equipped by cavitator NB allowed to register the temperature trends and electric power absorptions reported in Figs. 4.15-4.16.

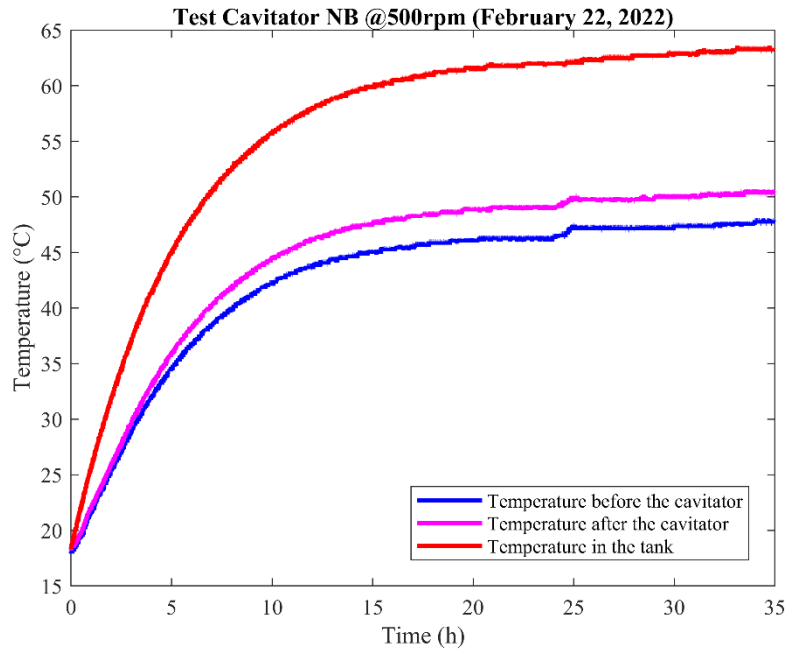


Fig. 4.15 Temperature trends from the test of the 22nd of February 2022, cavitator NB, 500 rpm.

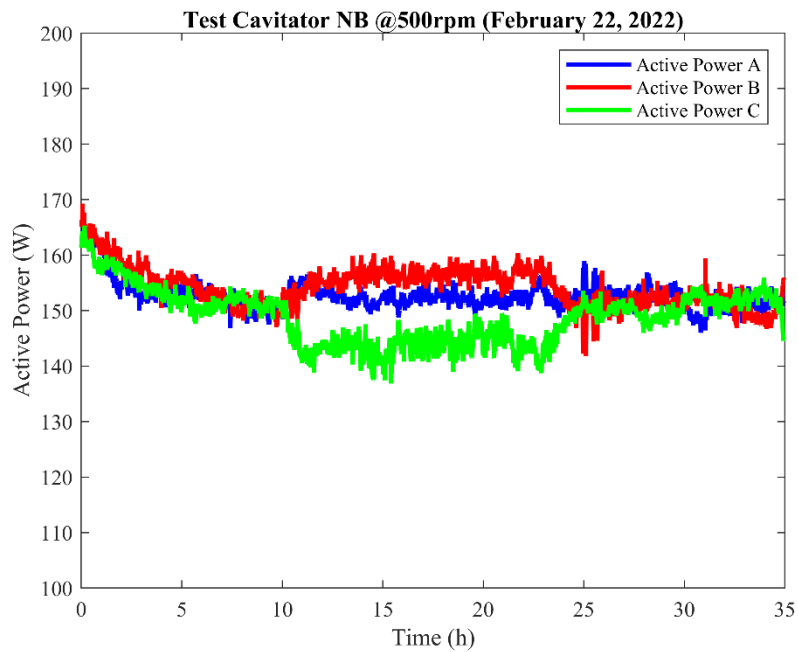


Fig. 4.16 Electric powers provided to the three-phase pump from the test of the 22nd of February 2022, cavitator NB, 500 rpm.

The following physical data were collected during the test:

- mass of the water solution 25 kg;
- initial (environmental) temperature 18.5°C;
- steady-state temperature before the cavitator 47.1°C;
- steady-state temperature after the cavitator 49.8°C;
- steady-state temperature in the tank 62.6°C;
- pressure drop in the cavitator 10.79 bar;
- electric power provided to the pump 455.66 W;
- pump rotation velocity 500 rpm;
- steady-state flow rate of the plant 0.01209 m³/minute;

The application of the direct method allowed to evaluate the next energy contributions:

- Input electric energy absorbed by the pump $E_{in} = 1640.4$ kJ
- Thermal energy stored by the water $E_w = 1622.1$ kJ
- Thermal energy dispersed in the environment $E_{disp} = 338.1$ kJ
- Mechanical energy dissipated by the cavitator $E_{mec} = 782.3$ kJ

The COP was thus calculated:

$$\text{COP} = \frac{E_{out}}{E_{in}} = \frac{2442.5 \text{ kJ}}{1640.4 \text{ kJ}} = 1.67 \quad (4.7)$$

The fourth and last attempt on the insulated reactor for cavitator NB provided the results in terms of thermal and electric power supply paths that are shown in Figs. 4.17-4.18.

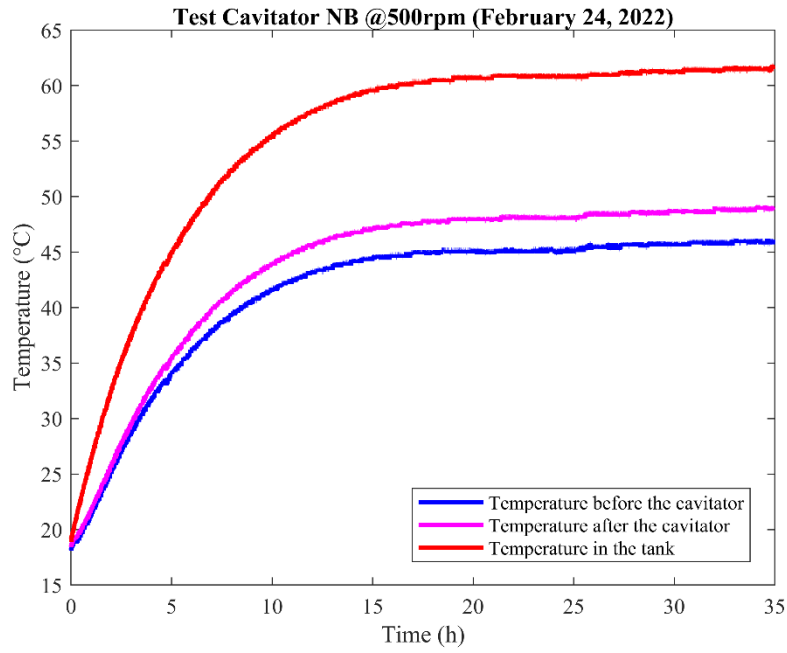


Fig. 4.17 Temperature trends from the test of the 24th of February 2022, cavitator NB, 500 rpm.

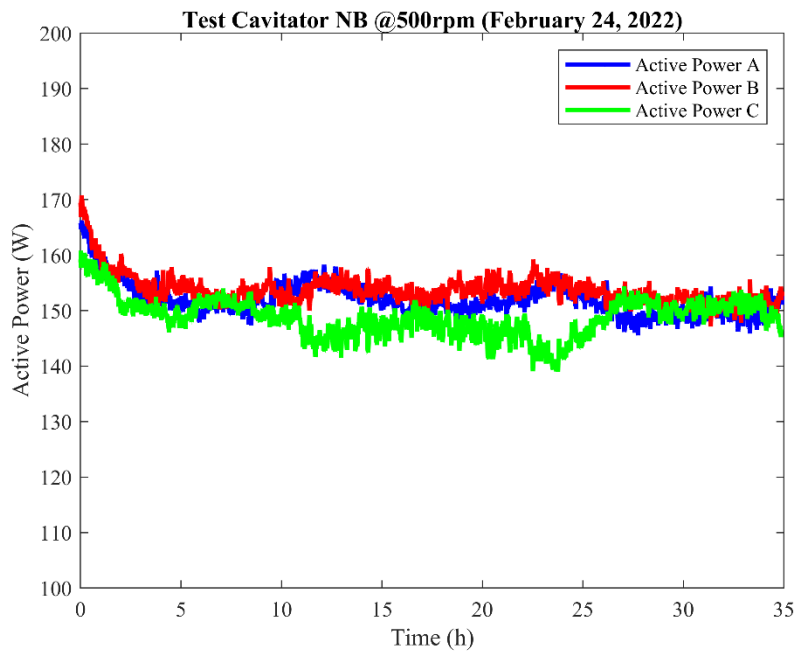


Fig. 4.18 Electric powers provided to the three-phase pump from the test of the 24th of February 2022, cavitator NB, 500 rpm.

The next physical parameters were considered in the calculations:

- mass of the water solution 25 kg;
- initial (environmental) temperature 19.3°C;
- steady-state temperature before the cavitator 45.6°C;
- steady-state temperature after the cavitator 48.5°C;

- steady-state temperature in the tank 61.2°C;
- pressure drop in the cavitator 10.84 bar;
- electric power provided to the pump 454.58 W;
- pump rotation velocity 500 rpm;
- steady-state flow rate of the plant 0.01209 m³/minute;

The energy contributions to the balance assumed then the following values:

- Input electric energy absorbed by the pump $E_{in} = 1636.5$ kJ
- Thermal energy stored by the water $E_w = 1632.5$ kJ
- Thermal energy dispersed in the environment $E_{disp} = 318.3$ kJ
- Mechanical energy dissipated by the cavitator $E_{mec} = 786.4$ kJ

The direct evaluation of COP allowed to obtain the next coefficient:

$$COP = \frac{E_{out}}{E_{in}} = \frac{2737.2 \text{ kJ}}{1636.5 \text{ kJ}} = 1.67 \quad (4.9)$$

Therefore, a comparison between the results obtained by reaching the steady-state condition on the insulated plant according to the direct method and the estimates produced by the indirect method (Paragraph 2.6) is given in Tab. 4.2.

Cavitator NB (2.7mm)	
Indirect method (500 rpm)	Estimated COP
13/12/21	1.49
15/12/21	1.51
17/12/21	1.50
17/01/21	1.29
Average COP	1.45
St. Dev.	0.11
Rel. St. Dev.	7.6%
Direct method (reaching steady state)	Direct evaluation of COP
26/01/22 (300 rpm)	1.01
27/01/22 (350 rpm)	1.30

31/01/22 (400 rpm)	1.41
01/02/22 (450 rpm)	1.56
15/02/22 (500rpm)	1.65
17/02/22 (500 rpm)	1.65
22/02/22 (500 rpm)	1.67
24/02/22 (500 rpm)	1.67
Average evaluated COP (500 rpm)	1.66
St. Dev. (500 rpm)	0.01
Rel. St. Dev. (500 rpm)	0.6%

Tab. 4.2 Comparison between the estimated COP and the effectively measured COP at steady state, cavitator NB.

As it is immediately possible to notice from the table, the assessment method for the COP of the plant in steady-state conditions adopted in the first phases of the calorimetric experimentation resulted to be the cause of an underestimate of the results for the first cavitator of the second generation of brass nozzles of about the 13%. The overcoming of the assessment method and the passage to a direct and more reliable evaluation of the COP constituted one of the more relevant outcomes obtained in the second phase of the laboratory survey activity reported in the present chapter.

Another relevant observation has to be pointed out. At the beginning of Paragraph 2.4 it was declared that from a theoretical point of view the COP evaluated on the non-insulated plant should have been almost coincident with the COP obtained for the insulated reactor, since all the terms of output energy have been considered in the balance. In Tab. 4.3 the comparison between the result of the non-insulated test for cavitator NB reported in Paragraph 2.6 and the results of the insulated tests analysed in the present chapter allow to confirm the original hypothesis and then the consistency of the thermal dispersion evaluation.

Cavitator NB (2.7mm)	
Non-insulated test (500 rpm)	Direct evaluation of COP
01/12/21	1.62
Insulated tests (500 rpm)	Direct evaluation of COP
15/02/22	1.65

17/02/22	1.65
22/02/22	1.67
24/02/22	1.67
Average evaluated COP	1.66

Tab. 4.3 Comparison between the direct evaluations of COP for the non-insulated and the insulated reactor, cavitator NB.

The reduced difference between the average COP of the insulated test and the COP of the non-insulated attempt, of about the 2%, can be intended as the effect of the empirical variability of the monitored tests.

With the aim to perform the direct evaluation of the Coefficients of Performance in thermal equilibrium conditions also for the other cavitators previously tested, a further series of attempts on the insulated cavitation reactor was planned. These new tests were chosen to last for longer periods than the previous insulated attempts analysed in Chapter 2, passing from durations of about 6-10 hours to 30-35 hours, in order to be able to appreciate the stability of the steady-state temperature in the tank.

The internal convection heat transfer coefficient for cavitator NM is reminded in Tab. 4.4.

Cavitator NM	
Tests at the velocity of 250 rpm	
Ra (-)	8199.22
Nu (-)	555.18
h_i ($\frac{W}{m^2K}$)	28716.38

Tab. 4.4 Rayleigh and Nusselt numbers, internal convection heat transfer coefficient, cavitator NM.

A preliminary attempt was accomplished on the non-insulated plant equipped by cavitator NM, characterized by a final diameter of 1.4 mm. The obtained temperature and electric power absorption paths are shown in Figs. 4.19-4.20.

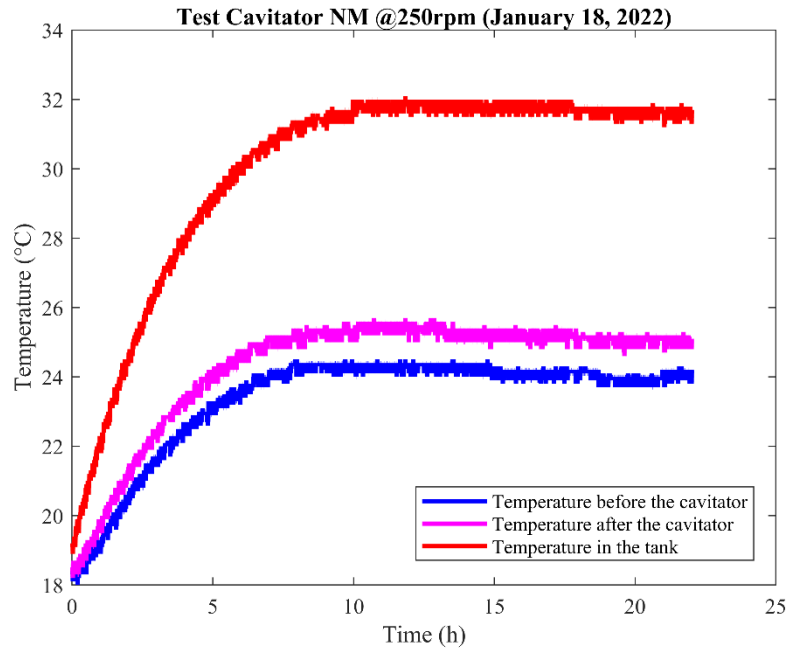


Fig. 4.19 Temperature trends from the test of the 18th of January 2022, cavitator NM, 250rpm.

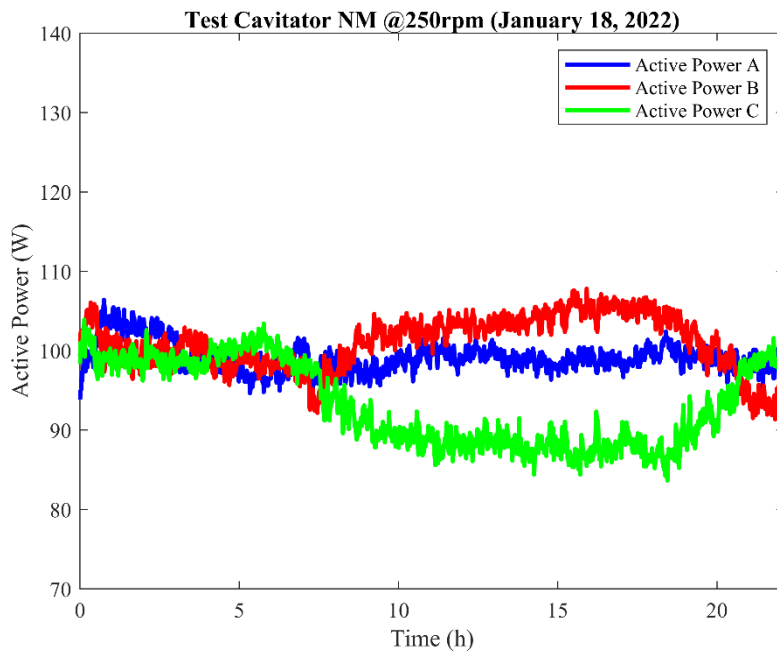


Fig. 4.20 Electric powers provided to the three-phase pump from the test of the 18th of January 2022, cavitator NM, 250rpm.

The next physical parameters were registered:

- mass of the water solution 25 kg;
- initial (environmental) temperature 19.2°C;
- steady-state temperature before the cavitator 24.1°C;
- steady-state temperature after the cavitator 25.1°C;

- steady-state temperature in the tank 31.7°C;
- pressure drop in the cavitator 12.30 bar;
- electric power provided to the pump 293.49 W;
- pump rotation velocity 250 rpm;
- steady-state flow rate of the plant 0.00448 m³/minute;

The energy terms of the balance were evaluated as follows:

- Input electric energy absorbed by the pump $E_{in} = 1056.6 \text{ kJ}$
- Thermal energy stored by the water $E_w = 795.3 \text{ kJ}$
- Thermal energy dispersed in the environment $E_{disp} = 175.0 \text{ kJ}$
- Mechanical energy dissipated by the cavitator $E_{mec} = 330.8 \text{ kJ}$

The Coefficient of Performance of the non-insulated plant was calculated according to the direct method:

$$\text{COP} = \frac{E_{out}}{E_{in}} = \frac{1301.1 \text{ kJ}}{1056.6 \text{ kJ}} = 1.23 \quad (4.10)$$

The first insulated test which reached the steady-state condition for cavitator NM allowed to register the temperature and electric absorption trends of Figs. 4.21-4.22.

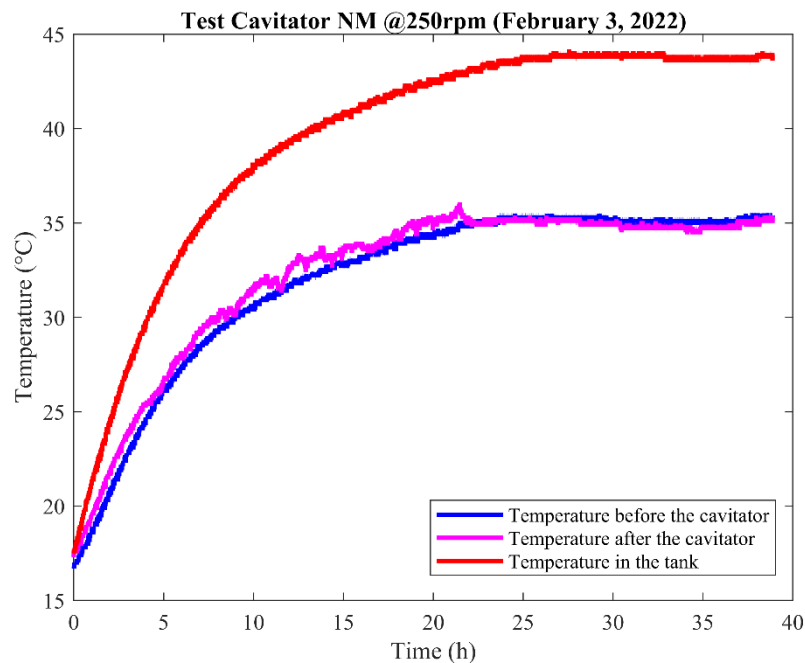


Fig. 4.21 Temperature trends from the test of the 3rd of February 2022, cavitator NM, 250rpm.

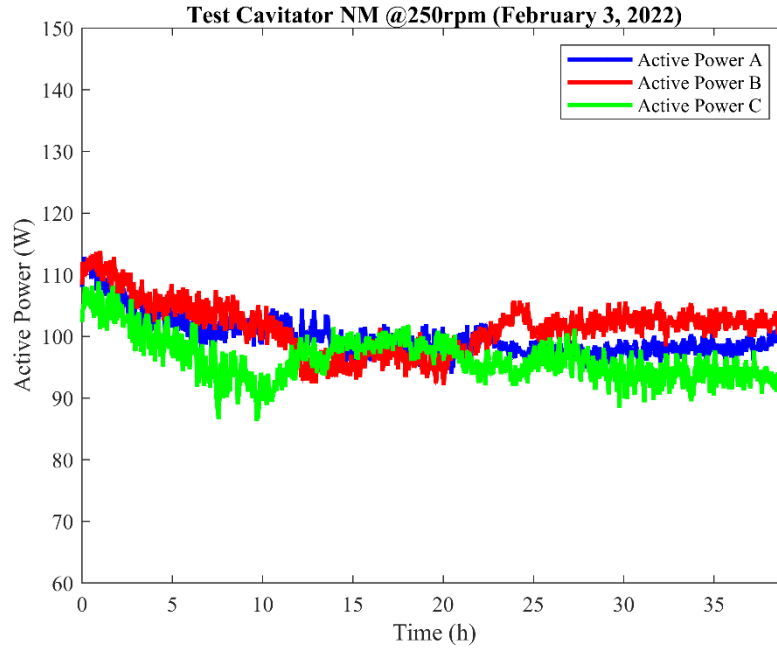


Fig. 4.22 Electric powers provided to the three-phase pump from the test of the 3rd of February 2022, cavitator NM, 250rpm.

During the test, the following physical parameters were measured:

- mass of the water solution 25 kg;
- initial (environmental) temperature 17.5°C;
- steady-state temperature before the cavitator 35.2°C;
- steady-state temperature before the cavitator 34.9°C;
- steady-state temperature in the tank 43.8°C;
- pressure drop in the cavitator 12.71 bar;
- electric power provided to the pump 297.83 W;
- pump rotation velocity 250 rpm;
- steady-state flow rate of the plant 0.00448 m³/minute;

The next energy contributions to the balance were then calculated:

- Input electric energy absorbed by the pump $E_{in} = 1072.2 \text{ kJ}$
- Thermal energy stored by the water $E_w = 900.0 \text{ kJ}$
- Thermal energy dispersed in the environment $E_{disp} = 203.5 \text{ kJ}$
- Mechanical energy dissipated by the cavitator $E_{mec} = 341.7 \text{ kJ}$

The Coefficient of Performance was thus evaluated as follows:

$$\text{COP} = \frac{E_{out}}{E_{in}} = \frac{1445.2 \text{ kJ}}{1072.2 \text{ kJ}} = 1.35 \quad (4.11)$$

The temperatures and electric power supplies to the pump measured during the second test on the insulated plant equipped by cavitator NM are portrayed in Figs. 4.23-4.24.

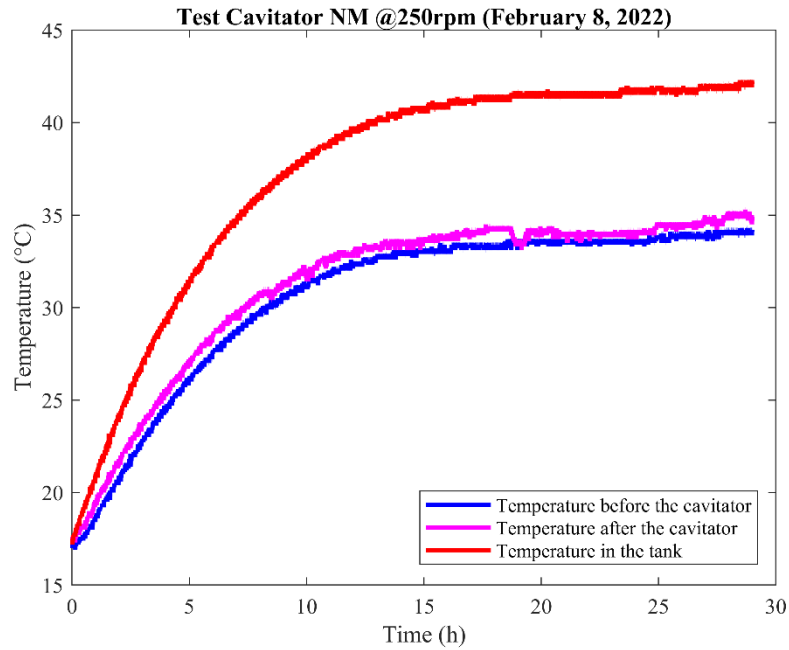


Fig. 4.23 Temperature trends from the test of the 8th of February 2022, cavitator NM, 250rpm.

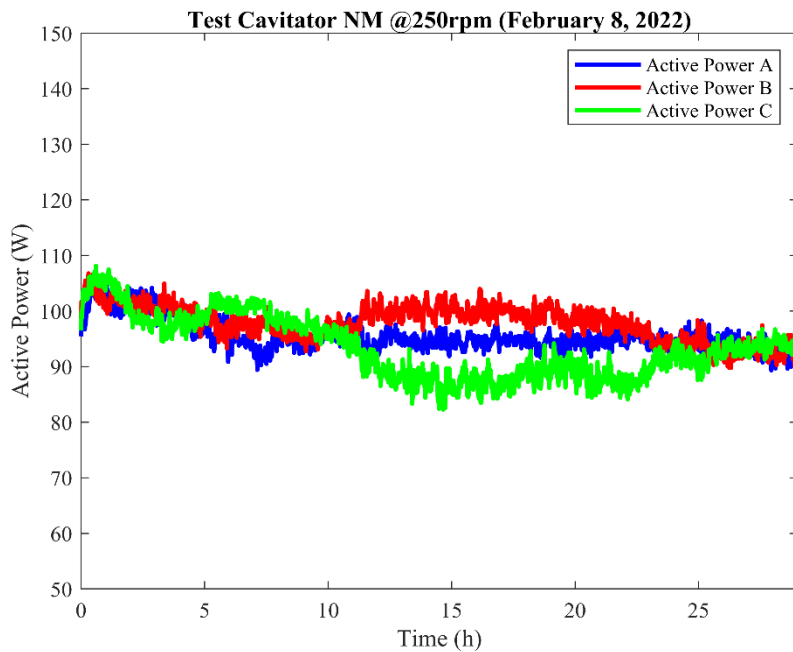


Fig. 4.24 Electric powers provided to the three-phase pump from the test of the 8th of February 2022, cavitator NM, 250rpm.

The ensuing physical quantities were registered:

- mass of the water solution 25 kg;
- initial (environmental) temperature 17.5°C;
- steady-state temperature before the cavitator 33.8°C;
- steady-state temperature after the cavitator 34.3°C;
- steady-state temperature in the tank 41.7°C;
- pressure drop in the cavitator 12.00 bar;
- electric power provided to the pump 286.87 W;
- pump rotation velocity 250 rpm;
- steady-state flow rate of the plant 0.00448 m³/minute;

From the previous data, the next energy terms were evaluated:

- Input electric energy absorbed by the pump $E_{in} = 1032.7 \text{ kJ}$
- Thermal energy stored by the water $E_w = 826.7 \text{ kJ}$
- Thermal energy dispersed in the environment $E_{disp} = 187.9 \text{ kJ}$
- Mechanical energy dissipated by the cavitator $E_{mec} = 322.7 \text{ kJ}$

The Coefficient of Performance in steady-state condition assumed then the following value:

$$\text{COP} = \frac{E_{out}}{E_{in}} = \frac{1337.3 \text{ kJ}}{1032.7 \text{ kJ}} = 1.29 \quad (4.12)$$

During the third test on the insulated plant for cavitator NM, the temperatures and electric power supplies of Figs. 4.25-4.26 were measured.

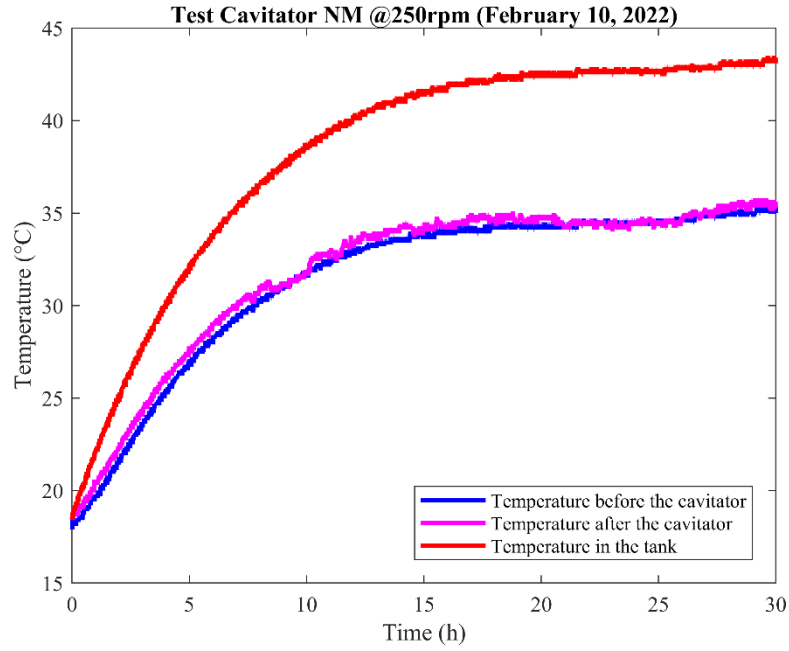


Fig. 4.25 Temperature trends from the test of the 10th of February 2022, cavitator NM, 250rpm.

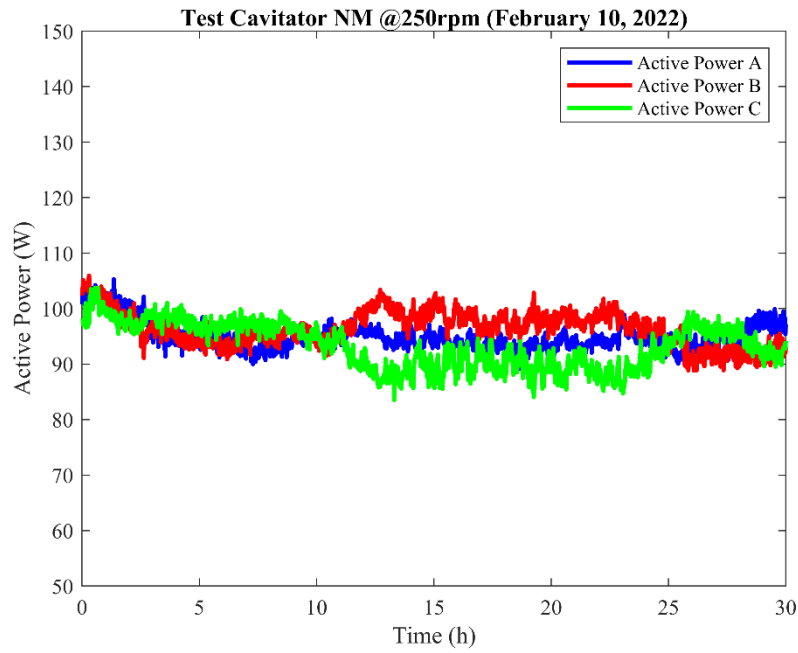


Fig. 4.26 Electric powers provided to the three-phase pump from the test of the 10th of February 2022, cavitator NM, 250rpm.

The test allowed to collect the next physical data:

- mass of the water solution 25 kg;
- initial (environmental) temperature 18.4°C;
- steady-state temperature before the cavitator 34.7°C;
- steady-state temperature after the cavitator 34.8°C;
- steady-state temperature in the tank 42.8°C;

- pressure drop in the cavitator 12.00 bar;
- electric power provided to the pump 284.54 W;
- pump rotation velocity 250 rpm;
- steady-state flow rate of the plant 0.00448 m³/minute;

Therefore, the ensuing energy contributions were calculated:

- Input electric energy absorbed by the pump $E_{in} = 1024.3 \text{ kJ}$
- Thermal energy stored by the water $E_w = 847.7 \text{ kJ}$
- Thermal energy dispersed in the environment $E_{disp} = 188.2 \text{ kJ}$
- Mechanical energy dissipated by the cavitator $E_{mec} = 322.7 \text{ kJ}$

With reference to the thermal equilibrium state of the plant, the COP was then evaluated:

$$\text{COP} = \frac{E_{out}}{E_{in}} = \frac{1358.6 \text{ kJ}}{1024.3 \text{ kJ}} = 1.33 \quad (4.13)$$

The fourth and last attempt on the insulated reactor equipped by cavitator NM allowed to register the temperature and electric power absorption trends portrayed in Figs. 4.27-4.28.

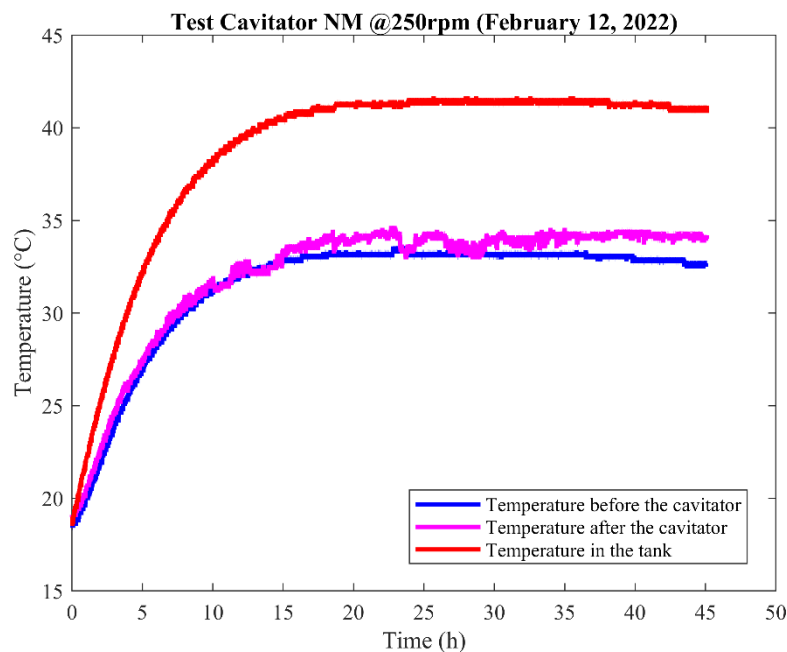


Fig. 4.27 Temperature trends from the test of the 12th of February 2022, cavitator NM, 250rpm.

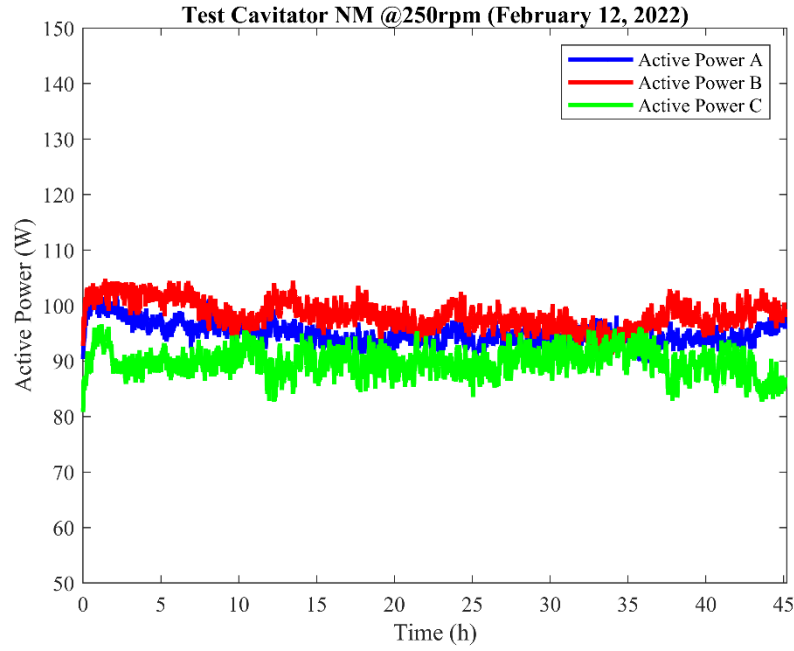


Fig. 4.28 Electric powers provided to the three-phase pump from the test of the 12th of February 2022, cavitor NM, 250rpm.

The following physical parameters of the test were measured:

- mass of the water solution 25 kg;
- initial (environmental) temperature 18.7°C;
- steady-state temperature before the cavitor 33.1°C;
- steady-state temperature after the cavitor 34.1°C;
- steady-state temperature in the tank 41.4°C;
- pressure drop in the cavitor 11.75 bar;
- electric power provided to the pump 283.09 W;
- pump rotation velocity 250 rpm;
- steady-state flow rate of the plant 0.00448 m³/minute;

The energy terms of the balance were thus evaluated as follows:

- | | |
|---|-------------------------------|
| - Input electric energy absorbed by the pump | $E_{in} = 1019.1 \text{ kJ}$ |
| - Thermal energy stored by the water | $E_w = 868.6 \text{ kJ}$ |
| - Thermal energy dispersed in the environment | $E_{disp} = 172.4 \text{ kJ}$ |
| - Mechanical energy dissipated by the cavitor | $E_{mec} = 316.0 \text{ kJ}$ |
| - Energy employed for the by-pass flux | $E_{bp} = 34.0 \text{ kJ}$ |

The COP in steady-state condition was finally calculated:

$$\text{COP} = \frac{E_{out}}{E_{in}} = \frac{1357.0 \text{ kJ}}{1019.1 \text{ kJ}} = 1.33 \quad (4.14)$$

The comparison between the values of COP which were previously estimated by means of the indirect method and the coefficients directly evaluated in steady-state conditions is given in Tab.4.5. As it possible to notice, for cavitator NM the indirect assessment method produced in this case an accurate estimate of the Coefficient of Performance for the insulated reactor.

Cavitator NM (1.4mm)	
Indirect method (250 rpm)	Estimated COP
20/01/22	1.25
21/01/22	1.34
24/01/22	1.38
25/01/22	1.36
Average COP	1.33
St. Dev.	0.06
Rel. St. Dev.	4.5%
Direct method (250 rpm)	Direct evaluation of COP
03/02/22	1.35
08/02/22	1.29
10/02/22	1.33
12/02/22	1.33
Average evaluated COP	1.33
St. Dev.	0.025
Rel. St. Dev.	1.9%

Tab. 4.5 Comparison between the estimated COP and the effectively measured COP at steady state, cavitator NM.

The comparison between the COP obtained for the non-insulated and the insulated tests on cavitator NM shows a higher variance of the efficiencies of the insulated plant with respect to the non-insulated one (Tab 4.6). The reason of this variance could be found in the major impact on the

COP ratio of the experimental variations of the energy contributions, due to the lower absolute values of the involved energies.

Cavitator NM (1.4mm)	
Non-insulated test (250 rpm)	Direct evaluation of COP
18/01/22	1.23
Insulated tests (250 rpm)	Direct evaluation of COP
03/02/22	1.35
08/02/22	1.29
10/02/22	1.32
12/02/22	1.33
Average evaluated COP	1.33

Tab. 4.6 Comparison between the direct evaluations of COP for the non-insulated and the insulated reactor, cavitator NM.

4.2 Application of the direct method for the evaluation of COP for cavitators M5, M2 and M4

Once the possibility of the reaching of the steady-state condition had been verified by means of the calorimetric tests on the second generation of brass cavitators, a series of other three attempts was performed in order to have a more reliable evaluation of the COP also for the first generation of brass nozzles. Consequently, a test for every cavitator M5, M2, M4 on the insulated plant was accomplished, and the COP obtained according to the direct method was then compared to the previous indirect assessments.

Tab. 4.7 reports the Rayleigh and Nusselt numbers and the relative internal convection heat transfer coefficient evaluated for cavitator M5.

Cavitator M5	
Tests at the velocity of 500 rpm	
<i>Ra</i> (-)	22129.12

$Nu (-)$	1498.40
$h_i \left(\frac{W}{m^2K} \right)$	77503.47

Tab. 4.7 Rayleigh and Nusselt numbers, internal convection heat transfer coefficient, cavitator M5.

The preliminary non-insulated calorimetric test on cavitator M5 resulted in the temperature and electric power curves shown in Figs. 4.29-4.30.

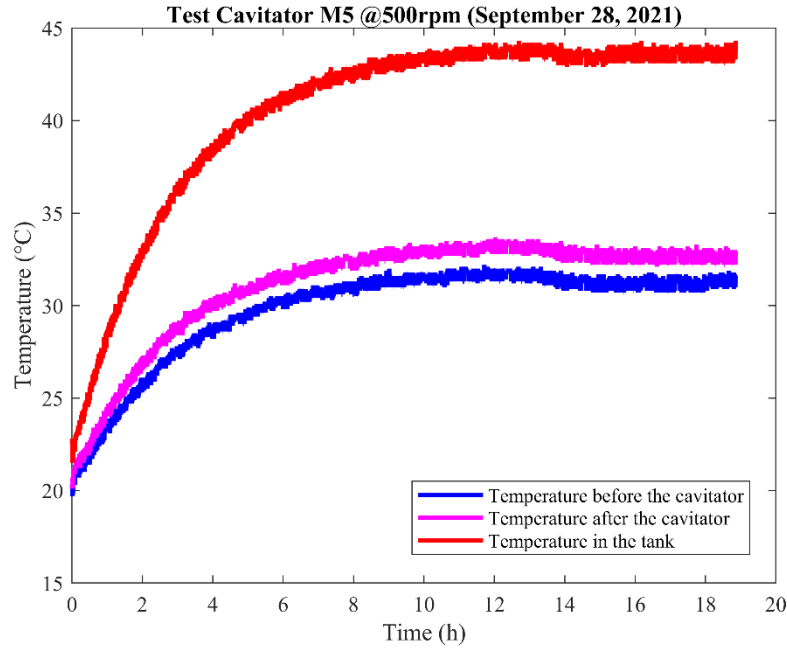


Fig. 4.29 Temperature trends from the test of the 28th of September 2021, cavitator M5, 500rpm.

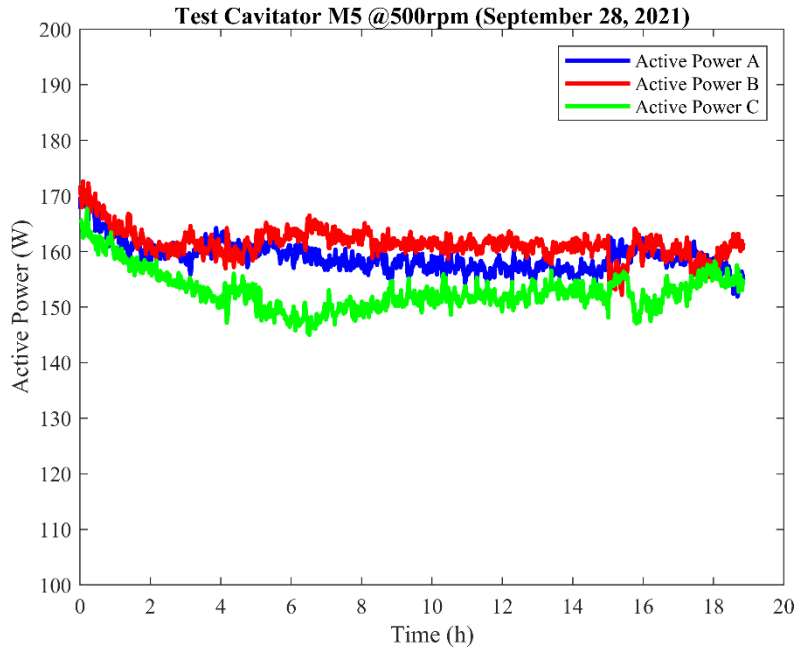


Fig. 4.30 Electric powers provided to the three-phase pump from the test of the 28th of September 2021, cavitator M5, 500rpm.

The following physical parameters of the system were taken into account:

- mass of the water solution 25 kg;
- initial (environmental) temperature 22.8°C;
- steady-state temperature before the cavitator 31.4°C;
- steady-state temperature after the cavitator 32.9°C;
- steady-state temperature in the tank 43.7°C;
- pressure drop in the cavitator 10.65 bar;
- electric power provided to the pump 473.30 W;
- pump rotation velocity 500 rpm;
- steady-state flow rate of the plant 0.0121 m³/minute;

According to the direct method, it was possible then to assess the next energy contributions:

- Input electric energy absorbed by the pump $E_{in} = 1703.9 \text{ kJ}$
- Thermal energy stored by the water $E_w = 1287.2 \text{ kJ}$
- Thermal energy dispersed in the environment $E_{disp} = 307.6 \text{ kJ}$
- Mechanical energy dissipated by the cavitator $E_{mec} = 772.6 \text{ kJ}$

Consequently, the Coefficient of Performance was evaluated as:

$$\text{COP} = \frac{E_{out}}{E_{in}} = \frac{2367.4 \text{ kJ}}{1703.9 \text{ kJ}} = 1.39 \quad (4.15)$$

The insulated test on cavitator M5 at the pump rotation velocity of 500 rpm allowed to register the temperature and electric power absorption paths portrayed in Figs. 4.31-4.32.

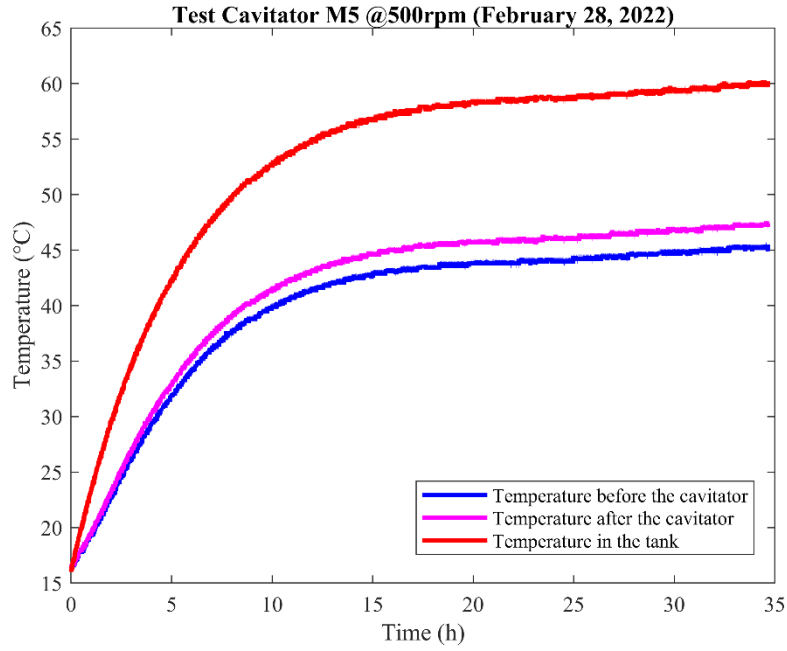


Fig. 4.31 Temperature trends from the test of the 28th of February 2022, cavitator M5, 500rpm.

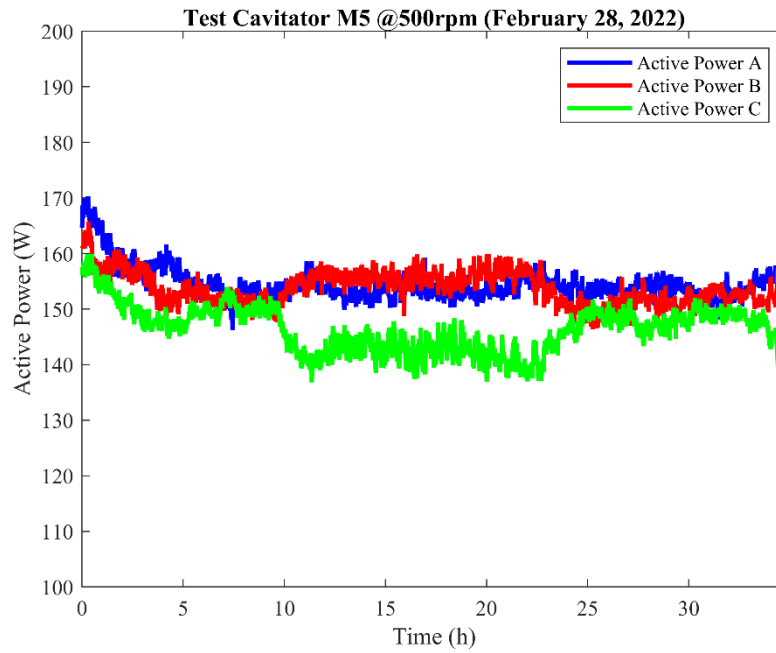


Fig. 4.32 Electric powers provided to the three-phase pump from the test of the 28th of February 2021, cavitator M5, 500rpm.

During the test, the ensuing physical data were collected:

- mass of the water solution 25 kg;
- initial (environmental) temperature 16.1°C;
- steady-state temperature before the cavitator 44.6°C;
- steady-state temperature after the cavitator 45.6°C;

- steady-state temperature in the tank 59.2°C;
- pressure drop in the cavitator 10.61 bar;
- electric power provided to the pump 454.65 W;
- pump rotation velocity 500 rpm;
- steady-state flow rate of the plant 0.0121 m³/minute;

The energy contributions were thus evaluated as follows:

- Input electric energy absorbed by the pump $E_{in} = 1636.5$ kJ
- Thermal energy stored by the water $E_w = 1527.9$ kJ
- Thermal energy dispersed in the environment $E_{disp} = 332.2$ kJ
- Mechanical energy dissipated by the cavitator $E_{mec} = 777.6$ kJ

The following Coefficient of Performance was evaluated according to the direct method:

$$COP = \frac{E_{out}}{E_{in}} = \frac{2637.7 \text{ kJ}}{1636.5 \text{ kJ}} = 1.61 \quad (4.16)$$

Tab. 4.8 shows the comparison between the COP assessed by means of the polynomial extrapolation of the indirect method and the COP directly evaluated in the steady-state condition for cavitator M5. The indirect method produced in this case a slight underestimation of the value of COP, of about the 7%.

Cavitator M5 (2.7mm)	
Indirect method (500 rpm)	Estimated COP
21/10/21	1.43
23/10/21	1.54
25/10/21	1.52
Average COP	1.50
St. Dev.	0.06
Rel. St. Dev.	4.0%
Direct method (500rpm)	Direct evaluation of COP
03/02/22	1.61

Tab. 4.8 Comparison between the estimated COP and the effectively measured COP at steady state, cavitator M5.

The test on the non-insulated plant equipped by cavitator M2 produced the temperature and electric power absorption paths depicted in Figs. 4.33-4.34. The internal convection heat transfer coefficient for cavitator M2 assumed the value reported in Tab. 4.9.

Cavitator M2	
Tests at the velocity of 500 rpm	
Ra (-)	22631.39
Nu (-)	1532.41
h_i ($\frac{W}{m^2K}$)	79262.59

Tab. 4.9 Rayleigh and Nusselt numbers, internal convection heat transfer coefficient, cavitator M2.

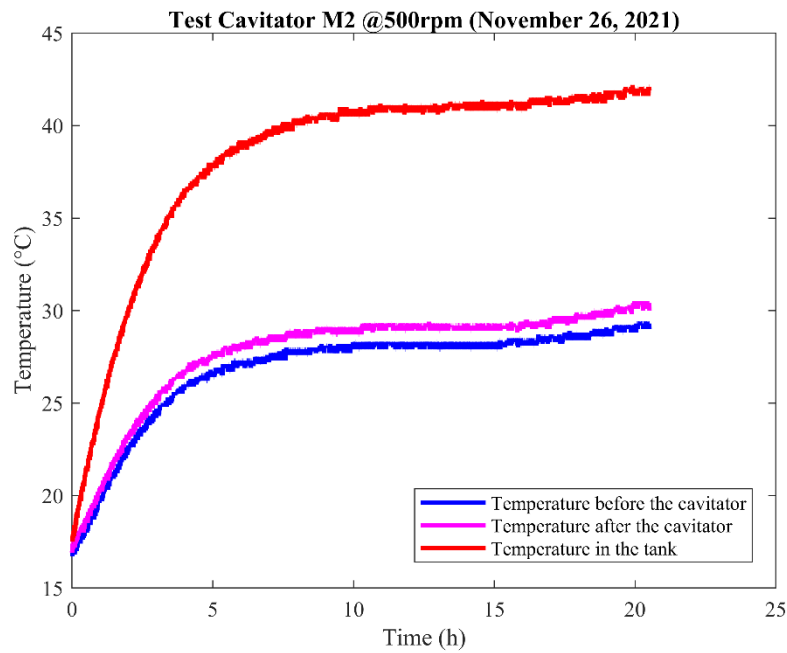


Fig. 4.33 Temperature trends from the test of the 26th of November 2021, cavitator M2, 500rpm.

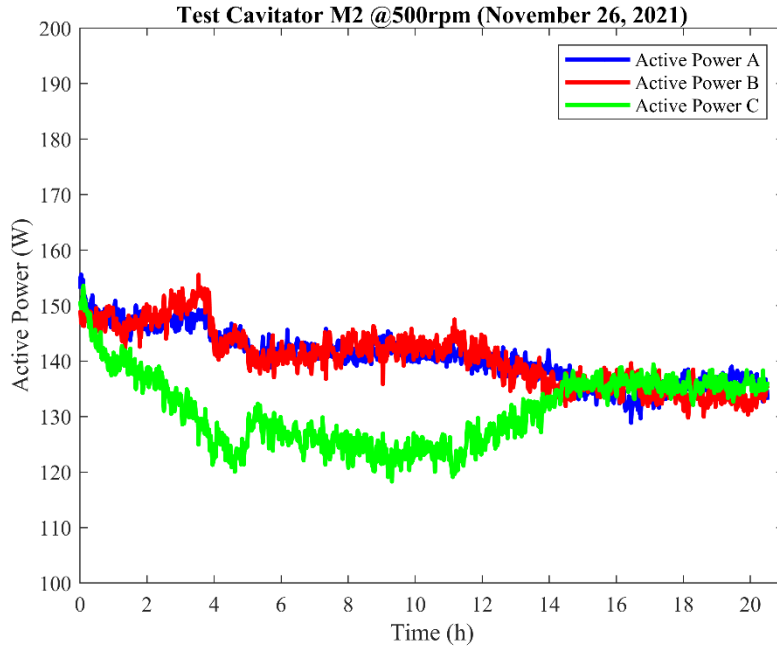


Fig. 4.34 Electric powers provided to the three-phase pump from the test of the 26th of November 2021, cavitor M2, 500rpm.

The following physical data of the system were considered in the calculations:

- mass of the water solution 25 kg;
- initial (environmental) temperature 17.5°C;
- steady-state temperature before the cavitor 28.2°C;
- steady-state temperature after the cavitor 29.2°C;
- steady-state temperature in the tank 41.0°C;
- pressure drop in the cavitor 8.75 bar;
- electric power provided to the pump 412.36 W;
- pump rotation velocity 500 rpm;
- steady-state flow rate of the plant 0.01237 m³/minute;

From the previous data it was possible then to evaluate the next energy contributions:

- Input electric energy absorbed by the pump $E_{in} = 1484.5$ kJ
- Thermal energy stored by the water $E_w = 1339.5$ kJ
- Thermal energy dispersed in the environment $E_{disp} = 338.3$ kJ
- Mechanical energy dissipated by the cavitor $E_{mec} = 649.2$ kJ

The corresponding Coefficient of Performance was calculated as follows:

$$\text{COP} = \frac{E_{out}}{E_{in}} = \frac{2327.0 \text{ kJ}}{1484.5 \text{ kJ}} = 1.57 \quad (4.17)$$

During the attempt on the insulated plant equipped by cavitator M2 the temperatures and electric power absorptions of Figs. 4.35-4.36 were registered.

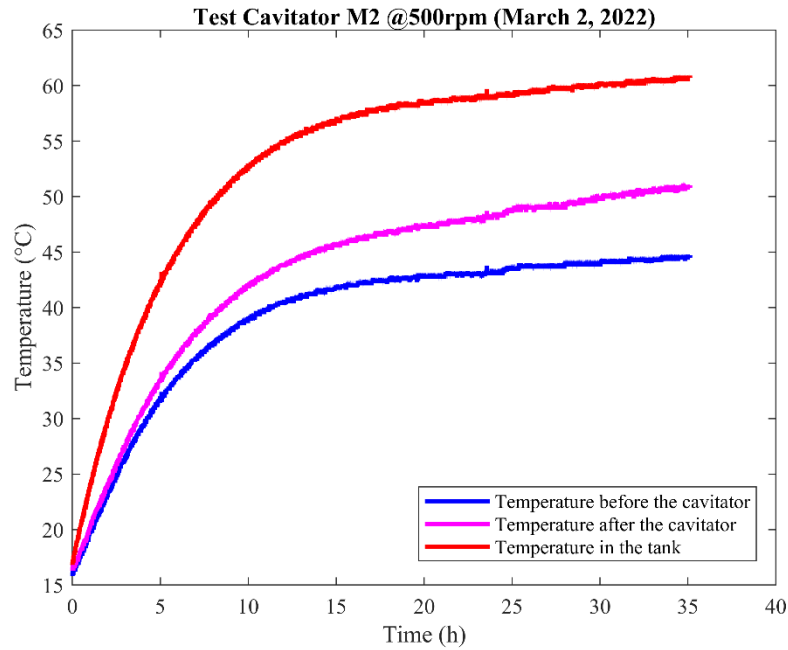


Fig. 4.35 Temperature trends from the test of the 2nd of March 2022, cavitator M2, 500rpm.

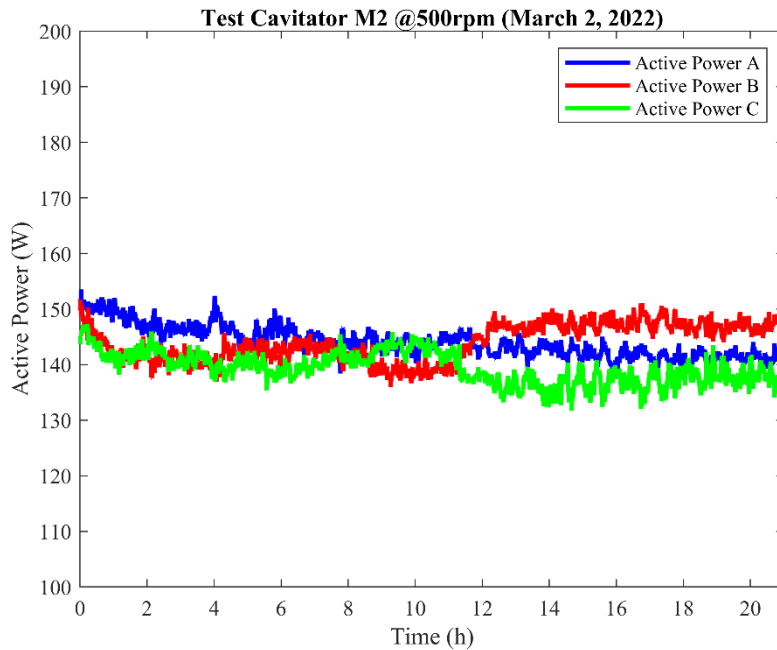


Fig. 4.36 Electric powers provided to the three-phase pump from the test of the 2nd of March 2022, cavitator M2, 500rpm.

The next physical parameters were measured:

- mass of the water solution 25 kg;
- initial (environmental) temperature 16.9°C;
- steady-state temperature before the cavitator 44.1°C;
- steady-state temperature after the cavitator 49.9°C;
- steady-state temperature in the tank 60.1°C;
- pressure drop in the cavitator 9.49 bar;
- electric power provided to the pump 427.04 W;
- pump rotation velocity 500 rpm;
- steady-state flow rate of the plant 0.01237 m³/minute;

The energy contributions according to the direct method were evaluated as follows:

- Input electric energy absorbed by the pump $E_{in} = 1537.3$ kJ
- Thermal energy stored by the water $E_w = 1674.4$ kJ
- Thermal energy dispersed in the environment $E_{disp} = 329.4$ kJ
- Mechanical energy dissipated by the cavitator $E_{mec} = 704.3$ kJ

The corresponding Coefficient of Performance was calculated as follows:

$$COP = \frac{E_{out}}{E_{in}} = \frac{2708.1 \text{ kJ}}{1537.3 \text{ kJ}} = 1.76 \quad (4.18)$$

The comparison between the indirect assessment of COP and the direct evaluation for cavitator M2 is reported in Tab. 4.10.

Cavitator M2 (2.7mm)	
Indirect method (500 rpm)	Estimated COP
27/10/21	1.40
06/11/21	1.42
16/11/21	1.41
Average COP	1.41
St. Dev.	0.01
Rel. St. Dev.	0.7%
Direct method	Direct

(500rpm)	evaluation of COP
02/03/22	1.76

Tab. 4.10 Comparison between the estimated COP and the effectively measured COP at steady state, cavitator M2.

As it is possible to notice, for cavitator M2 the indirect method of assessment for the COP led to an underestimation of about the 20% with respect to the direct evaluation. It is also relevant to underline the fact that the the COP directly evaluated for cavitator M2 resulted to be the highest between the ones obtained during the whole experimental campaign described in the present thesis.

The results in terms of calorimetric trends and electric power absorption paths for the preliminary non-insulated test on cavitator M4 are shown in Figs. 4.37-4.38. The Rayleigh and Nusselt numbers and the internal convection heat transfer coefficient adopted are reported in Tab. 4.11.

Cavitator M4	
Tests at the velocity of 500 rpm	
Ra (-)	21812.79
Nu (-)	1476.98
h_i ($\frac{W}{m^2K}$)	76395.56

Tab. 4.11 Rayleigh and Nusselt numbers, internal convection heat transfer coefficient, cavitator M4.

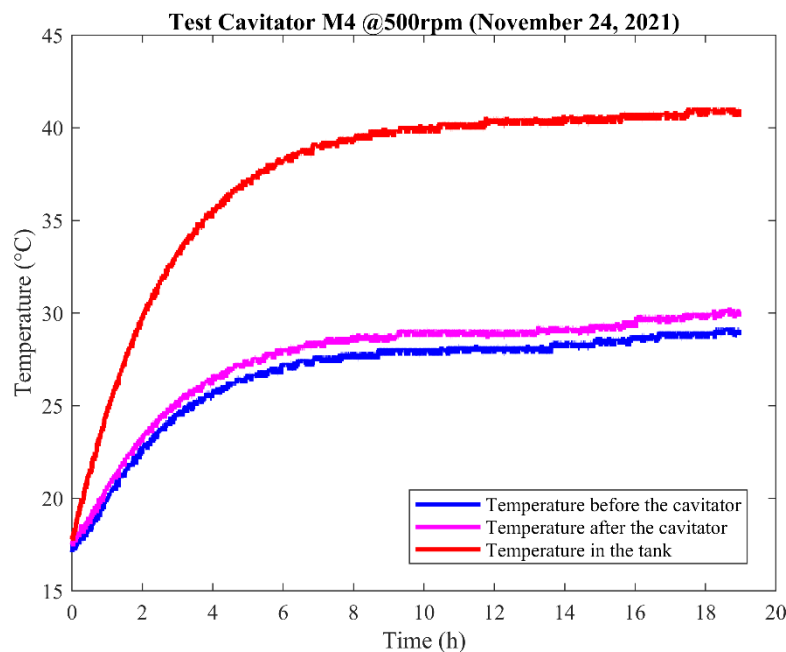


Fig. 4.37 Temperature trends from the test of the 24th of November 2021, cavitator M4, 500rpm.

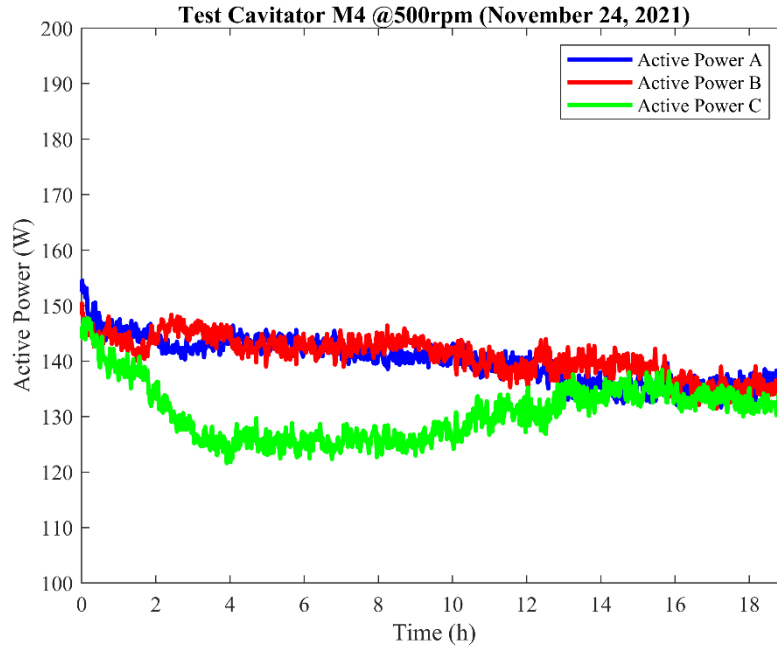


Fig. 4.38 Electric powers provided to the three-phase pump from the test of the 24th of November 2021, cavitor M4, 500rpm.

The next physical parameters were measured:

- mass of the water solution 25 kg;
- initial (environmental) temperature 17.8°C;
- steady-state temperature before the cavitor 28.4°C;
- steady-state temperature after the cavitor 29.3°C;
- steady-state temperature in the tank 40.5°C;
- pressure drop in the cavitor 8.74 bar;
- electric power provided to the pump 411.63 W;
- pump rotation velocity 500 rpm;
- steady-state flow rate of the plant 0.01192 m³/minute;

The following energy contributions were thus evaluated:

- Input electric energy absorbed by the pump $E_{in} = 1481.9$ kJ
- Thermal energy stored by the water $E_w = 1266.3$ kJ
- Thermal energy dispersed in the environment $E_{disp} = 329.0$ kJ
- Mechanical energy dissipated by the cavitor $E_{mec} = 625.6$ kJ

The previous terms allowed to calculate the Coefficient of Performance of the non-insulated test by means of the direct method:

$$\text{COP} = \frac{E_{out}}{E_{in}} = \frac{2220.9 \text{ kJ}}{1481.9 \text{ kJ}} = 1.50 \quad (4.19)$$

The insulated test on cavitator M4 at the pump velocity of 500 rpm resulted in the temperature and electric power supply curves portrayed in Figs. 4.39-4.40.

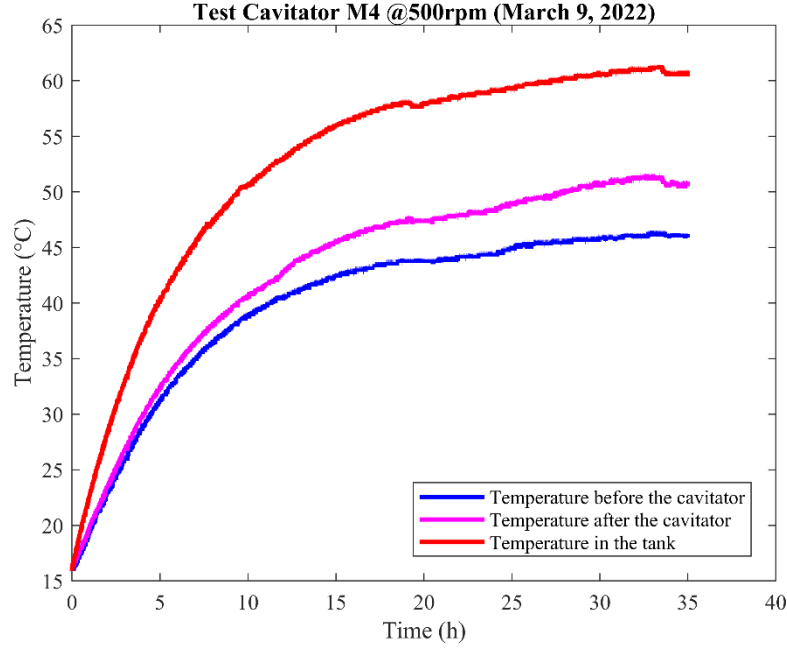


Fig. 4.39 Temperature trends from the test of the 9th of March 2022, cavitator M4, 500rpm.

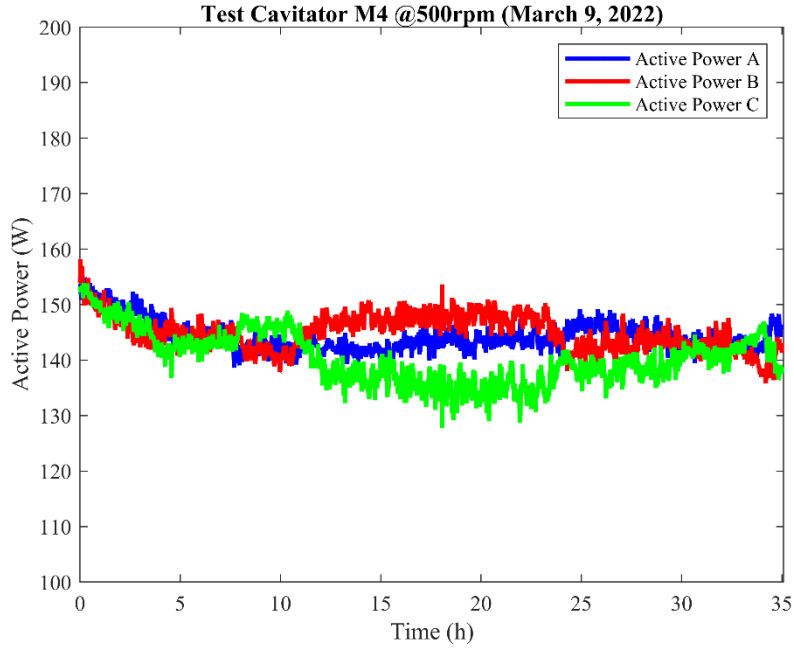


Fig. 4.40 Electric powers provided to the three-phase pump from the test of the 9th of March 2022, cavitator M4, 500rpm.

The following physical parameters were considered in the calculations:

- mass of the water solution 25 kg;
- initial (environmental) temperature 16.0°C;
- steady-state temperature before the cavitator 45.8°C;
- steady-state temperature after the cavitator 50.4°C;
- steady-state temperature in the tank 60.5°C;
- pressure drop in the cavitator 9.72 bar;
- electric power provided to the pump 429.55 W;
- pump rotation velocity 500 rpm;
- steady-state flow rate of the plant 0.01192 m³/minute;

The next energy terms were then evaluated:

- Input electric energy absorbed by the pump $E_{in} = 1546.4$ kJ
- Thermal energy stored by the water $E_w = 1538.4$ kJ
- Thermal energy dispersed in the environment $E_{disp} = 345.3$ kJ
- Mechanical energy dissipated by the cavitator $E_{mec} = 695.1$ kJ

The COP according to the direct method was finally assessed as follows:

$$\text{COP} = \frac{E_{out}}{E_{in}} = \frac{2578.8 \text{ kJ}}{1546.4 \text{ kJ}} = 1.67 \quad (4.20)$$

In Tab. 4.12 the COP assessed by means of the polynomial extrapolation of the indirect method are compared to the direct evaluation of the COP at the steady state condition.

Cavitator M4 (2.7mm)	
Indirect method (500 rpm)	Estimated COP
18/11/21	1.47
20/11/21	1.33
22/11/21	1.36
Average COP	1.39
St. Dev.	0.07
Rel. St. Dev.	5.0%
Direct method (500rpm)	Direct evaluation of

	COP
09/03/22	1.67

Tab. 4.12 Comparison between the estimated COP and the effectively measured COP at steady state, cavitator M4.

It is worth noting that also for cavitator M4 the indirect method resulted in a underestimation of the real value of the COP evaluated by means of the direct method, in this case of about the 17%.

In conclusion, the extrapolated method produced assessments of the values of the COP for the first generation of brass cavitators characterised by an underestimation between the 6% and the 20%, and it was confirmed as a conservative procedure of evaluation. On the other hand, the direct method allowed to collect values of COP for the cavitators M5, M2 and M4 in the range 1.61-1.76, which were found to be comparable to the results of the direct evaluations for cavitator NB.

Conclusions

In the last years a relevant amount of evidence has been collected about the effects of LENR in solid bodies in terms of compositional changes of the analysed specimens and neutron and alpha particle emissions. In liquid media, the experimental tests on electrolytic cells supplied by solutions of water and alkaline salts allowed to observe also noticeable extra-heat generations which were ascribed to effect of LENR, intended as fission reactions. Although the electrolytic tests needed the presence of water to promote the hydrogen embrittlement of the metal electrodes, the expected reactions happened still as a consequence of brittle fractures on the solid surfaces of the anode and the cathode

In this thesis for the first time a whole experimental campaign has been accomplished with the aim of exploring the calorimetric aspects related to piezonuclear reactions produced directly by a mechanical instability in the liquid medium, the implosion of bubbles of nanometric dimensions that formed as consequence of the cavitation phenomenon. Indeed, as theoretically suggested by the relation between wavelengths and frequencies, by Planck's law and by the scaling law between the cause of the mechanical instability and the frequency of the released phonon, it was expected that the implosion of nano-bubbles in a water solution enriched by iron salts would have elicited TeraHertz pressure waves that would have been able to establish resonance with the Debye frequency of a medium-weight metal as iron, causing in this way the fission of its dispersed atoms in solution in lighter elements.

The nuclear nature of the phenomenon produced as a consequence of cavitation was confirmed by the relevant neutron emissions observed during the tests, which allowed to reveal peaks also 100% higher than the natural neutron background, and by the compositional changes of the metal ions in water solution, which reflected a sensible percentage decrease of iron and a contemporary increase of aluminium, intended as a product of the fission reaction.

In order to assess in a proper way the heat generations caused by the cavitation process in the water solution, two different methods were proposed, the indirect assessment and the direct evaluation solutions, which allowed to determine of the COP of the reactor in steady-state conditions. According to both methods, three terms of output energy were considered as products of the cavitation process, being the thermal energy stored by the water in a full cycle, the mechanical energy dissipated by the passage through the cavitator section in the reference time and the thermal energy dispersion in the environment, given by the conduction, convection and irradiation effects. The input energy contribution was considered as the electrical energy supplied to the three-phase pump in the reference period considered for the COP evaluation (one hour). The main difference

between the indirect and the direct method of estimate was constituted by the fact that the first one referred to calorimetric tests interrupted still in transient phase, and then the steady-state condition temperatures were assessed by means of a numerical extrapolation according to the least square procedure; instead, the direct method allowed to measure the final temperatures once the thermal equilibrium condition had been reached. The comparison in terms of COP evaluated according to the two methods allowed to observe in general an underestimation of the value of efficiency obtained by the polynomial extrapolation, and on these bases the indirect method was considered as a conservative estimate which allowed to reduce the test durations from about 30-35 hours to 8-10 hours, despite some revealed numerical instabilities. On the other hand, the progressive development of the knowledge of the plant limitations which led to the capability of execution of direct COP evaluations also for the plant in insulated conditions was considered as one of the main procedural results obtained during the experimental activity.

The COP evaluated in the two ways for the seven different typologies of brass cavitators tested from the calorimetric perspective had the paramount importance effect of giving a first numerical quantification of the energy produced by LENR caused by the cavitation phenomenon. Indeed, by testing the cavitators at the believed optimal pump turning velocity, exceedances between the 30% and the 76% of the output energies were revealed with respect to the input electrical supply, which highlighted the relevant extra-heat generations expected. It is worth noting that these noticeable values were obtained by the employment of a reduced quantity of iron salts, equal to just 5 ppm in the water solution, and this constituted a sign of the potentialities of the studied reactions.

Furthermore, the large amount of accomplished tests allowed to assess the optimal turning velocity of the pump for the geometry of the adopted brass cavitator at about 500 rpm, to verify the importance of the transitions of the internal diameters with sharp edges in the promotion of the cavitation phenomenon and to evaluate the increase of the steady-state temperature in the tank by effect of the thermal insulation, aimed to the achievement of temperature values nearer to the ones required by industrial applications. The tests on the cavitators characterised by reduced final diameters provided the first signs of the possible favourable effect of the reducing throat section on the efficiencies, and they led to the proposal, as a future improvement, of a new generation of cavitators with several holes of small dimensions, that would be able to grant higher flow rates avoiding excessive exercise pressures.

Therefore, another result of primary importance was obtained from the theoretical point of view by the optic experimental survey for the measurement of the dimensions of the produced bubbles. The comparison between the calorimetric outcomes and the assessed nano-bubble populations resulted in the evaluation of the thermal energy per imploded nano-bubble, which was found to

assume an almost constant value for three cavitators analysed. Since the variation of several physical parameters of the test seemed to have negligible effects on the energy per imploded nano-bubble, it was considered as a confirmation of the importance of the nano-bubble implosions and the TeraHertz frequency phonons in the promotion of LENR in the iron salts dispersed in the water solution.

In conclusion, the energy evaluations related to the cavitation phenomenon resulted in an important demonstration of the extra-heat generation from LENR in liquid media, and the obtained outcomes encourage to a further development of the cavitator geometries and cavitation reactor setups, with a view to future possible industrial applications. The neutron emission and compositional change surveys, thus, together with the discovery of the consistency of the energy per imploded nano-bubble, constituted a series of additional proofs about the role of the piezonuclear reactions caused by the nano-bubble implosions on the energy release that clear the way for other experimental in-depth analyses.

Acknowledgments

The MS candidate wishes to thank the European Research Project “Clean Energy from Hydrogen-Metal Systems” (CleanHME, ID 951974) for the economic support and the interest in the experimental results, as well as the company MetalWork S.p.A. for the economic and technical support and for the realisation of the cavitation plant. A grateful mention is then bestowed to Professor Alberto Carpinteri and to Doctor Francesco Montagnoli for their active involvement in the experimental activities of the present MS thesis, and to Doctor Oscar Borla for the earlier calorimetric and neutron emission measurements and for the optical monitoring.

Warm thanks are finally addressed to the candidate’s Family for the moral and material support provided during the last demanding years of study.

References

1. C. E. Brennen: "Cavitation and bubble dynamics", Oxford University Press (1995).
2. O. Borla, G. Lacidogna, A. Zanini, A. Carpinteri: "The phenomenon of neutron emission from earthquakes", in *Fracture Mechanics for Durability, Reliability and Safety* (Proceedings of the 19th European Conference on Fracture), Kazan, Russia (2012), Paper N. 620.
3. F. Cardone, G. Lacidogna, A. Carpinteri: "Piezonuclear neutrons emission from brittle compression failure", *Conference & Exposition on Experimental and Applied Mechanics (SEM)*, Albuquerque, New Mexico (2009), Paper N. 541.
4. F. Cardone, A. Manuello, R. Mignani, A. Petrucci, E. Santoro, M. Sepielli, A. Carpinteri: "Ultrasonic piezonuclear reactions in steel and sintered ferrite bars", *Journal of Advanced Physics*, Vol. 5 (2016), 69-75.
5. F. Cardone, A. Carpinteri, G. Lacidogna: "Piezonuclear neutrons from fracturing of inert solids", *Physics Letters A*, Vol. 373 (2009), 4158-4163.
6. A. Carpinteri, F. Cardone, G. Lacidogna: "Energy emissions from failure phenomena: Mechanical, electromagnetic, nuclear", *Experimental Mechanics*, Vol. 50 (2010), 1235-1243; *Conference & Exposition on Experimental and Applied Mechanics (SEM)*, Albuquerque, New Mexico (2009), Paper N. 538.
7. A. Carpinteri, F. Cardone, G. Lacidogna: "Piezonuclear neutrons from brittle fracture: Early results of mechanical compression tests", *Strain*, Vol. 45 (2009), 332-339; *Atti dell'Accademia delle Scienze di Torino*, Torino, Italy, Vol. 33 (2009), 27-42.
8. A. Carpinteri, G. Lacidogna: "Energy emissions from fracture of concrete: Acoustic, electromagnetic, piezonuclear", in *Fracture Mechanics of Concrete Structures* (Proceedings of the 7th International FraMCoS Conference), Jeju, Korea, Vol. 1 (2010), 21-28.
9. A. Carpinteri, G. Lacidogna, A. Manuello, O. Borla: "Evidence of piezonuclear reactions: From geological and tectonic transformations to neutron detection and measurements",

Conference & Exposition on Experimental and Applied Mechanics (SEM), Indianapolis, USA (2010), Paper N. 458.

10. A. Carpinteri, G. Lacidogna, A. Manuello, O. Borla: "Piezonuclear transmutations in brittle rocks under mechanical loading: Microchemical analysis and geological confirmations", in *Recent Advances in Mechanics - Dedicated to the Late Professor P.S. Theocaris*, Springer, Chennai (2010), 361-382.
11. A. Carpinteri, A. Chiodoni, A. Manuello, R. Sandrone: "Compositional and microchemical evidence of piezonuclear fission reactions in rock specimens subjected to compression tests", *Strain*, Vol. 47, Suppl. 2 (2011), 282-292.
12. A. Carpinteri, G. Lacidogna, A. Manuello, O. Borla: "Energy emissions from brittle fracture: Neutron measurements and geological evidences of piezonuclear reactions", *Strength, Fracture and Complexity*, Vol. 7 (2011), 13-31.
13. A. Carpinteri, A. Manuello: "Geomechanical and geochemical evidence of piezonuclear fission reactions in the Earth's Crust", *Strain*, Vol. 47, Suppl. 2 (2011), 267-281.
14. A. Carpinteri, G. Lacidogna, A. Manuello, O. Borla: "Piezonuclear fission reactions in rocks: Evidences from microchemical analysis, neutron emission, and geological transformation", *Rock Mechanics and Rock Engineering*, Vol. 45 (2012), 445-459.
15. A. Carpinteri, G. Lacidogna, A. Manuello, O. Borla: "Piezonuclear neutrons from earthquakes as a hypothesis for the image formation and the radiocarbon dating of the Turin Shroud", *Scientific Research and Essays*, Vol. 7 (2012), 2603-2612.
16. A. Carpinteri, G. Lacidogna, A. Manuello, G. Niccolini, O. Borla: "Time correlation between acoustic, electromagnetic and neutron emissions in rocks under compression", *Conference & Exposition on Experimental and Applied Mechanics (SEM)*, Costa Mesa, California, USA, Chapter N. 50 (2012), 387-393.

17. A. Carpinteri, O. Borla, A. Goi, A. Manuello, D. Veneziano: "Mechanical conjectures explaining cold nuclear fusion", *Conference & Exposition on Experimental and Applied Mechanics (SEM)*, Lombard, Illinois, USA, Vol. 3 (2013), 353-367.
18. A. Carpinteri, G. Lacidogna, A. Manuello, O. Borla: "Piezonuclear fission reactions from earthquakes and brittle rocks failure: Evidence of neutron emission and nonradioactive product elements", *Experimental Mechanics*, Vol. 53 (2013), 345-365.
19. A. Carpinteri O. Borla, A. Goi, S. Guastella, A. Manuello, D. Veneziano: "Hydrogen embrittlement and cold fusion effects in palladium during electrolysis experiments", *Conference & Exposition on Experimental and Applied Mechanics (SEM)*, Greenville, South Carolina, USA, Vol. 6 (2014), 37-47.
20. A. Carpinteri, G. Lacidogna, A. Manuello: "Acoustic, Electromagnetic, Neutron Emissions from Fracture and Earthquakes", Springer International Publishing Switzerland (2015).
21. A. Carpinteri, G. Lacidogna, O. Borla, M. Costantino: "Acoustic, Electromagnetic, Neutron Emissions as Seismic Precursors", *Second Greek-Russian Symposium on Mechanics Xanthi*, Greece (2015).
22. A. Carpinteri, O. Borla, A. Manuello, D. Veneziano, A. Goi, "Hydrogen embrittlement and piezonuclear reactions in electrolysis experiments", *Journal of Condensed Matter Nuclear Science*, Vol. 15 (2015), 162-182.
23. A. Carpinteri, A. Manuello, D. Veneziano, N.D. Cook: "Piezonuclear fission reactions simulated by the lattice model", *Journal of Condensed Matter Nuclear Science*, Vol. 15 (2015), 149-161.
24. A. Carpinteri: "Opto-acoustic and neutron emissions from fracture and earthquakes", *Conference & Exposition on Experimental and Applied Mechanics (SEM)*, Costa Mesa, California, USA, Vol. 8 (2015), 135-140.
25. A. Carpinteri, O. Borla: "Fracto-emissions as seismic precursors", *Engineering Fracture Mechanics*, Vol. 177 (2017), 239-250.

26. A. Carpinteri, O. Borla: "Nanomechanics instabilities and TeraHertz vibrations: From geochemical evolution to fracto-emission seismic precursors", *Conference & Exposition on Experimental and Applied Mechanics (SEM)*, Indianapolis, Indiana, USA, Vol. 5 (2017), 1-5.
27. A. Carpinteri, O. Borla, A. Manuello, G. Niccolini: "Energy Balance During Elettrolisis and Cavitation Experiments", *The Society for Experimental Mechanics, Micro and Nanomechanics*, Vol. 5 (2018), 37-40.
28. A. Carpinteri, O. Borla: "Nano-scale fracture phenomena and TeraHertz pressure waves as the fundamental reasons for geochemical evolution", *Strength, Fracture and Complexity*, Vol. 11 (2018), 149-168.
29. A. Carpinteri, O. Borla: "Acoustic, electromagnetic, and neutron emissions as seismic precursors: The lunar periodicity of low-magnitude seismic swarms", *Engineering Fracture Mechanics*, Vol. 210 (2019), 29-41.
30. A. Carpinteri, G. Niccolini: "Correlation between the Fluctuations in Worldwide Seismicity and Atmospheric Carbon Pollution", *Sci*, Vol. 1 (2019), 1-12.
31. A. Carpinteri, O. Borla: "Strong Correlation Between LENR and Nano-Mechanics Instabilities/THz Phonons in Condensed Matter: Application in Geophysics, Geochemistry, Energetics, Biology", *Infinite Energy*, Issue 153 (2020), 32-37.
32. R. Hickling, M. S. Plesset: "The collapse of a spherical cavity in a compressible liquid", *Report No. 85-24*, Office of Naval Research, Department of the Navy (1963).
33. S. Invernizzi, O. Borla, G. Lacidogna, A. Manuello, A. Carpinteri: "Piezonuclear evidences from laboratory tests on steel", in *Fracture Mechanics for Durability, Reliability and Safety* (Proceedings of the 19th European Conference on Fracture), Kazan, Russia (2012), Paper N. 383.

34. G. Lacidogna, G. Piana, A. Carpinteri: "Damage monitoring of three-point bending concrete specimens by acoustic emission and resonant frequency analysis", *Engineering Fracture Mechanics*, Vol. 210 (2019), 203-211.
35. U. Lucia, A. Carpinteri: "GeV plasmons and spalling neutrons from crushing of iron-rich natural rocks", *Chemical Physics Letters*, Vol. 640 (2015), 112-114.
36. A. Manuello, R. Malvano, O. Borla, A. Palumbo, A. Carpinteri: "Neutron Emission from Hydrodynamic Cavitation", *Fracture, Fatigue, Failure and Damage Evolution, Conference Proceedings of the Society for Experimental Mechanics Series*, The Society for Experimental Mechanics, Volume 8 (2016), 175-182.
37. M. Postema, N. De Jong, G. Schmitz: "Shell rupture threshold, fragmentation threshold, Blake threshold", *IEEE International Ultrasonics Symposium*, Rotterdam, Netherlands (2005), 1708-1711.
38. J. Willard Gibbs: "Graphical methods in the Thermodynamics of fluids", *Scientific Papers of Josiah Willard Gibbs, Transaction of the Connecticut Academy*, Vol. 2. (1873), 309-342.
39. K. Yasui, T. Tuziuti, M. Sivakumar, Y. Iida: "Theoretical study of single-bubble sonochemistry", *Journal of Chemical Physics* (2005).